Alpha backgrounds in the DEAP Dark Matter search experiment

by

Tina Pollmann

A thesis submitted to the
Department of Physics, Engineering Physics and Astronomy
in conformity with the requirements for
the degree of Doctor of Philosophy

Queen's University
Kingston, Ontario, Canada
August 2012

Abstract

One of the pressing concerns in Dark Matter detection experiments is ensuring that the potential signal from exceedingly rare Dark Matter interactions is not obscured by background from interactions with more common particles. This work focuses on the ways in which alpha particles from primordial isotopes in the DEAP detector components can cause background events in the region of interest for Dark Matter search, based on both Monte Carlo simulations and data from the DEAP-1 prototype detector.

The DEAP experiment uses liquid argon as a target for Dark Matter interactions and relies on the organic electroluminescent dye tetraphenyl butadiene (TPB) to shift the UV argon scintillation light to the visible range. The light yield and pulse shape of alpha particle induced scintillation of TPB, which is an essential input parameter for the simulations, was experimentally determined.

An initial mismatch between simulated and measured background spectra could be explained by a model of geometric background events, which was experimentally confirmed and informed the design of certain parts of the DEAP-3600 detector that is under construction at the moment. Modification of the DEAP-1 detector geometry based on this model led to improved background rates. The remaining background

was well described by the simulated spectra, and competitive limits on the contamination of acrylic with primordial isotopes were obtained. Purity requirements for the DEAP-3600 detector components were based on this work.

The design and testing of a novel large area TPB deposition source, which will be used to make TPB coatings for the DEAP-3600 detector, is described.

Statement of originality

The work in this thesis is my own unless where stated otherwise.

The DEAP-1 detector was operated and maintained by Chris Jillings and his team at SNOLAB. The automated pulse analysis calculating values like total charge and Fprompt parameters for each event was already in place when I joined the group. All other analysis code, producing results regarding data selection, timing analysis, and energy calibration, was written by me. The initial alpha timing and spectrum analysis for the V2 detector was worked on by Hugh Lippincott, Eoin O'Dwyer, Kevin Olsen and me and we shared and double checked each others results, but all results presented here come from my own analysis done with my own code and calculations, and represent a significant extension to the original work done in the team.

The alpha scintillation measurement, including the production of the TPB films, the setup of the dark box and scintillation chamber, and scintillation data analysis was done by myself. Marcin Kuźniak played a significant part in operating the stylus profile meter to characterize the coatings, and in interpreting those measurements.

The original concept for the large area TPB evaporation source came from M. Boulay and C. Gilmour. The concept was substantially extended by myself with the quantitative calculations determining hole size and layout, and the heat up mechanism. The source was constructed by myself with R. Gagnon's help in drilling the

holes. The source test stand was built following the drawing of M. Boulay, with help from M. Kuźniak and R. Gagnon, and the slow control system was programmed by M. Ward. All electrical connections for heating and sensor operation were done by myself. The coatings were again characterized with M. Kuźniak's help using the stylus profile meter, but the results of these and the deposition monitor measurements were analyzed and synthesized by me.

Acknowledgments

I would like to thank my advisor Mark Boulay for taking me on a as a PhD student and for sharing many excellent ideas. I owe thanks to the DEAP collaboration, in particular: Chris Jillings for being there week after week on the analysis call, discussing the latest weirdness in the data; Marcin Kuźniak for all his help building things in the lab, getting the DEAP software up and running and always being ready to toss around hypotheses with me, trying to explain the latest weirdness in the data; Hugh Lippincott for many great exchanges on the alpha analysis; Bei Cai for always making sure the lab is in workable conditions; Paradorn Pasuthip for making the office a fun place to be. Many thanks go to the SNO group at Queen's, particularly Art McDonald for making me feel so welcome in the group; Wolfgang Rau for his astonishing willingness to explain and to help out; Robert Gagnon and Chuck Hearns for bringing my hand drawn sketches to life in the machine shop; Peter Skensved for sharing his expertise with PMTs; Steve Gillen for his advice on building anything electronic; and my fellow grad students for making my time here enjoyable.

I would like to thank my family and my boyfriend for all their support.

Table of Contents

List of Tables

List of Figures

Chapter 1

Introduction

1.1 Evidence for and nature of Dark Matter

In its original meaning and as the name implies, Dark Matter is matter that does not emit electromagnetic radiation and thus cannot be directly observed in an astronomical context. This is in contrast to luminous matter, i.e. stars or hydrogen gas. Astronomers expect most of the normal matter in astronomical entities such as galaxies to be made up of luminous matter. Dark Matter in that context could be brown dwarfs, planets, neutron stars or black holes, which can collectively be classified as Massive Compact Halo Objects (MACHOs).

More recently, Dark Matter has come to mean specifically a non-baryonic type of matter that is "dark" because it does not interact with electromagnetic radiation. Numerous astronomical and cosmological observations today can best be explained by the existence of such Dark Matter. The following discussion follows the work of Bertone et al.[8] except where otherwise cited.

The rotation curves of galaxies, that is the velocity of stars in a galaxy versus their

distance from the galaxy center, provide evidence for large amounts of non-luminous matter within galaxies. There is a well-known relation between luminosity and mass of stars, allowing astronomers to map the amount and location of luminous mass in a galaxy.

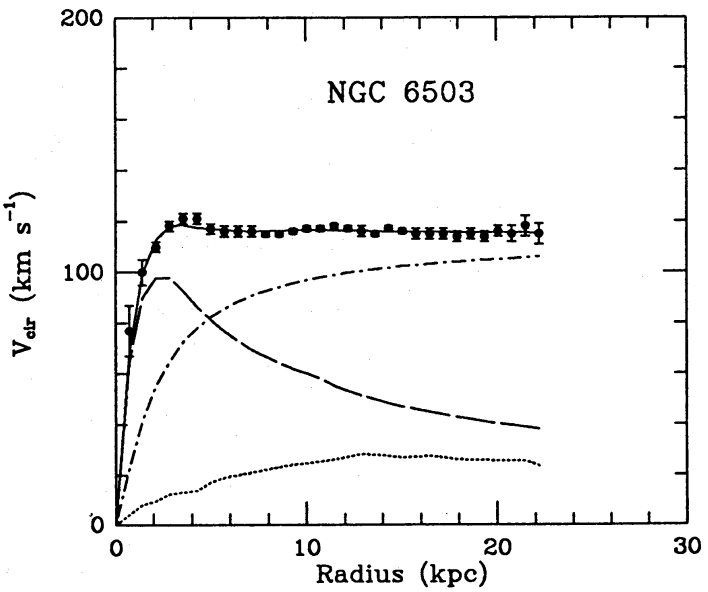

Figure 1.1: Rotation curve of galaxy NGC 6503 with three parameter fit from Ref. [5]. Dashed, dotted and dash-dot curves are the visible, gas and dark matter halo mass contributions.

Outside of the radius containing the bulk of the galaxy's mass, the rotation curve should fall as $\frac{1}{\sqrt{r}}$ according to the accepted law of gravity. However for many galaxies whose rotation curves have been measured, such as NGC 6503 shown in Fig. 1.1, the behaviour is flat, indicating that the luminous mass in the galaxy is surrounded by a halo of non-luminous mass.

The rotation curves indicate a spherical or near-spherical galactic halo of Dark Matter, though if this was the only evidence, it could as well be explained by postulating changes to the law of gravity at large radii.

Figure 1.2: False colour image of the bullet cluster. The locations from where x-ray emissions were detected are shown in red. The x-rays come from hot gas, which provides most of the baryonic matter in the cluster. The location of strongest gravitational pull, attributed to the Dark Matter component of the cluster, was determined through micro-lensing and is shown blue. Both are drawn on top of an optical image of the cluster. The hot gas was slowed down when the two galaxy clusters that now form the bullet cluster collided, so that it now lags behind the dark matter, which dominates in terms of mass. Image Credit: X-ray: NASA/CXC/M.Markevitch et al. Optical: NASA/STScI; Magellan/U.Arizona/D.Clowe et al. Lensing Map: NASA/STScI; ESO WFI; Magellan/U.Arizona/D.Clowe et al.

The first hint for the existence of Dark Matter was found on the next larger scale by F. Zwicky in 1933. He found that the velocity dispersion of galaxies in galaxy clusters is inconsistent with the amount of luminous mass in the clusters. The virial theorem can be used to find the gravitational mass of a cluster based on the observed distribution of radial velocities of its components. Comparing this mass to the mass calculated based on the light emitted from the stars in the cluster, one finds that only about 0.05% to 0.1% of the cluster's mass is luminous.

Weak gravitational lensing studies of the mass distribution in galaxy clusters[17] also indicate that a large fraction of the mass in those clusters is dark. In particular the now famous bullet cluster (Fig. 1.2), has shown that the gravitational centre of mass sometimes does not coincide with the baryonic centre of mass. This finding rules out many attempts at explaining the missing mass by postulating modifications to the theory of gravity.

Some of the most convincing evidence for the existence of non-baryonic Dark Matter can be found on a cosmological scale by studying anisotropies in the cosmic microwave background (CMB)[37]. The CMB is relic radiation from the time shortly after the Big Bang when matter decoupled from radiation. Fluctuations in the CMB temperature follow fluctuations in the matter density during that time. From studying these fluctuations and under the assumption of the standard cosmological model, the total matter and the cold dark matter density in the universe can be inferred. The latest results from WMAP, the experiment with the most precise measurement of the CMB, combined with the results from large scale structure observations, indicate that of the energy density in the universe, 4.5% is in the form of baryonic matter, 22.6% is in the form of dark matter and 72.9% is dark energy[42].

These observations require a particle that interacts gravitationally and is stable or long-lived enough to have survived since the Big Bang. It must be non-relativistic, or cold, at the time of structure formation and thus rather massive, to explain structure formation, and non-baryonic, as indicated by WMAP, and electrically neutral. This particle, called a weakly interacting massive particle (WIMP), cannot be found in the current Standard Model of particle physics.

Various extensions to the Standard Model of particle physics predict the existence of as yet unobserved new particles. The most favoured one of those with respect to a dark matter candidate is the neutralino, which is the lightest stable particle in the minimal super symmetric extensions to the standard model of particle physics.

Another viable Dark Matter candidate is the lightest Kaluza Klein particles, which arise in theories that involve extra dimensions.

1.2 Dark Matter detection

1.2.1 Experimental overview

The existence of Dark Matter has so far only been inferred from the effect it has on luminous matter and light in the universe. Detecting Dark Matter directly can give valuable information regarding the particle's mass, spin, and interaction strength.

Two basic approaches to Dark Matter detection exist: direct and indirect measurements. Direct detection experiments attempt to detect the scattering of particles from the Dark Matter halo of our galaxy off of a target nucleus in an earth-bound experiment. Indirect detection experiments try to detect the products (e.g. neutrinos or photons) of annihilation of Dark Matter particles with each other from areas such

as the sun or the galactic centre, where they can become gravitationally trapped. In addition, the possibility of the creation of Dark Matter particles at accelerator experiments exists, where missing energy or momentum can give hints as to an unobserved particle.

Indirect Dark Matter searches are often a secondary goal for experiments mainly designed to detect neutrinos (e.g. AMANDA, IceCube[68] and ANTARES[56]), cosmic gamma rays (e.g. EGRET and the Fermi Gamma-ray Space Telescope), or cosmic radiation[7] (e.g. PAMELA and ATIC)[23].

Direct detection experiments have been built or planned that rely on a variety of signals, such as light (scintillation), charge and/or sound (phonons) to detect a nuclear recoil event caused by scattering WIMPs. Some of the most sensitive experiments are listed in table 1.1.

Experiment	Medium	Signal	Status
CDMS[67]	germanium	phonon, ionization	results/running
EDELWEISS[50]	germanium	phonon, ionization	results
DAMA[6]	NaI(Tl)	scintillation	results/running
CRESST[40]	$CaWO_4$	phonon, scintillation	results/running
CoGeNT[1]	germanium	ionization	results/running
XENON[3]	xenon	scintillation, ionization	results/running
WARP[13]	argon	scintillation, ionization	results
LZS[53](LUX and ZEPLIN)	xenon	scintillation, ionization	planned
DEAP	argon	scintillation	under construction
MiniCLEAN[33]	argon or neon	scintillation	under construction
PICASSO[61]	C_4F_{10}	ionization	running
COUPP[9]	CF_3I	ionization	results/running

Table 1.1: List of some of the larger Dark Matter direct detection experiments.

The current best limits on the spin-independent WIMP-nucleon cross section come from the XENON and CDMS experiments. A controversial detection claim

has been made by the DAMA collaboration[6], but several other experiments exclude the WIMP mass and scattering cross section they claim to observe. The CoGeNT and CRESST experiments also find an excess over the expected number of low energy events and cautiously state that this may be compatible with a WIMP interpretation[4], but their excess can be explained by a more careful simulation of surface backgrounds[46].

The upcoming class of ton-scale target mass experiments, such as DEAP-3600, will be able to extend the sensitivity and provide a further test of some of these claims.

1.2.2 Analysis of recoil spectra

Direct detection experiments measure dark matter recoil spectra which can be analyzed to find the scattering cross section and mass of dark matter particle, given certain assumptions as to our galaxy's Dark Matter halo properties. The expected recoil spectra and standard halo properties are well-described in Ref. [64] and [47], and will be summarized here.

Using Fermi's Golden Rule, the WIMP-nucleon scattering cross section can be divided into a term σ_0 that is independent of the momentum transfer and a term F^2, called the form factor, that contains the dependence on the momentum transfer q[64]:

$$\frac{d\sigma(q)}{dq^2} = \frac{\sigma_0 F^2(q)}{4\mu_A^2 v^2} \tag{1.1}$$

where v is the velocity of the WIMP in the lab frame, and $\mu_A = M_\chi M_A/(M\chi + M_A)$ with the mass of the target nucleus M_A and the mass of the WIMP M_χ. The momentum independent cross section σ_0 can be further divided into a spin-dependent and spin-independent component. The spin independent part, under the assumption

that the coupling of WIMPs to protons and neutrons is of similar strength, can be written as[64]

$$\sigma_{0,SI} = \sigma_{SI}\frac{\mu_A^2}{\mu_n^2}A^2 \tag{1.2}$$

where A is the atomic mass of the target nucleus and μ_n the reduced mass of the WIMP nucleon system. σ_{SI} is then a target-independent spin-independent cross section that can be used to compare experimental results to each other or to theory.

Spin-dependent interactions are possible only in nuclei that have a net spin. Argon has even numbers of protons and neutrons, and thus is not sensitive to spin-dependent interactions[64].

The standard assumptions used with respect to the kinematics are a local WIMP density of 0.3 GeVc^{-2}cm^{-3}, a mean WIMP velocity of 230km s^{-1}, and a galactic escape velocity of 600 km s^{-1}. In the simplest case of zero momentum transfer, the WIMP spectrum follows from simple elastic scattering calculations, assuming a Maxwellian velocity distribution of the WIMPs. The rate R over the observed recoil energy E_R is:

$$\frac{dR}{dE_R} = c_1\frac{R_0}{E_0 r}e^{-c_2 E_R/E_0 r} \tag{1.3}$$

where, E_0 is the most probable energy of the incident WIMP, $r = 4M_\chi M_A/(M_\chi + M_A)^2$, and R_0 is the total event rate. The differential rate is usually given in units of kg^{-1}keV^{-1}d^{-1}. The parameters c_1 and c_2 are constants with average values of 0.751 and 0.56 for the above quoted values for the WIMP density, mean velocity and escape velocity.

There is a modulation of c_1 and c_2 with the time of year, as the apparent velocity of WIMPs changes with the earth's rotation around the sun. This modulation is considered "smoking gun" evidence for Dark Matter interactions and could be used

to separate the WIMP signal from a constant background event rate in experiments that are not background-free, but demonstrate a significant rate of Dark Matter interactions.

The experimentally expected shape of the spectrum is given by equation 1.3 multiplied by the scattering cross section and a term accounting for detector effects such as energy threshold and energy resolution. Sample spectra are shown in figure 1.3 for argon, xenon and germanium targets, including nuclear form factors, for a 100 GeV WIMP with an interaction cross section of 10^{-43} cm^2 and an exposure of 365 ton·days[27].

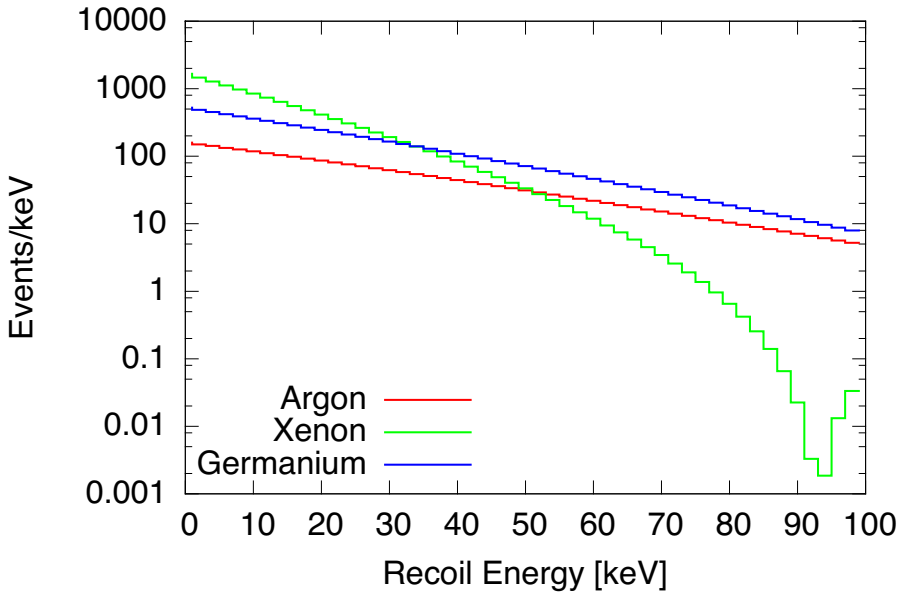

Figure 1.3: WIMP recoil spectra in argon, xenon and germanium targets, including nuclear form factors, for a 100 GeV WIMP with an interaction cross section of 10^{-7} pb and an exposure of 365 ton·days[27].

The energy spectrum described here is featureless and exponentially falling, though features may be introduced by the nuclear form factors and instrumental effects, as seen in the xenon target spectrum in figure 1.3. Typical expected recoil energies are

10 to 100 keV, and the current exclusion curves for WIMP-nucleon scattering cross sections are pushing towards 10^{-44} cm^2. Since the total event rate and mean energy are so small and the spectrum falls quickly with energy, detectors should be sensitive to events as low in energy as possible, with 100 keV often quoted as the threshold above which the event rate becomes negligible.

Chapter 2

Background in Dark Matter experiments.

Dark Matter interactions are very rare events and transfer only small amounts of energy to the detector. Dark matter detectors are radiation detectors and thus produce a signal when any kind of radiation interacts in their active volume. At energies below 100 keV, the rate of background events from radioactive decays in the detector materials and from cosmic radiation is typically many orders of magnitude larger than the expected signal. The sources of these background events and techniques to reduce their rate will be discussed here with a focus on the DEAP experiment.

2.1 Sources of radioactive background

2.1.1 Primordial isotopes

Primordial isotopes are long-lived radioactive isotopes that were already present in the material from which the earth was formed[26]. The most important of these isotopes in terms of detector background are ^{232}Th and ^{238}U[32], which have long decay chains shown in figures 2.1 and 2.2, emitting gamma radiation up to 2.6 MeV in energy, alpha particles between 5 and 8 MeV, beta and neutron radiation. Uranium and thorium are omnipresent in ores, and detector components can easily be contaminated if their production processes included ores, coal or other mined materials[32].

^{222}Rn and ^{220}Rn are the most notable daughters of primordial uranium and thorium, due to their ability to diffuse out of the material the parent isotope was in and into neighbouring materials. Both radon isotopes alpha-decay to polonium, a metal, which is often ionized after the decay and adheres to dust and solid surfaces. While the ^{220}Rn chain reaches a stable isotope within several hours, ^{210}Pb from the ^{222}Rn chain can remain on surfaces with a 22 year halflife where it provides a continuous source of alpha emitting ^{210}Po.

The alpha particles emitted are usually stopped within the bulk material and can only cause direct backgrounds if the parent isotope is located in the active volume of a detector or in the first few tens of micrometers of the material surrounding the active volume. However, alpha particles can also be absorbed in certain nuclei and cause the emission of energetic secondary neutrons in what is called an (α, n) reaction, which can propagate and interact in the active volume.

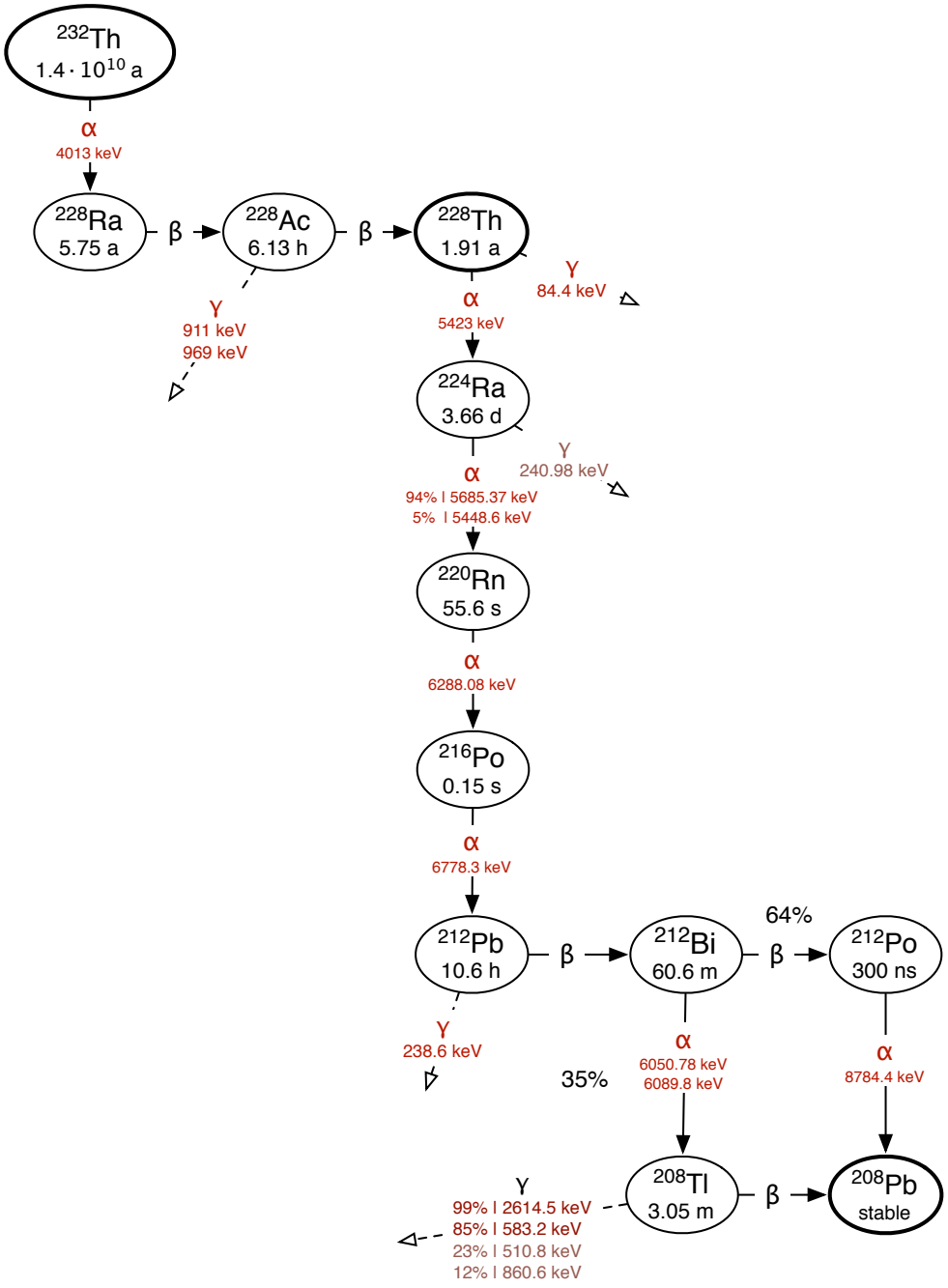

Figure 2.1: Decay chain of primordial thorium, indicating half-lives and decay energy (Q value). Data taken from [25], figure is author's own work.

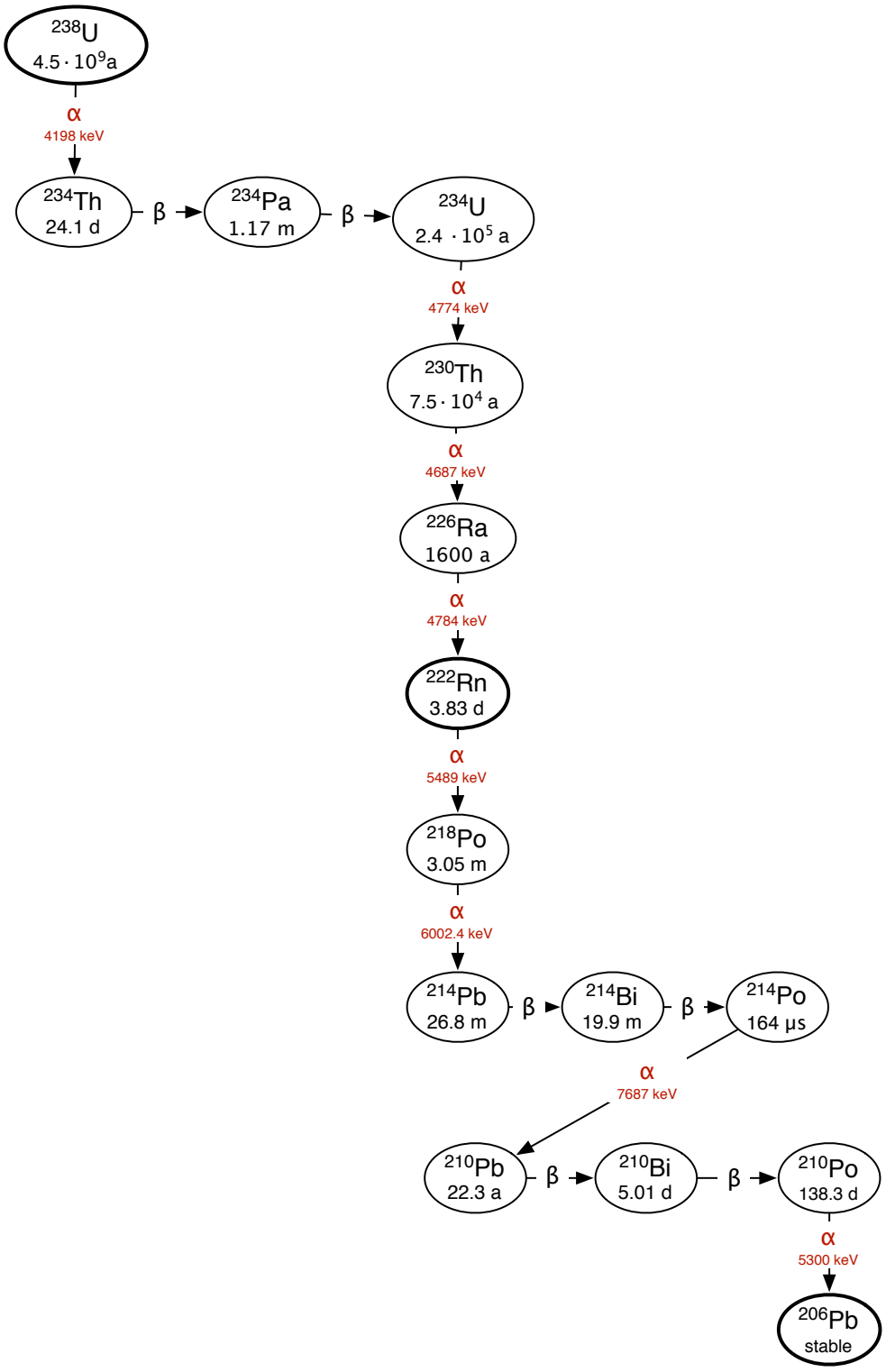

Figure 2.2: Decay chain of primordial uranium. Data taken from [25], figure is author's own work.

Another important primordial isotope is ^{40}K, which is often present in photomultiplier glass as well as in living organisms. It decays emitting beta as well as gamma radiation[54].

2.1.2 Cosmic radiation

Cosmic radiation consists of a constant stream of mainly protons and alpha particles at energies that can exceed 10^6 GeV[58], impacting the earth's atmosphere and creating hadronic showers, which at sea level consist mainly of muons and small numbers of pions, protons and heavier particles. The secondary products of cosmic radiation themselves are a source of background. They can also react with materials around the detector to turn stable isotopes into radioactive ones.

Cosmogenically produced isotopes are created in the interaction of cosmic radiation with materials on earth. The most important one for the DEAP experiment is ^{39}Ar, a beta emitter with a half-life of 369 years and a Q-value of 565 keV[25], which is constantly produced from ^{40}Ar in the atmosphere and therefore present in the liquid argon supply of the detector. The concentration of ^{39}Ar in natural argon is $8.1 \pm 0.3 \cdot 10^{-16}$ g/g, leading to an activity of $1.783 \pm 0.006 \cdot 10^{-3}$ Bq/l[49] or $3.3 \cdot 10^7$ decays per kg and year. A few percent of the beta decay events will be in the energy window of interest for WIMP search (10 to 25 keV recoil energy) and need to be suppressed[11].

High energy muons are often the last remaining component of cosmic radiation at locations deep underground. They can be efficiently detected using a so called "veto detector" before they enter the detector volume, so that a subsequent signal in the detector is known to be due to a muon passing through and is discarded, or

"vetoed". Muons themselves are thus not a major background concern[26]. However, muons can impact nuclei in material surrounding the detector and create spallation products such as neutrons, which do not registered in the veto detector.

2.2 Background reduction measures

Materials with a low specific activity (defined as the number of radioactive decays per second per mass of material) are called radio-pure. Strategies for obtaining radio-pure detector materials can be classified as prevention of contamination, cleaning and waiting out the decay.

In order to prevent the accumulation of ^{210}Pb on detector surfaces exposed to air, components are often built in a radon-reduced environment, such as a glove box filled with boiled off argon or nitrogen. Radon in liquid argon and nitrogen tends to stay in the liquid phase, so that the boiled off gas contains less radon than the liquid. Where this is not possible, ^{210}Pb can be removed by chemically dissolving or physically removing the outer layer of a component, as will be done for the DEAP-3600 acrylic vessel.

To prevent ^{210}Pb in the bulk material, the alpha particle from which can cause an (α,n) reaction with neutrons being emitted from the bulk, the factory where the material is made has to be kept clean of dust, and production processes that involve ores can sometimes be replaced in favour of such that do not.

Lead, which is a favourable shielding material against gamma radiation, is often inadvertently enriched in ^{210}Pb during production. In this case, "old lead" can be used in the detector. This is lead that was produced many hundreds of years ago, retrieved from for example from old water pipes or sunken ships, where the activity

of ^{210}Pb is strongly reduced because most of it has decayed by now.[32]

Argon that is depleted in ^{39}Ar can be obtained from geological underground gas reservoirs which have not been in contact with the atmosphere for many hundreds of years, so that most of the cosmogenically produced ^{39}Ar has decayed away. Efforts are underway to procure such depleted argon for use in DEAP-3600.

In order to be certain of their level of radio-purity, all materials used to build a dark matter detector are usually screened with high purity germanium detectors for content of isotopes from the primordial thorium and uranium chains[54].

Cosmic radiation as a primary background source can be reduced by placing the detector in underground caves or mines. The depth of the site is usually quoted as the depth of water which would give the same muon attenuation. The DEAP experiments are located at SNOLAB[22] in Sudbury, Ontario, which is currently the deepest large underground lab with 6000 m water equivalent (m.w.e.) shielding. Other underground labs are the Laboratoire Souterrain de Modane in France with 4000 m.w.e. and the Gran Sasso National Laboratory in Italy at 3000 m.w.e. depth.

The rock above an underground lab can be considered the first layer of detector shielding. Successive layers of shielding are often employed in an onion-skin type design, consisting typically of a water shield to moderate and stop low energy neutrons, and several layers of gamma shielding made from progressively radio-purer materials. In DEAP-3600, this is not necessary because the liquid argon is self-shielding (see Ch. 3.3). The shielding material, in particular also the rock in underground laboratories, itself is a source of neutrons from neutron producing interactions with cosmic muons, (α, n) reactions and natural fission processes of isotopes in the shielding, thus thicker shielding is not always better in terms of final detector backgrounds.

The types of shielding discussed so far are all passive shielding. In addition to this, active shielding can be employed, which involves instrumenting a volume surrounding the actual detector to detect particles travelling towards it from the outside. A muon veto is a type of active shielding, where either a scintillator or a water volume surrounding the detector is instrumented with photo multiplier tubes to detect the scintillation or Cherenkov light produced when muons pass through. This signal is then used to veto the detector. This does not remove any Dark Matter events, because the interaction probability for WIMPs is so small that the chance of one interacting in the veto volume and then in the active detector volume is negligible, though it can reduce the life-time of the detector significantly if the muon rate is high.

Even when properly shielded and located in underground laboratories, additional background suppression is necessary in all dark matter detection experiments. Of great advantage is the possibility to discriminate events from gamma or beta radiation, that is electromagnetic interactions, from the nuclear-recoil-like interactions expected for a WIMP signal. This can significantly reduce the overall level of background, leaving only neutrons and possibly degraded energy alpha particles as a source of background that could mimic dark matter signals.

The possibility to reconstruct the position of an event is additionally useful in reducing backgrounds, since radiation due to environmental radioactivity tends to enter the detector from the outside and, in a dense material such as liquid argon, background events are thus concentrated near the outside of the active volume, while WIMP events occur evenly throughout the detector.

Chapter 3

The DEAP detectors

3.1 Liquid argon as a detector medium

The DEAP detectors utilize liquid argon as both the absorber and detection medium for WIMP interactions. Liquid argon is a good absorber material for Dark Matter detection experiments because it can be purified easily and because it has a relatively high atomic number and is thus self shielding against external radiation. It is also relatively inexpensive so that a large target mass is financially feasible.

Liquid argon is also a good detection medium, scintillating with a competitive light yield and producing pulse shapes that allow for the use of pulse shape discrimination methods to separate nuclear recoil events from electromagnetic recoil events. As discussed in the previous section, the ability to separate nuclear recoil from electromagnetic recoil events is crucial for Dark Matter detection experiments.

DEAP uses a single phase detector design, where all the argon is in its liquid phase and only the scintillation signal is measured. This is as opposed to a two-phase design popular in experiments using xenon, where electrons separated from

their nuclei during an interaction are drifted out of the liquid and through a gas volume, and both the scintillation and ionization signals are measured. The two phase design has a somewhat better position resolution, because the time difference between the scintillation and charge signals provides information about the event position. However, depending on the particle type and electric field strength, the scintillation yield is reduced by 20% to over 50%[21], negatively affecting the discrimination power against electromagnetic events.

Table 3.1 qualitatively shows a comparison of the relative merits of the noble gases under consideration for Dark Matter detection experiments. The decay times of the two excited states that lead to light emission in liquid argon and neon are the most favourable out of all the noble gases for use in a single phase detector design, allowing for sufficiently good pulse shape discrimination (PSD) using only scintillation[12] (see next section). The decay times in Neon are 18 ns/14.9 us[59], in Kryton 2.0 ns/91 ns[43] and in Xenon $<$ 3 ns/34 ns[43]. The price is relevant when experiments need many tons of target material. The interaction cross-section is proportional to the square of the nuclear mass. The self-shielding power is proportional to the density. Finally, the level of natural contamination with radioactive isotopes determines the requirements for background reduction measures.

Gas	light yield	PSD	Price	Interaction cross-section	Radioactive contamination	self-shielding
Neon	x	xxxx	xxx	x	xxx	x
Argon	xxx	xxx	xxxx	xx	x	xx
Krypton	xx	xx	xx	xxx	x	xxx
Xenon	xxx	x	x	xxxx	xx	xxxx

Table 3.1: Relative merits of noble gases for Dark Matter search experiments. More x's are better.

3.1.1 Pulse shape discrimination

The passage of ionizing radiation through liquid argon ionizes and excites argon atoms, which can then form strong bonds with regular argon atoms, leading to ionized or excited dimers (excimers)[57]. Highly excited excimers quickly de-excite non-radiatively to lower energies[21].

Of the four lowest energy atomic states, the potential well necessary for excimer formation occurs for the $^3P_2$ and the $^3P_1$ states, so that two distinct excimer states arise: a singlet state $^1\Sigma_u \quad (^3P_1 +^1 S_0)$ and a triplet state $^3\Sigma_u \quad (^3P_2 +^1 S_0)$[57] (see Fig. 3.1). The decay of those excimers into the repulsive ground state is the origin of argon scintillation light, which at a wavelength of 128 nm[16] is not energetic enough to re-excite another argon atom and thus passes through the argon target unhindered. The argon experiences no permanent chemical change from the interaction.

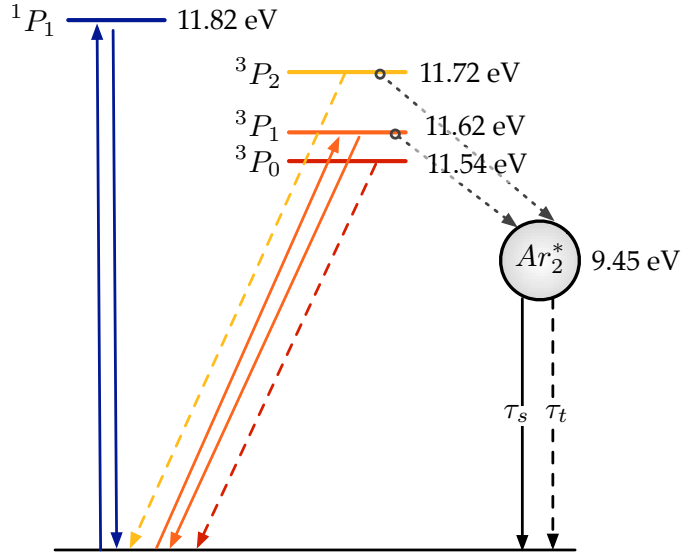

Figure 3.1: Excited states of the argon atom (after [69]). Dashed lines represent dipole forbidden transitions. Two of those states can form excited argon dimers with a ground state atom.

The singlet state decay is an allowed transition with a lifetime of 6.7 ns, while the triplet state decay is forbidden and thus has a much longer lifetime of up to 1600 ns (literature values range from 1000 to 1600 ns, possibly due to differing argon purities and temperatures)[35]. The fraction of excimers produced in the singlet and triplet state depends on the linear energy transfer dE/dx (LET) of the penetrating radiation[20][35]. The more energy is dissipated per unit track length, the more singlet excimers are produced. This means that electromagnetic interactions preferentially excite the argon excimer triplet state while nuclear recoils tend to excite the singlet state, which is the basis for the background suppression used in DEAP and other liquid noble gas experiments.

The large difference in decay times makes it possible to estimate the relative fraction of singlet and triplet excimers by comparing the scintillation pulse intensity in the first hundred or so nanoseconds to the intensity in the rest of the pulse. This fraction is then a good estimate of the LET of the exciting particle, and thus of the particle type.

3.1.2 Photon yield, quenching and scintillation light detection

The energy gap between the argon excimer and its ground state is too large for non-radiative transitions[21], so one could naively expect to measure a photon for every excimer produced. This is not the case due to the following photon reducing processes[21, 34]:

Biexcitonic quenching occurs at high LET, when a large number of excitons are produced in a small space and the chance of two of them colliding is considerable.

They undergo the reaction

$$Ar^* + Ar^* \rightarrow Ar + Ar^+ + e^-.$$

The ion and electron will then recombine and a photon is emitted, while the two excimers would have each emitted one photon had they not collided.

Escaping electrons are prevalent in the low LET region where only few atoms are ionized. If the electron becomes thermalised beyond a critical radius, it will not recombine in the time-window of the measurement so that no photon is detected.

Charge carrier trapping is independent of LET. It happens when, after ionization, the electron becomes attached to electronegative impurities, most notably oxygen, preventing recombination of electron and argon ion.

Electronic energy transfer to impurity atoms is a very effective process in liquid argon by which the excitation energy of an argon atom is transferred to an impurity atom[16][29]. Impurities such as nitrogen or water, which relax non-radiatively, considerably quench the scintillation light[44].

Two important considerations for experiments using liquid argon arise from these effects: The liquid argon used in the detector must be as pure as possible, and an energy calibration done for one type of radiation will not be correct for a type of radiation with a different LET.

The introduction of only 2% nitrogen into the argon reduces the scintillation output by 50% [44]. DEAP-1 uses grade 5 purity argon gas that is further purified to contain less than 0.1 parts per billion of most impurities[12].

For practical reasons, gamma sources are usually used for detector calibration, leading to an "electron equivalent" energy scale denoted as [keVee]. Particles with a higher LET, such as alpha particles or recoil nuclei, produce less light for the same energy transfer. The light is quenched and the quenching factor relates the energy calibration for gammas to that of other particle types. An energy calibration corrected for nuclear recoil events is denoted as [keVr]. Relevant quenching factors and other scintillation properties of argon are summarized in table 3.2.

W value (liquid)	$23.6^{+0.5}_{-0.3}$eV[55]
W_{ph}	19.5 ± 0.4eV[21]
Scintillation wavelength (peak value)	128 nm
Attenuation length (own scintillation light)	66± 3 cm[39]
Alpha quenching factor	0.7[20]
Nuclear recoil quenching factor	0.25 [28]

Table 3.2: Liquid argon properties. The W value is the average energy required to produce one electron-ion pair and W_{ph} is the average energy required to produce one scintillation photon.

While the liquid argon is transparent to its own scintillation light, materials such as acrylic and glass are not. In order to detect the light then, it needs to be shifted to a longer wavelength. The organic wavelength shifter 1,1,4,4-tetraphenyl-1,3-butadiene (TPB) has long been the preferred material for this purpose. TPB of about 1 μm thickness is around 100% efficient at absorbing UV light[52] and re-emits it at 440 nm[18], where glass and acrylic are transparent and where most photo multiplier tubes are most sensitive. Additionally, the decay time of TPB is less than a couple of nanoseconds[31] so that it does not distort the timing characteristics of the liquid argon scintillation pulses.

3.2 The DEAP-1 series of prototype detectors

Noble liquids have been used as detector media since the 1950s, in calorimeters and time projection chambers, and their properties are well-studied[19]. A Dark Matter search experiment however has new requirements concerning purity, detector size and background discrimination power. It was therefore important for DEAP to establish experimental procedures and background reduction techniques using a number of prototype detectors before setting out to build a large scale detector. Several versions of the DEAP-1 prototype detector have been built and operated at Queen's University and at SNOLAB since 2006 for this purpose.

A schematic drawing of the DEAP-1 detector is shown in Fig. 3.2. All versions of

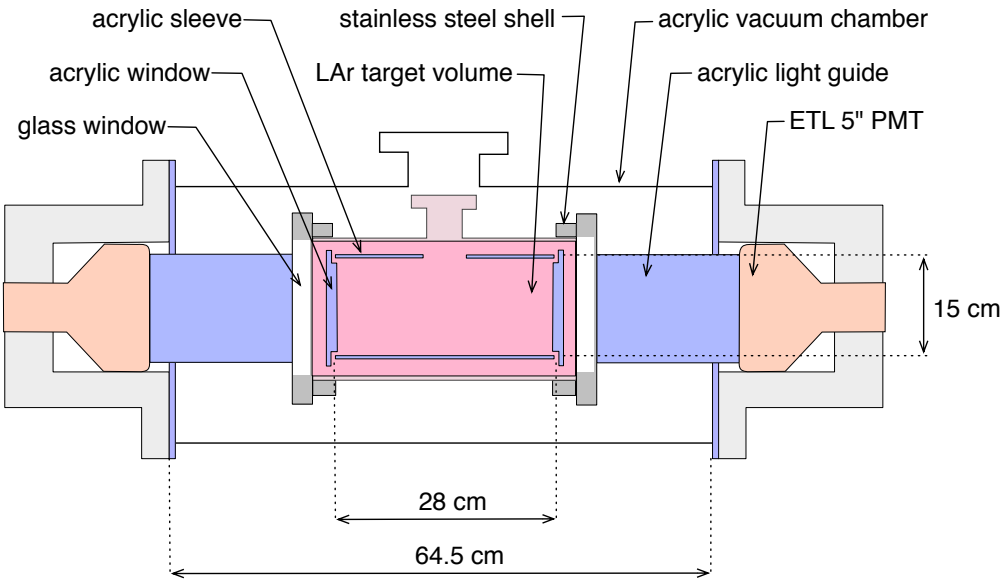

Figure 3.2: Schematic drawing of the DEAP-1 detector.

DEAP-1 have as their central interaction region a cylindrical volume of liquid argon, 28 cm long with a diameter of 15 cm, defined by an acrylic sleeve 0.36 cm thick. The sleeve is coated on the inside by vacuum deposition with a typically 1-3 µm thick

layer of TPB (see Sect 3.1.2).

The acrylic sleeve is surrounded by a diffuse reflector and contained in a cylindrical stainless steel vessel with glass windows at each end. The total mass of liquid argon inside the vessel is 7.6 kg. Acrylic light guides with photomultiplier tubes (PMTs) at their ends are loosely attached to the glass windows. The light guides serve three purposes: They absorb radiation from radioactive decays in the PMT glass, they thermalize neutrons from (α,n) reactions through collisions with hydrogen atoms in the acrylic, and they thermally insulate the PMTs from the liquid argon volume thus allowing them to be operated at room temperature, which improves their efficiency.

An opening at the top of the acrylic and stainless steel cylinders leads to the "neck", a pipe through which liquefied argon is filled into the detector. For a more detailed description of the liquid argon process system and detector hardware see Ref. [12].

Several iterations of DEAP-1 have led to improved backgrounds:

DEAP-1 version 0: The original DEAP-1 detector was operated at Queen's University in 2006. The acrylic sleeve in this iteration was sanded by hand on the inside using P150-grit (100 micron average diameter) aluminum oxide paper in order to remove radioactive deposits from the decay of ^{222}Rn in the air. This was done in a glove box under nitrogen atmosphere to prevent new deposits of radon daughters on the sanded surface. TPB was evaporated onto the inside of the sleeve, and the outside was painted with BC-620 (TiO_2) reflective paint.

5" ETL 9390B (flat-face) PMTs were used to detect the scintillation light. The waveforms from the PMTs were read out using a LeCroy WavePro7100 digitizing oscilloscope.

V0 stands for 3 main data taking periods between November 2006 to October 2007 on surface at Queen's University.

Version 1: In order to reduce the backgrounds measured in the V0 detector, the detector was moved to SNOLAB to be operated underground. A large rate of radon alpha events were observed in V0, so the sandpaper to be used to sand the sleeve was assayed for radon and the cleanest one chosen for sanding the V1 chamber. A PTFE reflector was wrapped around the sleeve replacing the BC-620 paint, which was found to have high radon emanation.

V1 was operated from December 2007 to December 2008

Version 2: After finding that the radon alpha rate increases after each re-fill of the detector with liquid argon[60, 48], an activated charcoal radon trap was installed in the argon fill line to further remove radon and daughters present in the liquid argon supply.

The waveforms from the PMTs were read out using the CAEN V1720 digitizer and MIDAS data acquisition system (DAQ). This allowed for a higher data taking rate and will also be the system used in DEAP-3600.

V2 took data with the oscilloscope from March to July 2009 and with the MIDAS DAQ from July to December 2009.

Version 3: To deal with the remaining background in the detector, at this point believed to be from surface events (See Sect. 6), the sleeve was coated with purified acrylic monomer at a thickness of about 100 µm[45], rather than sanded. The TPB for coating the sleeve and windows was preheated to evaporate all contaminants with

lower evaporation temperature.

The same Hamamatsu R5912 8 inch high quantum efficiency PMTs that will be used in DEAP-3600 were installed, which required also replacing the light guides to accommodate the larger spherical PMT shape.

V3 took data from March to September 2010.

Version 4: No significant reduction in backgrounds was achieved with V3, and a new hypophesis of geometric backgrounds was developed (see Sect. 7). To reduce this type of background new windows were machined to more tightly fit the acrylic sleeve, and a plug was designed to fit in the neck. The sleeve was again sanded, since coating in acrylic was a time intensive procedure and the surface background this was meant to address was found not to be a dominant source of background.

Analysis of V4 data showed that the light yield was very unstable, and was significantly different for the two PMTs. After disassembling the chamber, no mechanical problems were found, and the most likely explanation was bubbles of gaseous argon trapped behind one of the windows while the detector was filled changing the optical properties on that side.

V4 took data from November 2010 to February 2011

Version 5: Preliminary analysis of the background rate in V4 was promising, thus a decision was made to modify the acrylic windows again to fit less tightly (to allow for flow of argon gas) and to attempt another run. Some instability related to the argon flow through the detector was observed, but some good data could be obtained.

V5 took data from June 2011 to April 2012.

Table 3.3 lists some properties of the different DEAP-1 detector versions that are

relevant for the following chapters.

Detector	TPB thickness [μm]		Light yield [pe/keVee]
	on windows	on sleeves	
V2	2.8	1-2	2.4
V3	0.9	2-4	4.7
V5	0.9	4-5	3.8

Table 3.3: Summary of DEAP-1 detector version properties relevant for later chapters. The light yield is for 60 keV gamma events from an AmBe source.

3.3 The DEAP-3600 detector

A drawing of the DEAP-3600 detector is shown in Fig. 3.3. The detector is under construction at SNOLAB and expected to be operational by 2013.

The inner acrylic vessel of the DEAP-3600 detector has a radius of 85 cm and is filled with 3600 kg of liquid argon. After a fiducial volume cut (removing events that reconstruct near the surface of the detector) used to reduce background events from outside the detector, the active detector mass will be 1000 kg in the central detector region. Like the DEAP-1 vessel, the DEAP-3600 acrylic vessel will be coated on the inside with the wavelength shifter TPB to shift the LAr scintillation light to the visible spectrum.

Light guides 19 cm in diameter and 50 cm long are attached to the acrylic vessel. They are long enough to absorb most of the neutrons emitted from the PMT glass and serve as thermal insulation to allow the 255 8 inch Hamamatsu R5912 PMTs to be operated at -30° C. Filler material between the light guides (high density polyethylene) adds to the neutron shielding.

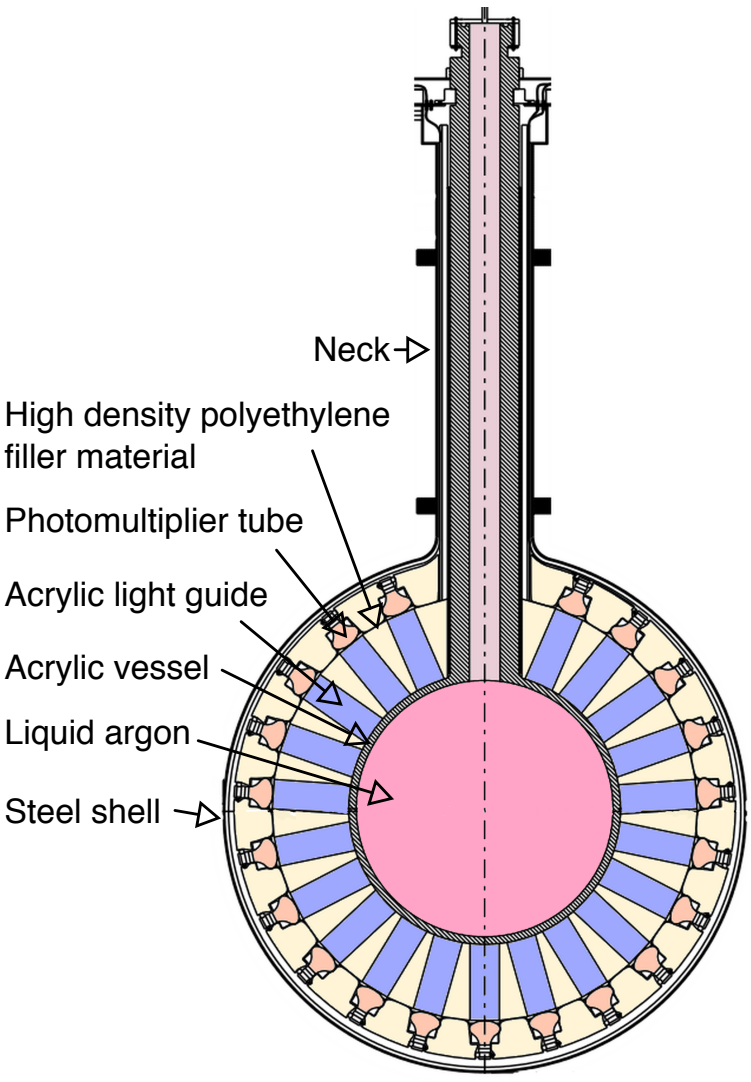

Figure 3.3: DEAP-3600 detector design.

A stainless steel shell supports the acrylic vessel and seals it from the shielding water in the 8 m diameter shielding tank the sphere is immersed in. This volume of water shields the detector from residual external neutrons originating from (α,n) interactions in the surrounding rock, and also reduces the flux of external gamma rays toward the detector. The water tank is lined with a white diffuse reflector and instrumented with 48 Hamamatsu 1408 PMTs to detect Cherenkov light from passing muons, and thus in addition to the passive shielding serves as an active muon veto system.

The neck at the top of the detector is used to insert the LAr and allows access to the interior of the vessel for cleaning, applying the TPB, and calibration. The first 50 cm of the neck consist of a piece of acrylic bonded to the vessel, the rest of the length is made from steel. This allows liquid argon to rise into the neck.

As mentioned in section 3.1, even small amounts of nitrogen in the liquid argon can considerably quench the scintillation light. A glove box made from a cylindrical, stainless steel vacuum vessel is situated at the top of the neck allowing the introduction of equipment into the detector without introducing air.

Chapter 4

DEAP-1 background data

4.1 Automated analysis

When a photon hits a PMT's front face, a photo electron (PE) is freed, multiplied within the PMT and eventually, a voltage signal can be measured that is proportional to the amount of light incident on the PMT's front face. Every time the voltage measured on both DEAP-1 PMTs simultaneously passes a fixed threshold, the voltage versus time is recorded for both PMTs for 16 μs. Those PMT traces are analyzed in an offline analysis. A typical trace for a nuclear-recoil-like event between 120 and 240 PE is shown in Fig. 4.1.

For each trace, the baseline is calculated and subtracted, the location of the peak of the pulse shape is found and the charge in the prompt and in the late time window is calculated by integrating the voltage from -50 ns to 150 ns (PCh) and from 150 ns to the end of the trace (LCh), where 0 ns is at the peak. The data from both PMT traces is then combined to calculate the total number of photo electrons in the event (TotalPE) using the known charge of a single photoelectron (SPE charge) and the

location of the event along the axis of the detector (Zfit). Also calculated is the so called "prompt fraction", or Fprompt, the charge in the prompt window divided by the total charge in the trace.

$$\text{Charge0,1} = \text{PCh0,1} + \text{LCh0,1} \tag{4.1}$$

$$\text{TotalPE} = \frac{1}{\text{spe}}(\text{Charge0} + \text{Charge1}) \tag{4.2}$$

$$\text{Zfit} = \text{L} \cdot \frac{\text{Charge0} - \text{Charge1}}{\text{Charge0} + \text{Charge1}} \tag{4.3}$$

$$\text{Fprompt} = \frac{\text{PPE0} + \text{PPE1}}{\text{Charge0} + \text{Charge1}} \tag{4.4}$$

where L is the length of the detector chamber, spe is the SPE charge and 0 and 1 stands for the two PMTs.

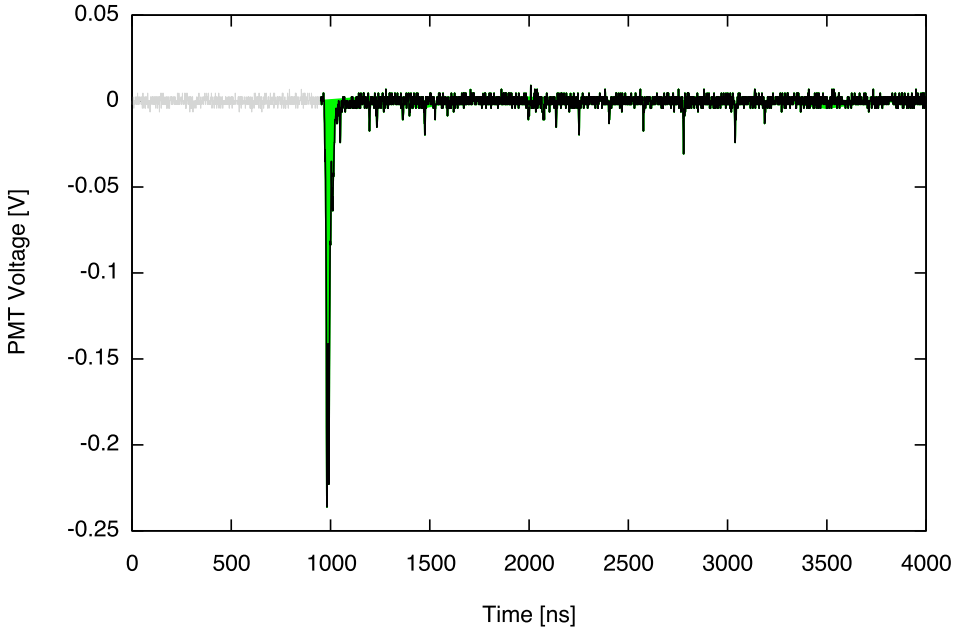

Figure 4.1: Typical nuclear-recoil-like PMT trace. The liquid argon scintillation pulse is drawn in black.

4.2 Run types

The following types of data runs were normally taken with DEAP-1:

PSD Data is taken with a tagged ^{22}Na source irradiating the detector. An additional PMT coupled to a plastic scintillator behind the source provides the tag. A triple coincidence between the back PMT and the two DEAP PMTs is required for a signal to be fed to a single channel analyzer, which passes only events in the energy window of interest to be written to file. This way, only events from gamma interactions in the region of interest are recorded for PSD studies.

^{22}Na full spectrum This is an energy calibration run where the full spectrum of the ^{22}Na source is recorded. It is similar to PSD runs but events of all energies are recorded.

Neutron The detector is irradiated by an americium-beryllium source which emits neutrons and 60 keV gammas. These runs are used for energy calibration and to find the mean Fprompt value of the nuclear-recoil-like events.

Physics Data is taken without any source near the detector. This data is used to study backgrounds and for calculating WIMP cross section limits.

Pulser Pulser runs use a random pulse generator to trigger readout of the PMTs. This data is used to evaluate electronic noise.

Flasher A dedicated, pulser driven LED source is used to illuminate each PMT. This data is used to evaluate the SPE charges.

Engineering Data taken to test new electronics components. Not used for data analysis.

4.3 PSD and background data

DEAP relies on pulse shape discrimination (PSD) to separate nuclear recoil from electron recoil events. The pulse shape discrimination parameter Fprompt is shown in Fig. 4.2 versus TotalPE or energy for events from a Neutron run. Two populations of events are visible forming the nuclear recoil band at an Fprompt of about 0.8 and the electron recoil band at an Fprompt of about 0.3. The width of the bands increases toward lower TotalPE due to lower statistics, so that they start to leak into each other.

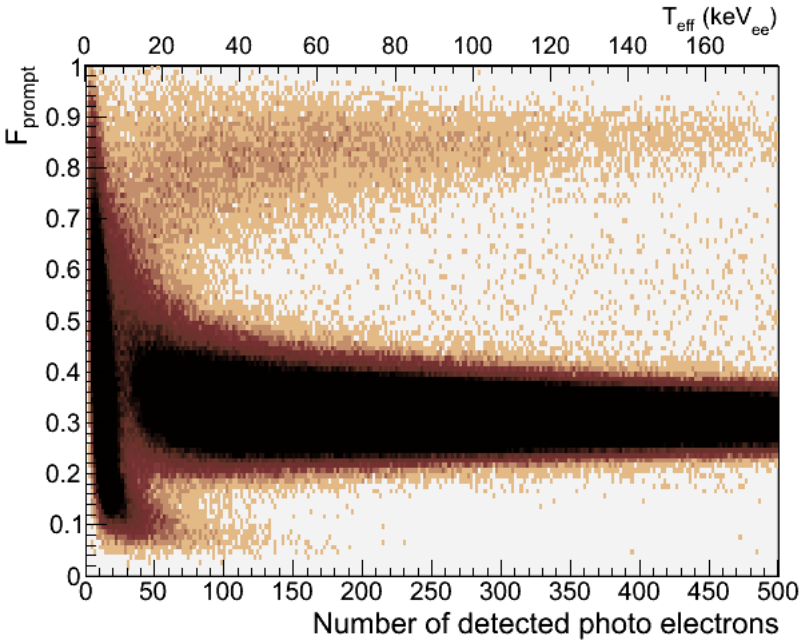

Figure 4.2: The discrimination parameter Fprompt versus TotalPE for events from a Neutron calibration run (V2 data).

In order for the DEAP-3600 experiment to succeed in obtaining a competitive WIMP limit, or in detecting a statistically significant WIMP signal, the background rate, that is the event rate in the nuclear recoil band at low energies, must be low

enough. The collaboration aims for less than 0.6 background events in a three year run in the region of interest.

The region of interest (ROI) for WIMP search is a two dimensional window in Fprompt and TotalPE. The Fprompt window is chosen based on the desired recoil acceptance. The exact Fprompt value this corresponds to in DEAP-1 is different for each version of the detector. The TotalPE window has a lower limit at about 120 PE due to statistical considerations, and we usually choose the upper limit as twice the lower one.

The DEAP-1 physics run data showed a number of event populations in the nuclear recoil band, which will be the topic of the following chapters.

Figures 4.3 and 4.4 show the events in the nuclear recoil band for DEAP-1 V2, V3 and V5, one with Fprompt versus TotalPE and one with Zfit versus TotalPE. For all three detector versions, nuclear-recoil-like events occur at all energies from the detector energy threshold up to about 8 MeV.

Several event populations emerge in these plots, labelled A to D. Note that the livetimes are different for the different data sets and quoted for each one on the plot in days.

The populations A in each plot at 5000 to 8000 TotalPE will be shown to be full energy alpha decays from radon. Alpha particles have an Fprompt value similar to neutrons, and thus are in the nuclear recoil band. Radon can enter the argon supply by emanating out of storage tanks and the gas handling system.

The radon chain alpha particles all have energies in excess of 5 MeV, much more than the WIMP events the experiment is designed to detect. Full energy alpha events, located in the active liquid argon volume from which all scintillation light reaches the

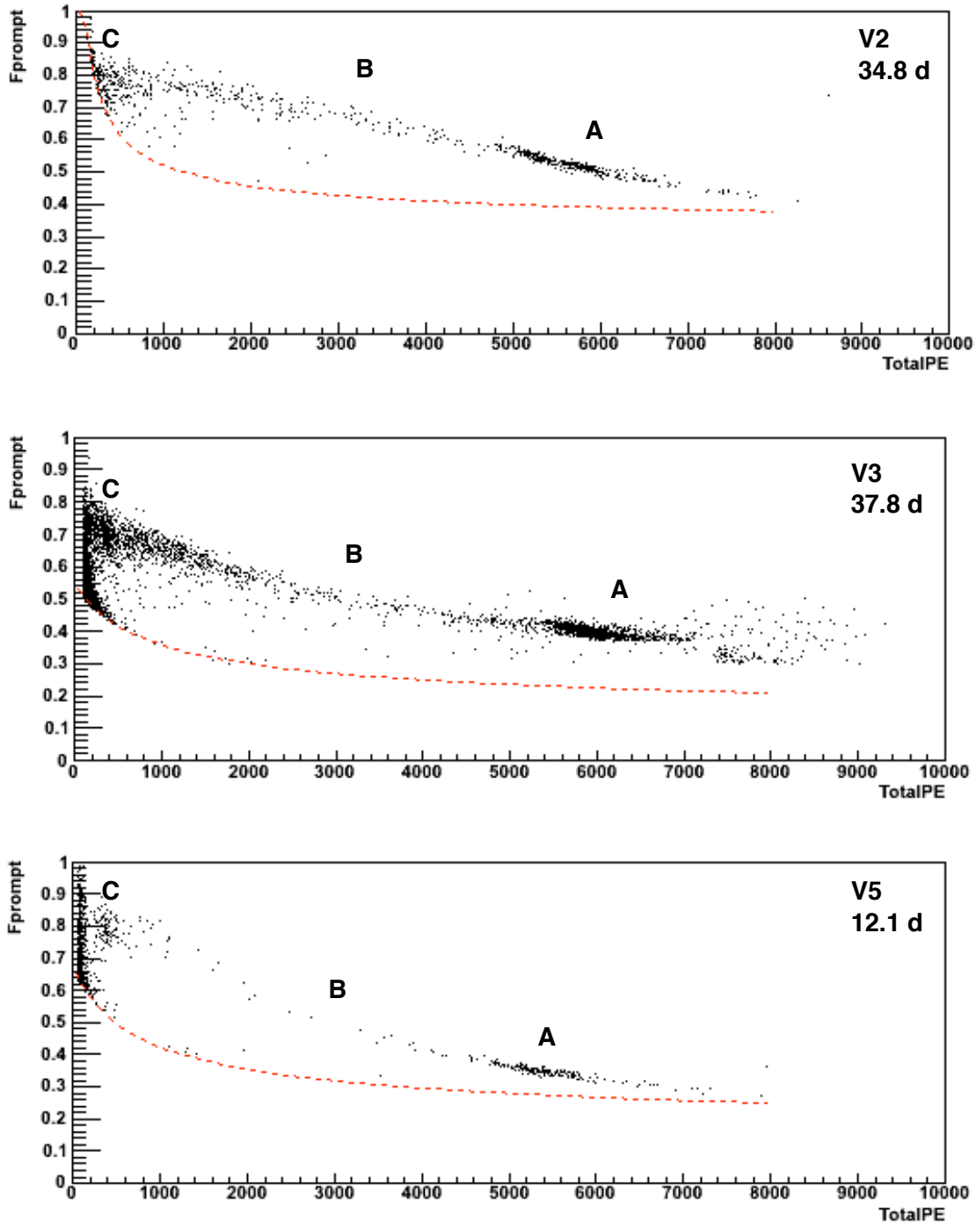

Figure 4.3: Fprompt vs. TotalPE for all nuclear-recoil-like events in the center of the detector. Events below the dotted line are from electromagnetic interactions and were removed. The band drops to lower Fprompt with higher event energy due to saturation of the PMTs.

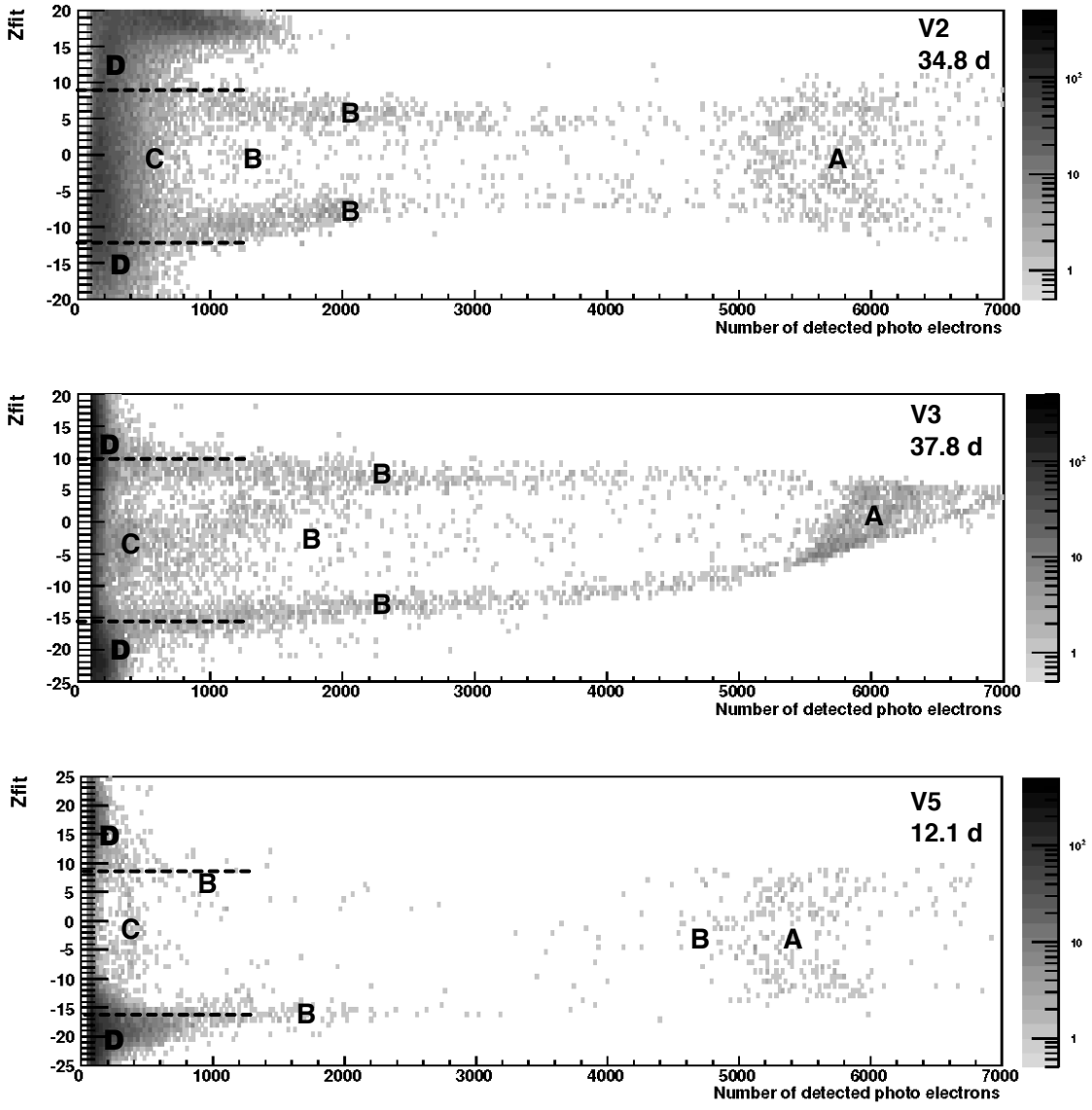

Figure 4.4: Zfit vs. TotalPE for nuclear-recoil-like events. The dashed line corresponds to the approximate location of the windows at low energies. These are not at constant Zfit at higher energies due to saturation of the PMTs.

wavelength shifter, can thus be readily discriminated based on their energy. Full energy alpha events are the topic of chapter 5. Despite not presenting a source of background in the region of interest directly, they are the key to understanding the dominant source of background in V2 and V3, and by quantifying their contribution to the high energy spectrum one can put constraints on the level of surface backgrounds.

Surface alpha events come from alpha emitters on the surface and in the first 80 μm of the acrylic vessel. Alpha particles from these isotopes lose some of their energy on their way out of the acrylic and/or the TPB, so that only a fraction of their original energy is available to excite the argon. These "surface backgrounds" have an energy spectrum stretching all the way from zero to the full energy of the alpha particle, and thus need to be understood and if possible reduced to guarantee the success of the experiment. Surface backgrounds dominate the background rate in V5, in particular event population C was found to be due to these, and are discussed in chapter 6.

Population B in figure 4.4 was found to be mainly from geometric alpha events, from what we call gap alphas, which occur when alpha particles excite the liquid argon outside of the active volume, in an area of the detector from where not all light can reach the PMTs. The visible event energy is then lower than it should be and the spectrum can again stretch down to the energy region of interest. V2 and V3 background is dominated by those events and they are discussed in chapter 7.

Population D events reconstruct outside of the detector and are poorly understood. They might be due to scintillation in the oil used to couple the PMTs to the light guides or Cherenkov radiation in the PMT or window glass.

Chapter 5

High energy background events

5.1 Timing coincidence tags indicative of radon daughters

Event population A from Fig. 4.3 was expected to be due to alpha decays from the radon chain. Re-printed in Fig. 5.1 are parts of the primordial uranium and thorium chains (see Sect. 2) starting at the radium isotopes.

A few isotopes in these chains have short half-lives suitable for coincidence tagging, whereby one looks for pairs of events within a time window less than a few times the half-life of the intermediate isotope, and "tags" them. The presence of such tagged pairs can confirm the origin of these events and allows one to directly determine the radon decay rate in the detector.

When performing such a timing coincidence analysis one looks for the number N_c events that are correlated in time out of a certain total number of pairs of events (N_{all})

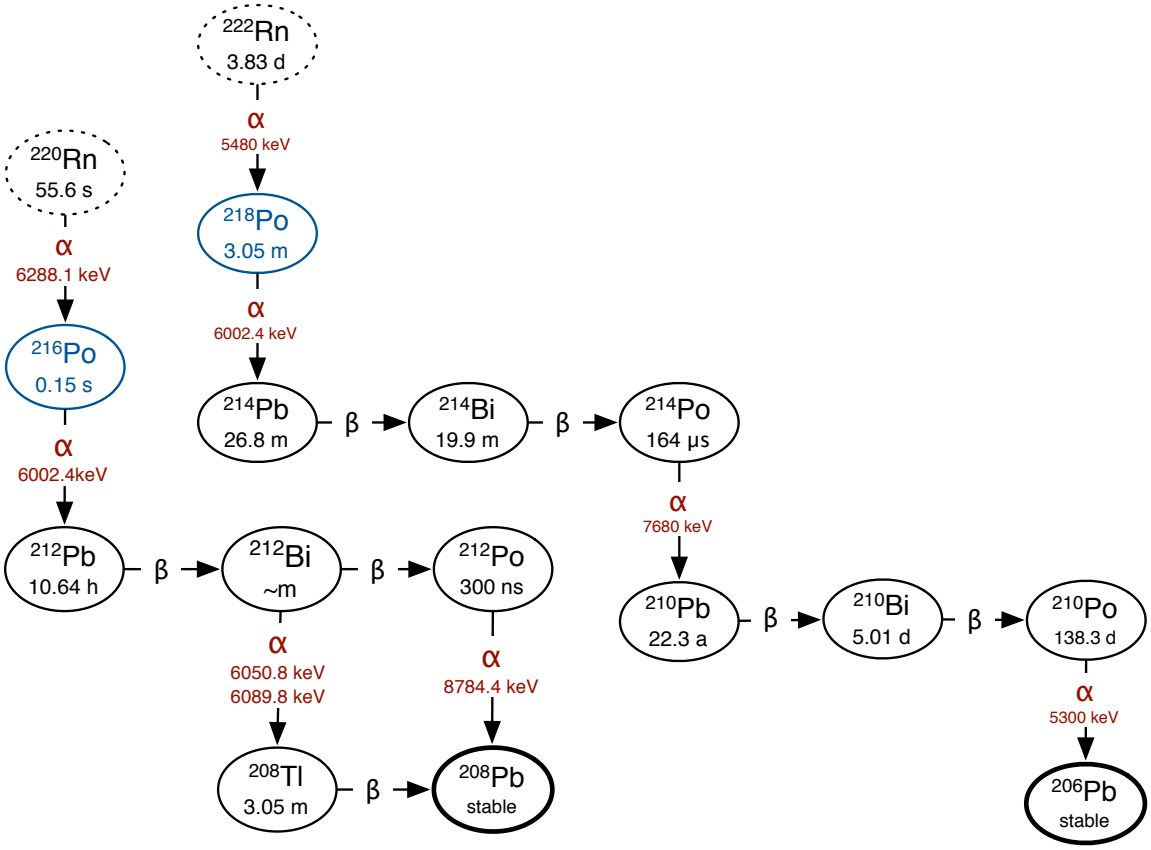

Figure 5.1: Decay chains of ^{224}Ra and ^{226}Ra.

which contains mostly uncorrelated events (N_u). Each set of high energy nuclear-recoil-like events subsequent in time is considered a pair. The number of tagged event pairs (N_{tag}) contains both correlated and uncorrelated events that occurred within the tag time window Δt due to random coincidences (N_r).

The number of expected random coincidences N_r can be calculated using a well known equation,

$$N_r = N_u \cdot (1 - e^{-N_u \cdot \Delta t/T}) \tag{5.1}$$

$$= (N_{all} - N_c) \cdot (1 - exp\{-(N_{all} - N_c) \cdot \Delta t/T\}) \tag{5.2}$$

where T is the total time over which the data was taken.

Only N_{all} and N_{tag} are immediately known. If there are about three times more uncorrelated than correlated events, N_c is small and N_u can be approximated by the total event number, N_{all}, without introducing a large error. The number of real coincidences can then be easily found as the difference between the number of tagged and the number of random coincidences.

A situation might arise where most of the events under consideration are expected to be real coincideces, so that the above approximation is not valid and the full equation needs to be evaluated. The number of actually correlated events, written in terms of only known quantities, is

$$N_c = (N_{tag} - N_r)/\epsilon \tag{5.3}$$

$$= (N_{tag} - (N_{all} - N_c) \cdot [1 - exp\{-(N_{all} - N_c)/T \cdot \Delta t\}])/\epsilon \tag{5.4}$$

where ϵ is the tag efficiency. This equation has no analytic solution, however an

iterative solution can be found:

$$N_c^{(1)} = (N_{tag} - N_{all} \cdot (1 - exp\{-N_{all}/T \cdot \Delta t\}))/\epsilon \tag{5.5}$$

$$N_c^{(2)} = (N_{tag} - (N_{all} - N_c^{(1)}) \cdot (1 - exp\{-(N_{all} - N_c^{(1)})/T \cdot \Delta t\}))/\epsilon \tag{5.6}$$

$$... \tag{5.7}$$

$$N_c^{(n)} = (N_{tag} - (N_{all} - N_c^{(n-1)}) \cdot (1 - exp\{-(N_{all} - N_c^{(n-1)})/T \cdot \Delta t\}))/\epsilon \tag{5.8}$$

With a convergence criterion of a change smaller than 0.1 events per step, this converges after 6 to 11 iterations in our data. I used this method in the analysis of all background data.

I calculate the uncertainty using only the first step:

$$\epsilon N_{Rn} = N_{tag} - N_{all} \cdot (1 - exp\{-\frac{N_{all}}{T} \cdot \Delta t\}) \tag{5.9}$$

$$\epsilon(\Delta N_{Rn})^2 = (\frac{\partial N_{Rn}}{\partial N_{tag}} \Delta N_{tag})^2 + (\frac{\partial N_{Rn}}{\partial N_{all}} \Delta N_{all})^2 \tag{5.10}$$

$$= N_{tag} + (e^{-r \cdot \Delta t} \cdot (e^{-r \cdot \Delta t} + r \cdot \Delta t - 1))^2 \cdot N_{all} \tag{5.11}$$

When choosing the tag time window, one has to weight the expected number of random coincidences against the chance of missing some real coincidences. Making the time window long will lead to nearly all real coincidences being tagged, but a lot of random coincidences will be included as well. The percentage of real coincidences missed for a time window Δt and an isotope with a half life of $\tau_{1/2}$ is

$$1 - \epsilon = \frac{N}{N_0} = e^{-\Delta t \cdot ln(2)/\tau_{1/2}} \tag{5.12}$$

Both ^{220}Rn and ^{222}Rn decays can be tagged, due to the relatively short half-lives of their daughter polonium isotopes. The ^{220}Rn tag time window I use is $0 < \Delta t < 0.5$ s, which has an efficiency of about 90%. The ^{222}Rn tag has a time window of $0.5 < \Delta t < 500$ s with corresponding efficiency of $\epsilon = 85\%$. The lower limit was

chosen to exclude ^{220}Rn events. All radon event numbers quoted are corrected for random coincidences and tag efficiency. The number of ^{222}Rn coincidences in the ^{220}Rn tag time window is negligible.

5.2 Rates of ^{220}Rn and ^{222}Rn in DEAP-1

Using the method described above on the populations A in Fig. 4.4, the radon decays in every background run were tagged. As shown in Fig. 5.2, the rates were stable over many months and were not affected by the switch from V2 to V3 indicating a sustained source of radon.

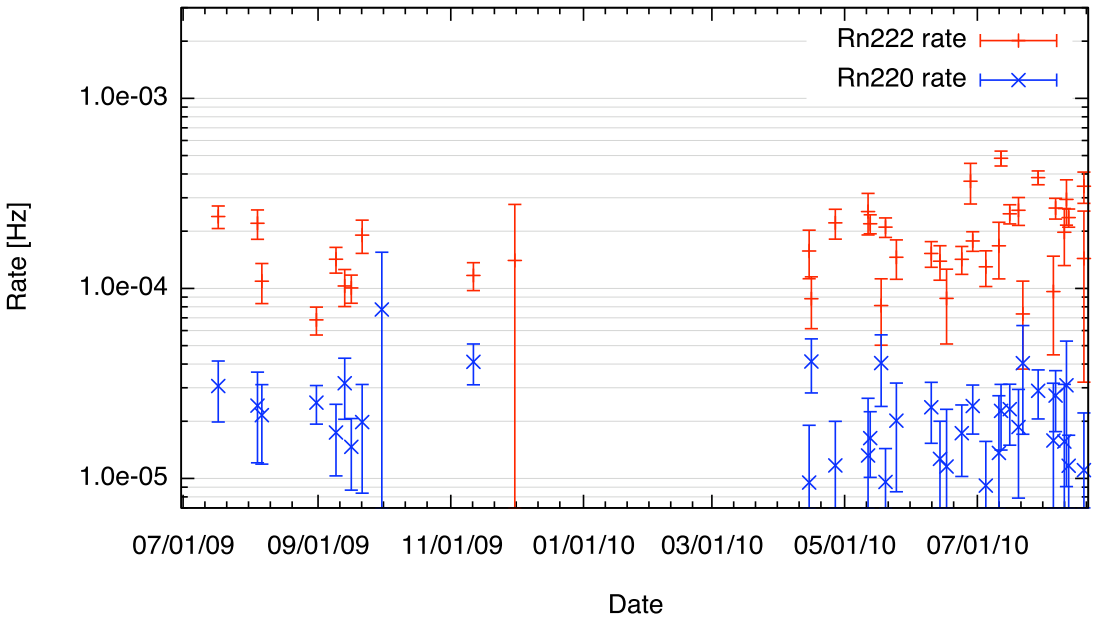

Figure 5.2: Run by run tagged radon decay rates. V2 runs are to the left and V3 runs to the right of the gap.

The average rates for each run are presented in Tab. 5.1. Data in V3 was taken with high and low voltage on the PMTs to increase the dynamic range. Numbers

are quoted for both separately to make comparison with the spectra fits in the next subsection easier.

Version	Run time (d)	^{222}Rn tags	^{220}Rn tags	^{222}Rn rate [10^{-5}Hz]	^{220}Rn rate[10^{-5}Hz]
V2	34.8	349 ±22	77 ±7	11.6 ±0.7	2.56 ±0.21
V3 LV	14.0	199 ±17	27 ±5	16.3 ±1.4	2.23 ±0.43
V3 HV	37.8	599 ±29	62 ±8	18.3 ±0.9	1.90 ±0.24
V5 LV	13.4	135 ±13	16 ±4	11.6 ± 3.5	1.5 ±0.3

Table 5.1: Number of tagged radon decays in DEAP-1 V2, V3, and V5. LV and HV stand for low voltage and high voltage runs respectively.

5.3 Is it really radon?

One might wonder what evidence there is that the tags in the above subsection indeed count radon events. One way to verify this is to look at the timing spectrum between the high energy events. I fitted two regions in time indicative of ^{220}Rn and ^{222}Rn with an exponential function, and the lifetimes fitted out are consistent with those of ^{218}Po and ^{216}Po. The timing spectra and their fits are shown in Fig. 5.3.

Another thing I looked for is the electron signal from the decay of ^{212}Bi to ^{212}Po followed by an alpha. If the above tags are really from the radon chains, such events should be present. The lifetime of the ^{212}Po is only 300 ns, so that these two events will appear in the same pulse shape in our data. Looking at all the high energy pulse shapes in a subset of runs, I found a number of such pulses consistent with what was expected from the number of tagged ^{220}Rn decays in the same data set.

I also looked for signatures of ^{224}Ra in the data, being the parent of ^{220}Rn. If radium was decaying to radon in the active detector volume, each $^{220}\text{Rn} \rightarrow {}^{216}$Po tag should be preceded by another alpha event within less than 3 s. The rate of these

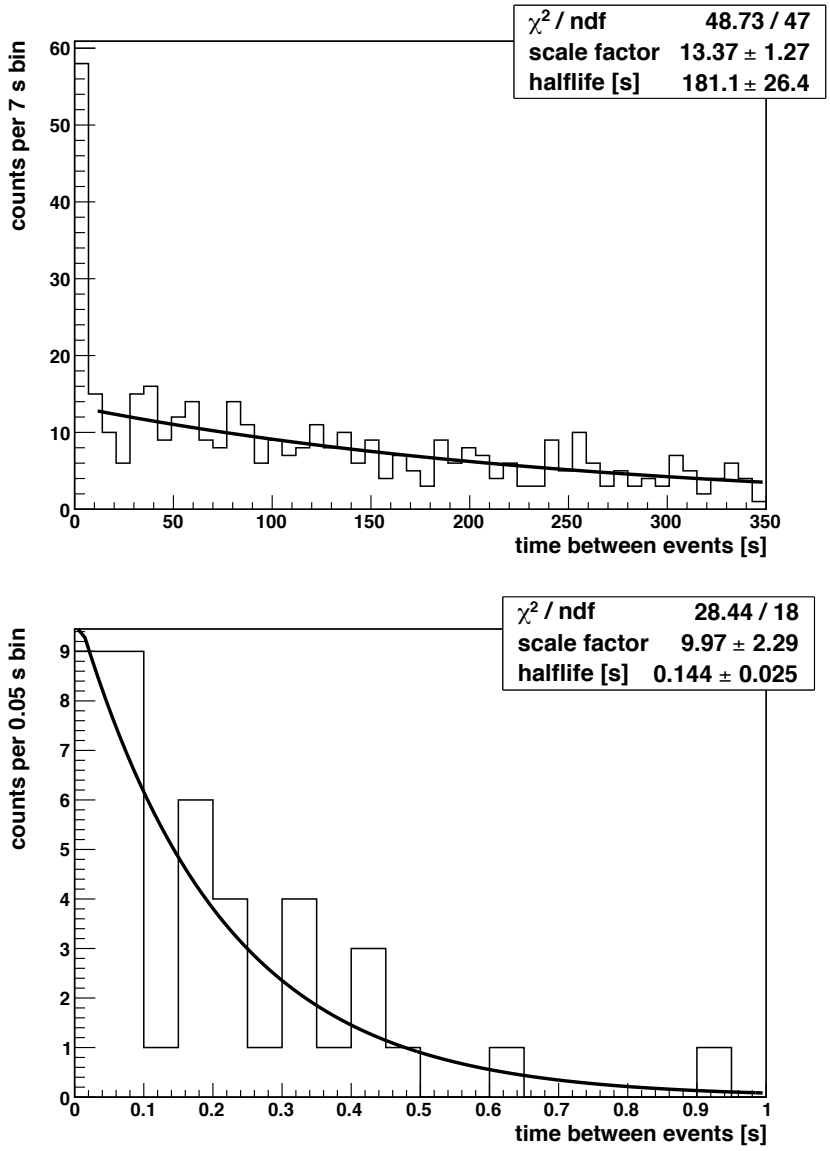

Figure 5.3: Timing between high energy events. Top: Fit from 10 to 350 seconds. Bottom: Zoomed in on the large bin at the first second of the top plot and fit from 0 to 1 s. The lifetimes fitted out are consistent with those of ^{218}Po (top) and ^{216}Po (bottom).

triple coincidences is consistent with random coincidences, and the energies of the events found is not consistent with ^{224}Ra. I thus conclude that there is no ^{224}Ra in the active volume of the detector. There is evidence for ^{224}Ra being present outside the active volume, as shown in Sect. 7.3.

Finally, the tagged events form peaks in energy consistent with radon and daughters, which is the subject of the next subsection.

5.4 High energy spectra

It is desirable to have a well-resolved high-energy alpha spectrum to look for signs of surface backgrounds (see Chapt. 6), like ^{210}Po decays from under the TPB, which serves to assess to cleanliness of the acrylic sleeve.

In all versions of DEAP-1, the spectra in TotalPE are not well resolved. This is mainly due to the following two effects: The full energy alpha pulses saturate the PMTs and/or the read out electronics, and the light yield is a function of event position along the axis of the detector. In V3, an additional problem is that the two PMTs saturate at different event energies. The saturation causes the light yield to drop by about 60%, compared to the gamma calibration. This problem was partially addressed by operating the PMTs at lower gain (low voltage, or LV, data sets) to reduce the saturation at high energies, at the cost of losing sensitivity to low energy events. Since the PMTs are not sensitive to single photo-electrons when operated this way, the TotalPE variable does not indicate the actual number of singe photo-electrons in a pulse anymore. The spectra shown in this section all come from LV data sets.

The saturation of the PMTs is shown in Fig. 5.4 for V3. The high energy alpha

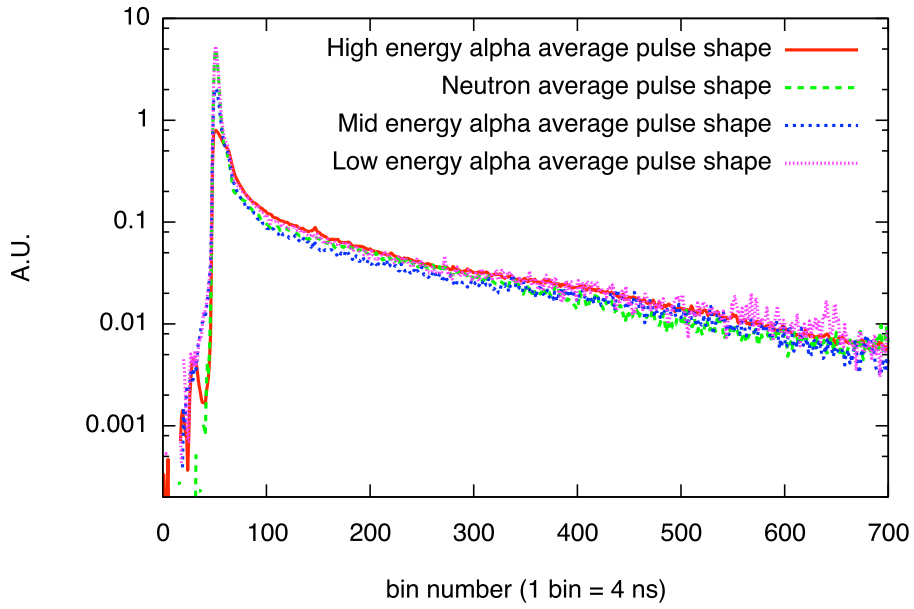

Figure 5.4: Average pulse shapes of full energy alpha pulses in V3, as well as neutrons and alpha pulses at mid and low energies. Pulse shapes are normalized to have the same intensity in the tail. The peak is more and more truncated at higher energies because of PMT saturation.

peak is clearly truncated compared to the lower energy alpha and neutron pulse shapes. Extrapolating energy calibrations done with gamma sources to high energy alphas is questionable due to this effect. The dependence of light yield on event position, or "zfit", was already known for gamma sources, but extrapolating the shape of the dependence from gamma events to alpha events is again a questionable procedure, especially for V3.

In the absence of calibration sources for high energy alpha events, the tagged events were used for calibration. The first and the second event from each tag have well known energies; the tagged events can therefore be used to get both an energy and a zfit-dependence calibration for full energy alphas. For V3, a radon spike supplied a large number of events which allowed for a good energy and zfit calibration. For V2,

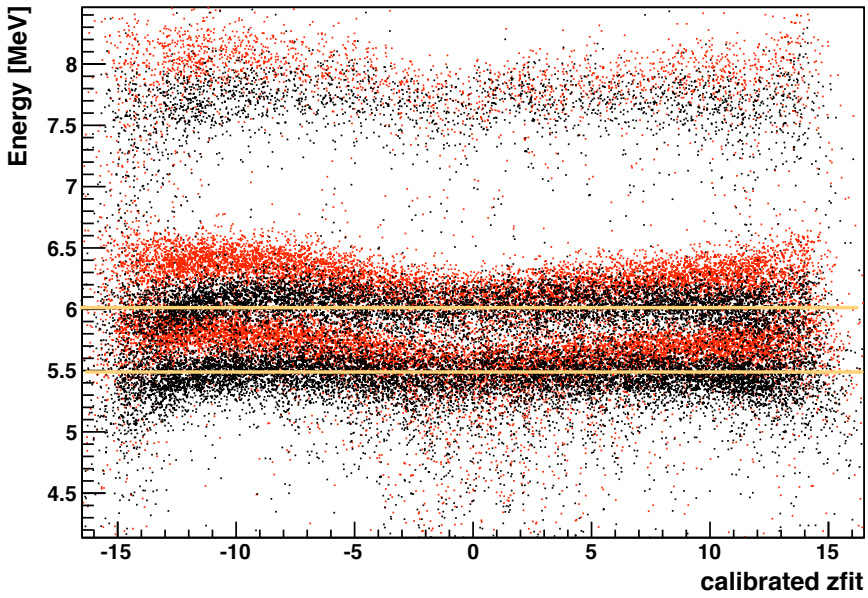

Figure 5.5: Energy versus Zfit before (red) and after (black) correction.

the zfit calibration found from gamma sources was used, but the energy calibration was done using tagged alpha events. For V5, I used the tagged events to do both the energy calibration and the zfit correction.

The zfit correction can most drastically be seen by looking at the corrected and uncorrected zfit versus charge plot, as shown in Fig. 5.5 for V3 data after the radon spike. The three peaks from ^{222}Rn and its daughters are clearly visible. The zfit variable was adjusted to shift the distributions such that they are centred on position zero. Other features will be discussed in the following section.

The peaks formed by tagged events for V3 are shown in Fig. 5.6; V2 and V5 data looks similar. The ^{222}Rn and ^{218}Po spectra seem to have a second peak each due to random coincidences.

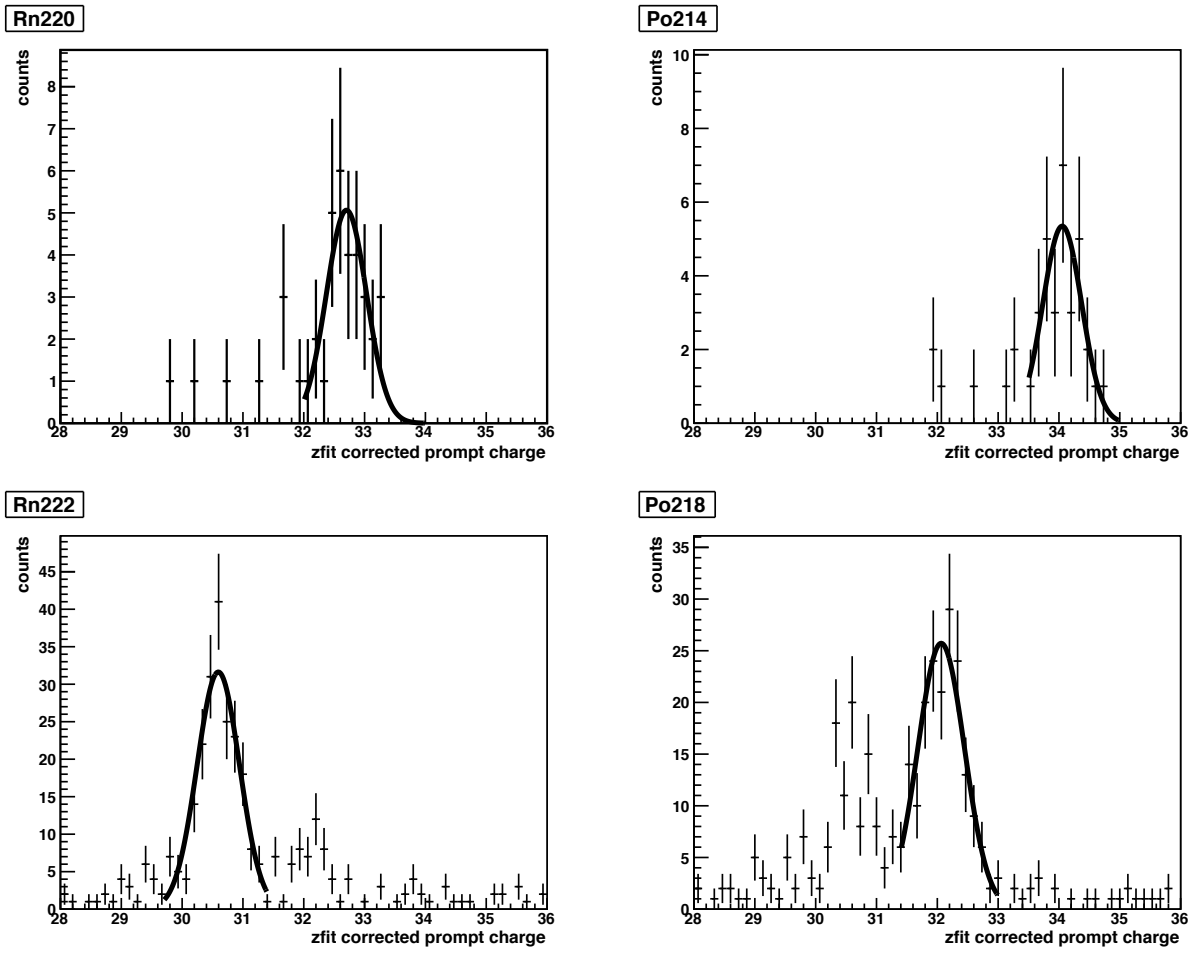

Figure 5.6: The peaks formed by tagged radon decays for DEAP-1 V3. The known energies of these peaks (see Fig. reffig:rn222 and 5.1) are used for the energy calibration of high energy alpha events.

The energy calibration used for V2 data is the following:

$$E[MeV] = 6.625 \cdot 10^{-3} \cdot \frac{TotalPE}{0.962 - 0.0013 \cdot Zfit + 0.0005 \cdot Zfit^2} \tag{5.13}$$

While TotalPE is fine to use as a variable for V2, the stronger PMT saturation in V3 pulse shapes led me to look at the charges in the prompt and the late windows separately. The resolution is better when only the charge in the prompt window is used. In addition, because the PMTs have different saturation curves, the two sides of the detector have to be treated differently. The calibration found is:

$$E[MeV] = 0.367 \cdot (x + y + 4.085 \cdot \frac{x-y}{x+y}) - 5.728 \qquad (\frac{x-y}{x+y} < -0.04) \tag{5.14}$$

$$E[MeV] = 0.367 \cdot (x + y - 3.511 \cdot \frac{x-y}{x+y} - 0.3) - 5.728 \qquad (\frac{x-y}{x+y} > -0.04) \tag{5.15}$$

where the variables in the data were abbreviated to x=PCh0 and y=PCh1 (see Sect. 4.1). In V5, TotalPE with a zfit correction leads to a good energy resolution again, but the two sides of the detector still need to be treated differently:

$$E[MeV] = -1.95 + 0.00944 \cdot (TotalPE - (-1.5 \cdot (Zfit + 5.4)^2) + 10) \quad (Zfit < 1.5) \tag{5.16}$$

$$E[MeV] = -1.95 + 0.00944 \cdot (TotalPE - (-0.5 \cdot (Zfit - 12)^2)) \qquad (Zfit > 1.5) \tag{5.17}$$

Both the alpha particle and the recoil nucleus interact in the liquid argon. The energies of the recoil nuclei are all around 100 keV which is less than 2% of the alpha energies, and the recoil energy is additionally quenched. It is therefore not taken into account here.

The fully calibrated full energy alpha spectra are shown in figures 5.7, 5.8 and 5.9. I did a fit to the spectra assuming that all events above 5.2 MeV are due to decays

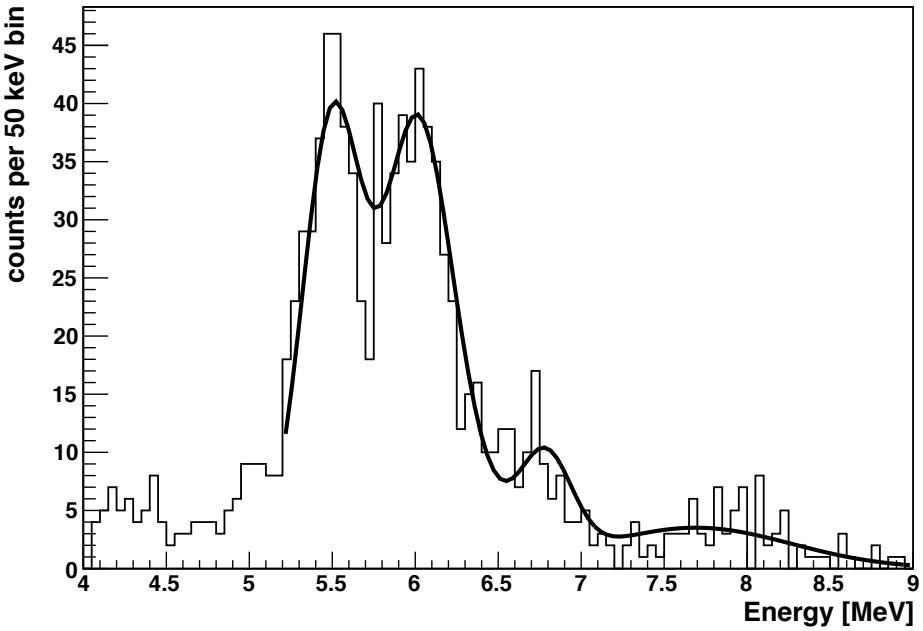

Figure 5.7: Spectrum of full energy alphas in DEAP-1 V2 (midas).

of ^{222}Rn, ^{218}Po, ^{214}Po, ^{220}Rn and ^{216}Po.[1]

The full fit function used is

$$R(E) = A \cdot n \cdot e^{-(x-5.5)^2/2\sigma^2} + A \cdot n \cdot e^{-(x-6.0)^2/2\sigma^2} + A \cdot \frac{n}{\eta} \cdot e^{-(x-7.7)^2/2\sigma'^2} + \quad (5.18)$$

$$B \cdot n \cdot e^{-(x-6.3)^2/2\sigma^2} + B \cdot n \cdot e^{-(x-6.8)^2/2\sigma^2} \quad (5.19)$$

There are 4 fit parameters: The number of ^{222}Rn and ^{220}Rn events, A and B, the resolution σ, the resolution of the highest energy peak σ' (V2 and V3 only) and the ^{214}Po scaling factor η. The variable n accounts for the binnning, it is MeV/bin for each histogram. The energies of the peaks were fixed. The number of ^{214}Po events

[1]The rate of ^{220}Rn is much lower than that of ^{222}Rn and the decays of ^{212}Bi and ^{212}Po are split, so that only very few events due to these two isotopes are expected in the data; they are therefore disregarded in the fit. The rate of ^{210}Po is strongly suppressed because of the comparatively long 22 year halflife of ^{210}Pb.

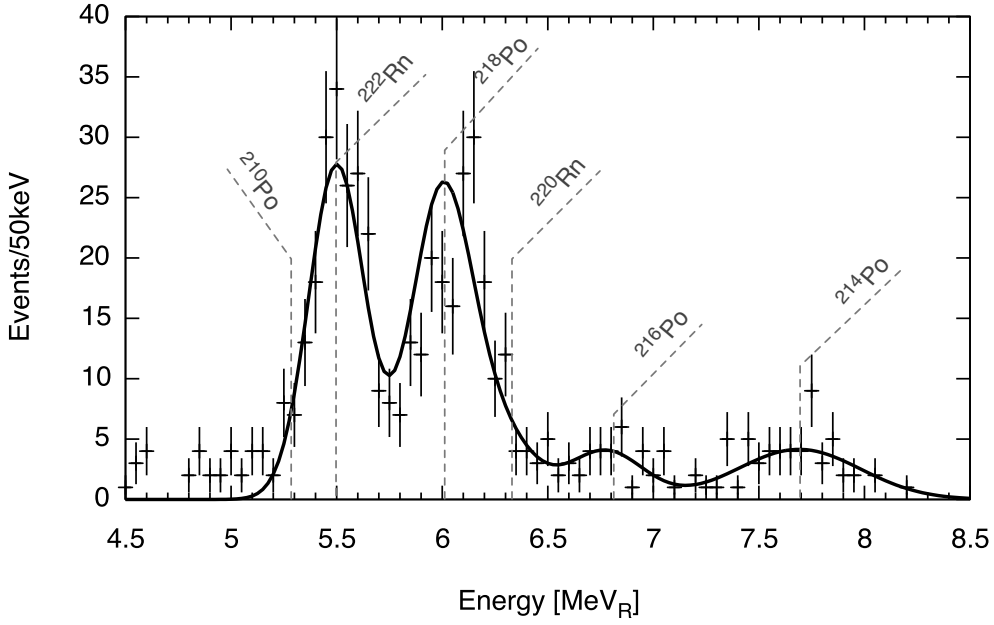

Figure 5.8: Spectrum of full energy alphas in DEAP-1 V3.

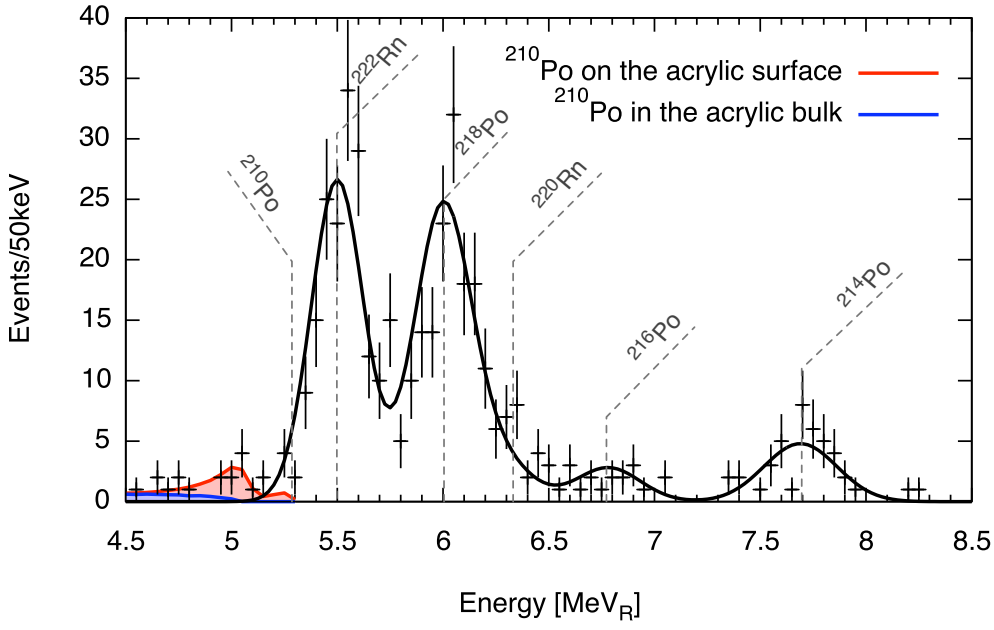

Figure 5.9: Spectrum of full energy alphas in DEAP-1 V5.

had to be reduced by a scaling factor . The missing ^{214}Po events can be found at low energies, the evidence and explanation for this is discussed in Sect. 6.3.1. The results of the fits are summarized in Tab. 5.2.

	χ^2/NDF	^{222}Rn number	^{220}Rn number	resolution (σ/E)	^{214}Po divider η
V2	1.3	350 ±15	73 ±9	0.033 ±0.002	3.4 ±0.4
V3	1.1	181 ±10	36 ±6	0.025 ±0.002	2.9 ±0.4
V5	1.0	165 ±9	21 ±4	0.023 ±0.001	4.0 ±0.7

Table 5.2: Fit results for full energy alpha spectra. For an overview of corresponding event rates, see Tab. 5.1.

5.5 Rate of unaccounted for events

The majority of the event rate in the nuclear recoil band at high energies could be identified as coming from decays of ^{222}Rn, ^{220}Rn and their daughter isotopes. To see if any other sources of alpha particles could be contributing to the high energy events in V2 and V3, the total number of tagged events was compared to the number of high energy events. Each tagged event is followed by three more alpha events down the decay chain. The polonium however is suppressed by a factor of η, as fitted out. All events accounted for by the tags are then

$$N_{tag} = (2 + 1/\eta) \cdot N_{222Rn} + (2 + 1/\eta) \cdot N_{220Rn} \tag{5.20}$$

Tab. 5.3 shows the total number of high energy events accounted for with the tagging, N_{tag}, the counted number of high energy events, N_{count}, and the difference between the two as $N_{unaccounted}$. In all cases, $N_{unaccounted}$ is consistent with zero and allows for a high energy event rate not caused by radon and daughters of no more than $3.6 \cdot 10^{-5}$ Hz at 1 σ confidence level.

	V2 midas	V3 low voltage	V3 high voltage
N_{total}	985 ±31	516 ±23	2097 ±46
N_{tag}	976 ±51	529 ±40	2078 ±87
$N_{unaccounted}$	6 ±60	-13 ±44	19 ±99

Table 5.3: Comparison between the tagged and the total number of high energy alpha events.

5.6 Discussion and summary

The events from population A in figure 4.4, which is the highest energy population in the nuclear recoil band, were studied using timing coincidence and energy spectrum analysis. The timing between these high energy events is indicative of ^{222}Rn and ^{220}Rn, the decay rate of which was determined through tagging, that is counting event pairs within the expected timing coincidence window. The rate was monitored throughout the data taking runs from DEAP-1 V2 through V5 and found to be stable at 10^{-4} Hz and 10^{-5} Hz respectively, which indicates a sustained source of ^{222}Rn and ^{220}Rn, probably from emanation out of the argon process systems.

The tagged events were used to calibrate the data not just for energy but also to correct for PMT saturation effects, leading to high energy spectra with good resolution. Comparison of Tab. 5.1 and Tab. 5.2 shows excellent agreement between the tagged and the fitted number of radon decays for both V2 and V3 and for both radon isotopes.

In V5, the tagged number of events is 20% lower than the fitted number of events, and the timing spectra are distorted. The reason for this is so far not understood, the best explanation is that there was a problem with the clock recording event times. Additionally, the tagged radon rate in V5 fluctuates by a factor of 3 between runs.

The new tighter windows and neck plug (see Sect. 3.2) were probably influencing the flow of isotopes in and out of the active volume, which could have lead to tag chains being broken.

The high energy spectrum was found to be dominated by decays from ^{222}Rn and ^{220}Rn and their daughter isotopes. Contributions to the high energy spectrum not from ^{222}Rn or ^{220}Rn could be excluded at the $3.6 \cdot 10^{-5}$ Hz level.

Chapter 6

Surface backgrounds in DEAP-1

Surface backgrounds are events from alpha particles or nuclear recoils emitted from the surface or in the first 80 μm of the acrylic vessel, or the TPB. These alphas lose some of their energy on their way out of the acrylic and/or the TPB, so that only a fraction of their original energy is available to excite the argon. Events due to surface backgrounds thus have an extended energy spectrum from zero up to the full energy of the alpha particle.

6.1 Monte Carlo simulation of surface background spectra

In order to understand the background spectra, I simulated the energy loss of alpha particles from different isotopes placed at various locations in the detector. The energy loss calculation done by the Monte Carlo simulation is based on SRIM[70] tables. SRIM outputs the energy loss at a discrete set of energies; my simulation

interpolates these values linearly for energies in between. The angle under which the alpha is emitted is random and I assume the alpha travels in a straight path along the original direction; straggling or possible reflection at interfaces is not taken into account. All surfaces are assumed to be perfectly smooth.

The thickness of the TPB layer is drawn randomly from a double gaussian distribution to describe both decays on the windows and on the sleeve. The two gaussians are centred at the mean thickness of TPB on the acrylic sleeve and on the windows respectively, and both have a width corresponding to the variation in typical TPB layer thicknesses as measured with a profile meter. The mean TPB thicknesses for each version of DEAP-1 are shown in table 3.3.

In chapter 9, it will be shown that TPB scintillates and that the pulse shape is such that many events enter the Fprompt region of interest. Scintillation of the TPB is taken into account in the simulation.

If starting in the acrylic, a maximum depth of 80 μm is used, since that is larger than the maximum distance the highest energy radon-chain alpha particle can travel in acrylic. Depending on the start location and angle, the alpha particle could lose some energy in the acrylic, the TPB and the liquid argon. The acrylic does not scintillate strongly enough to have an appreciable effect here[1]. The apparent energy of the event in DEAP-1 is calculated based on the energy loss in TPB E_{tpb} and the energy loss in the argon E_{lar}, and the light yields in TPB and argon ϵ_{tpb} and ϵ_{lar} :

$$E_{app} = \frac{1}{\epsilon_{lar}}(\epsilon_{tpb} \cdot E_{tpb} + \epsilon_{lar} \cdot E_{lar}) \tag{6.1}$$

The expression in the bracket calculates the total number of photons produced, and it is divided by the light yield in liquid argon since we interpret all event energies

[1]No scintillation signal above background was observed for uncoated acrylic windows in the experiments described in Chapt. 9.

like only liquid argon is scintillating. An event of mixed origin could in principle be discriminated to some degree from its different pulse shape, but in practice this has not worked very well. For practical reasons, I used the corresponding photo-electron yields for ϵ_{lar} and ϵ_{tpb}.

I simulated primordial thorium and uranium distributed evenly throughout the acrylic and the TPB, as well as all polonium isotopes in the bulk acrylic, on the acrylic surface and in the TPB. The geometry and some of the possible paths the alpha particle can take are shown in Fig. 6.1.

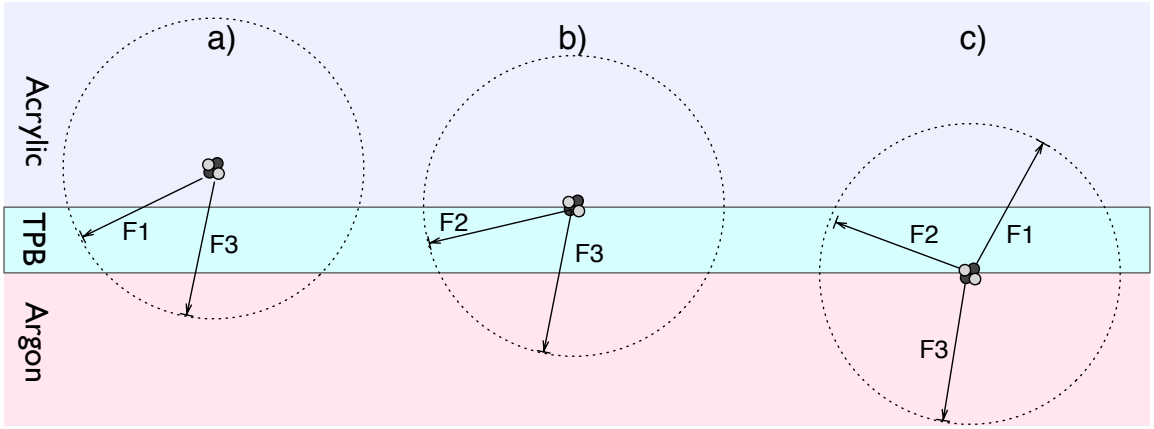

Figure 6.1: Sketch of possible paths that lead to light emission for an alpha particle emitted in the bulk acrylic (a), on the acrylic surface (b), and on the TPB inner surface (c). Labels on the paths correspond to labels in figures 6.2 and 6.3

The simulated spectra of ^{210}Po alphas from the bulk and the surface of the acrylic shown in Fig. 6.2. The spectra are not folded by the detector's energy resolution. The bulk acrylic spectrum has a feature F1, from alphas that lose some energy in the acrylic and then are stopped completely in the TPB. The remaining spectrum is nearly constant up to about 5 MeV. The surface acrylic spectrum has a sharp peak (F2)

which is also from alphas completely stopped in the TPB. The following continuum corresponds to more and more energy loss in the liquid argon. The spectrum ends at F3 just below the actual energy of the ^{210}Po alpha; the gap is the amount of energy even an alpha going straight out into the liquid argon loses in the TPB. The double peak structure is due to the difference in TPB thickness on the sleeve and the windows.

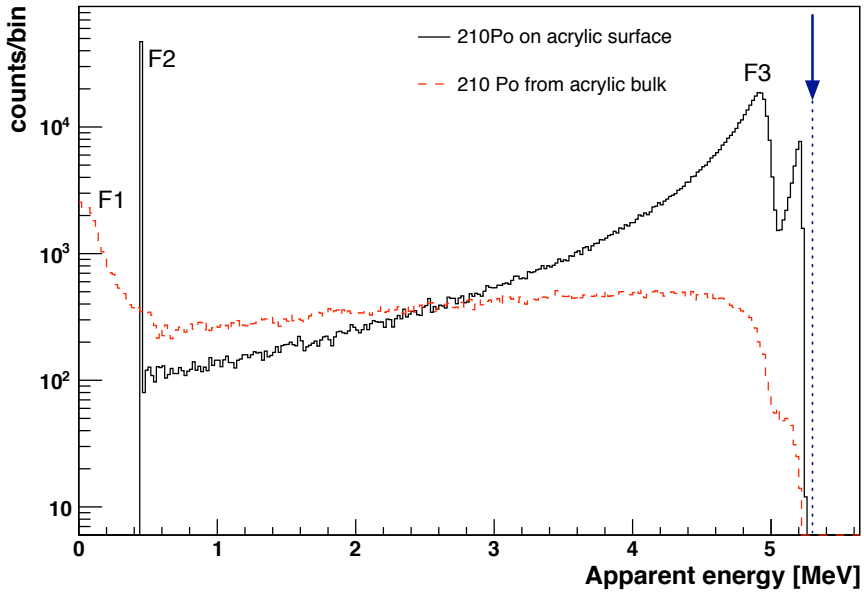

Figure 6.2: Simulated spectra of ^{210}Po alphas from the surface (solid line) and the bulk of the acrylic (dashed line). The arrow indicates the full energy of the alpha. The detector energy resolution is not included.

Fig. 6.3 shows the simulated spectrum of ^{214}Po on the TPB surface that faces the argon. Notable features are indicated on the figure. F1 is again only TPB scintillation from alpha particles travelling toward the acrylic. This feature peaks at around 50 keV, the rest of the energy is lost in the acrylic. The peak at F2 is from alphas going sideways through the TPB and loosing all of their energy there. F3 is

the peak from alphas going into the liquid argon. The relative height of features F3 and F1 depends on the surface structure of the TPB.

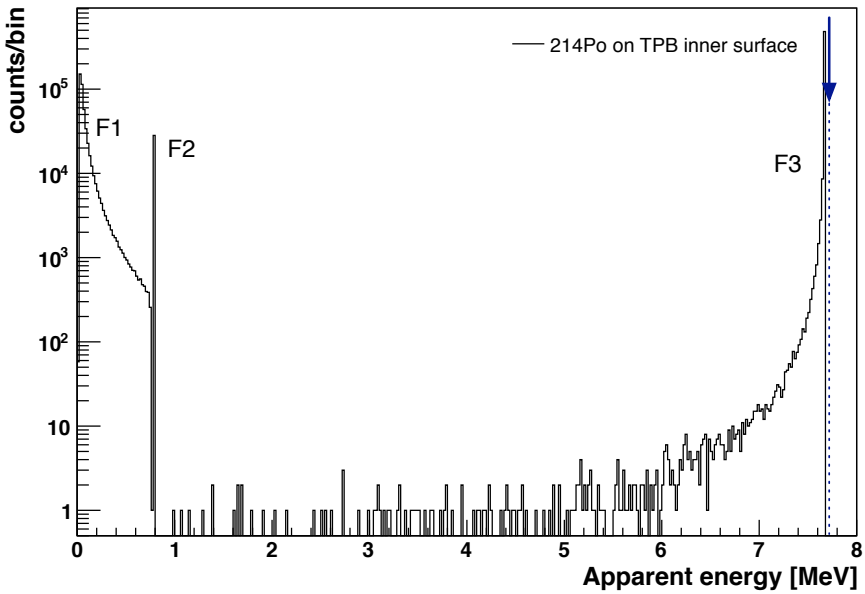

Figure 6.3: Simulated spectrum of ^{214}Po alphas on the TPB inner surface. The arrow indicates the full energy of the alpha.

6.2 Effect of a rough surface

In the ideal situation of a smooth surface, alpha particles emitted isotropically on the surface have a 50% probability of entering the bulk material and a 50% probability of entering the adjoining material. The effect of a rough surface can be understood using the model of a sinusoidal surface profile $H(x) = A \cdot \sin(k \cdot x)$ with amplitude A and wavelength $L = 2\pi/k$, as shown in Fig. 6.4. Besides entering the bulk and leaving the surface completely, there is now a possibility of leaving the surface and then entering the bulk after some distance. For a smoothly varying surface, the probability to enter

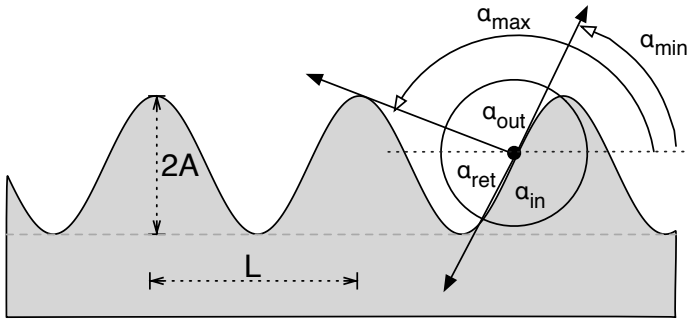

Figure 6.4: First approximation of a rough surface.

the bulk material is still 50%, but the probability to be free of the surface is lowered and depends on the amplitude and wavelength.

The probability for leaving the surface completely is given by $P_{free} =< \alpha_{out} > /2\pi$, where $< \alpha_{out} >$ is the average of that angle over the whole surface, or in the case of the sinusoidal surface profile, the average from $-L/4$ to $L/4$. Taking the horizontal as 0°, the minimum angle needed to leave the surface is determined by the surface slope at the emission location, which is just the derivative. The maximum such angle is formed by the line connecting the emission location to the maximum elevation opposite of the flank where the emission takes place, which in the range under consideration is located at $x = -\frac{3}{4}L$. Thus

$$\alpha_{min} = |\arctan(\frac{dH(x)}{dx})| \tag{6.2}$$

$$= |\arctan(Ak \cdot \cos(kx))| \tag{6.3}$$

$$\alpha_{max} = \pi - \arctan(\frac{A - H(x)}{x + \frac{3}{4}L}) \tag{6.4}$$

$$= \pi - \arctan(\frac{A(1 - \sin(kx))}{x + \frac{3}{4}L}) \tag{6.5}$$

and

$$\alpha_{out} = \alpha_{max} - \alpha_{min} \tag{6.6}$$

So that

$$P_{free} = \frac{2}{L}\frac{1}{2\pi}\int_{-L/4}^{L/4}[\pi - \arctan(\frac{A(1-sin(kx))}{x+\frac{3}{4}L}) - |\arctan(Ak\cdot cos(kx))|]dx \quad (6.7)$$

This can be numerically integrated. For example for $A = 5\,\mu m$ and $L = 10\,\mu m$, $P_{free} = 0.252$. If the average L for a surface is larger than the range of the emitted particle in the medium, P_{free} is an underestimate.

For isotopes on the acrylic surface, the above considerations mean that some alpha particles can travel a short distance through the TPB and then enter the acrylic again, leading to an event below the minimum energy found in the simulation. This is a particular concern for DEAP-3600, since these events might then be in the energy region of interest.

A surface scan of a piece of sanded acrylic similar to the DEAP-3600 acrylic is shown in Fig. 6.5[2]. The fraction of events that leave the surface and then enter the bulk material was calculated by taking each point of the scan and finding the probability of a particle emitted isotropically from there to hit the surface again. This fraction was found to be below 1%.

Similar considerations can be made for isotopes on the TPB surface, where a fraction of less than 50% of the decays will lead to a full energy event from the alpha particle losing all its energy in the liquid argon. The TPB surface is a lot rougher than the acrylic surface, as indicated by the fact that the full energy alpha spectra show only about 1/4 of the expected ^{214}Po rate. This will be further discussed in Sect. 6.3.1.

[2]Scan data provided by Slav Florian.

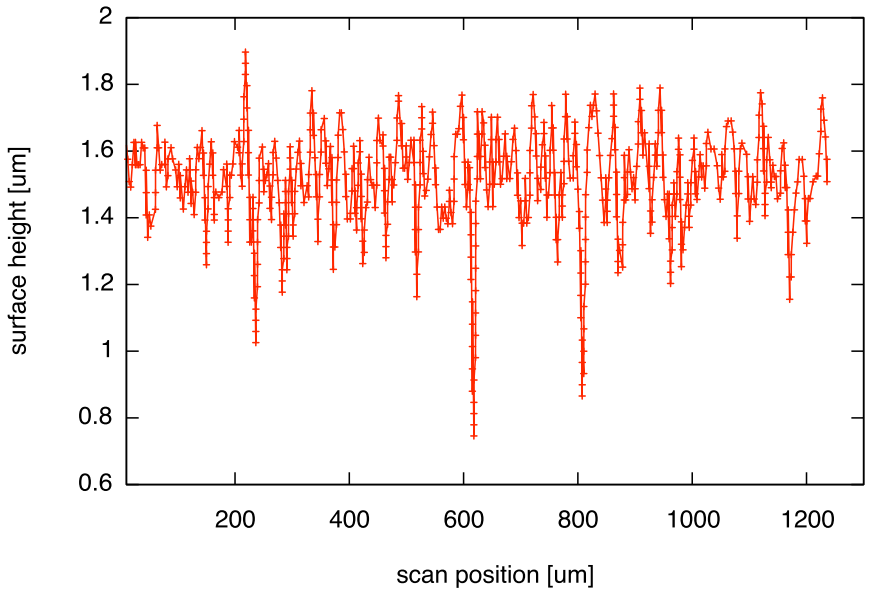

Figure 6.5: Surface profile of a piece of sanded acrylic.

6.3 Comparison of simulated and measured spectra

6.3.1 The missing ^{214}Po

The fits to the high energy spectra indicate that the ^{214}Po peak has only 1/4 of expected events. The missing ^{214}Po events might show up at low energies if the ^{214}Po adheres to the TPB surface and the alpha particle goes into the TPB. These events are made up of light from the TPB scintillation and light from the recoil nucleus in the LAr.

The rate of high energy events in V5 is $(4.4 \pm 0.3) \cdot 10^{-4}$ Hz, composed of 1 part ^{222}Rn alphas, 1 part ^{218}Po alphas and 1/4 part ^{214}Po alphas. According to the rough surface model, if 1/4 of the alpha events go into the liquid argon, making a high

energy event, then 1/2 of them go into the TPB making a low energy event, and another 1/4 travel partially through argon and partially through TPB, making an intermediate energy event.

To get the rate expected in the low energy peak then, one calculates

$$R_{214Po,LE} = \frac{R_{HE}}{2 + 1/4} \cdot \frac{1}{2} \cdot 0.37\,, \tag{6.8}$$

where the 0.37 is the efficiency of the zfit cut used on the low energy data. This leads to an expected low energy rate of $(3.6 \pm 0.2) \cdot 10^{-5}$ Hz.

The measured rate of events in the low energy peak presumed to come from ^{214}Po is $3.9 \cdot 10^{-5}$ Hz, in excellent agreement with the expectation.

The low energy spectrum including the peak from ^{214}Po on the TPB will be discussed in the context of the low energy background rate (Chapt. 8).

6.3.2 A limit on ^{210}Po from the acrylic bulk

Acrylic is made from small beads of material, which provide a large surface area for ^{210}Po from radon in the air to adhere to, or directly from liquid monomer, which is easily permeated by radon. Once made into acrylic, the bulk of the matter is expected to be enriched in ^{210}Po. For DEAP-3600, it is important to know the rate of these events.

The simulated spectrum of ^{210}Po from the acrylic bulk is shown in Fig. 6.2. No reliable energy calibration is available for the data between about 1 and 5 MeV, so fitting the spectrum to the data to obtain the ^{210}Po contamination is not possible. However, the probability for an event to present in a certain energy range per ^{210}Po decay can be calculated and used to correct the integrated rate in the same energy range of the measured spectrum, using start and stop energies in the calibrated low

energy and high energy regions.

For 1400 to 4400 PE (350 keV to 4.5 MeV), the probability is $(7.8 \pm 0.2) \cdot 10^{-2}$, where the uncertainty is due to the uncertainty in the energy calibration. The event rate in a zfit range of -10 to 2 (11.3 cm), corresponding to an acrylic volume of 4.3 cm^3, is $(8 \pm 2) \cdot 10^{-6}$ Hz. The total rate of ^{210}Po decays in that volume is then $(1 \pm 0.1) \cdot 10^{-4}$ Hz/cm^3. This leads to a limit of $(5 \pm 0.5) \cdot 10^{-19}$ g/g.

The simulated spectrum scaled to this rate is drawn together with the high energy spectrum in figure 5.9.

6.3.3 A limit on ^{210}Po from the acrylic surface

The simulated spectrum of ^{210}Po from the acrylic surface has a peak at around 5 MeV that can be used to match the simulated spectrum to the observed high energy spectrum. Care must be taken when comparing the simulated spectra to data, to accurately determine how the scintillation from the TPB is interpreted in the energy calibration of the data. The high energy alphas have a lower light yield than the low energy events, so the additional TPB scintillation is interpreted in terms of that light yield here.

The high energy spectra from all detector versions could be fit this way, but the excess of events observed around 5 MeV in V2 and V3 spectra will be shown to be dominated by geometric background events. The red line in figure 5.9 shows the fit of the simulated spectrum of ^{210}Po on the acrylic surface to the high energy spectrum from V5. The fit returned a scaling factor of $5 \cdot 10^{-5}$ on the simulated spectrum with 10^6 simulated decays. With a lifetime of 1160814 s for that data set, the total rate of these decays was $(4.6 \pm 1.1) 10^{-8}$ Hz/cm^2.

6.4 Discussion and summary

Spectra from the alpha decay of primordial isotopes and their daughter products on various detector surfaces were simulated. The simulations are basic in the sense that they simulate the energy loss in various materials of alpha particles travelling straight lines along their original trajectory, disregarding straggling or the production of sputtering products. Surfaces are assumed to be smooth, though the effect of a rough surface was studied analytically. This simple approach was sufficient to identify significant inconsistencies in the original surface background hypothesis for detector V2 and V3, and then to describe much of the data taken with V5.

The simulated spectra indicate that isotopes on the surface of the acrylic or the TPB cannot cause events below a minimum energy given by the scintillation from the alpha particle passing the thickness of the TPB. This however is only a first order approximation.

Fitting these simulated spectra to the V5 background data allowed me to obtain competitive limits on the contamination of the acrylic chamber's bulk ($(5 \pm 0.5) \cdot 10^{-19}$ g/g) and surface ($(4.6 \pm 1.1)10^{-8}$ Hz/cm^2) with ^{210}Po, as well as explain part of the low energy spectrum, which will be discussed in chapter 8.

The ^{210}Po limits obtained are upper limits in the sense that all events in a given energy range were assumed to be due to this source. For ^{210}Po in the acrylic bulk, remaining geometric events from the windows and neck (see Chapt. 7) could have leaked into the cut region used to obtain the limit, and some ^{214}Po events are known to occur in the same region.

For ^{210}Po on the surface, the small excess of events around 5 MeV that the fit is based on could also all be due to geometric events, though their zfit distribution is

more consistent with the surface background model.

Most of the event rate from surface backgrounds would appear at the windows, since they have the most surface area per bin along the axis of the detector. Indeed, population B in the background data from DEAP-1 versions 2 and 3 has just those properties (compare Fig. 4.3). This observation, and the absence of any other explanation at that time, led to the hypothesis that event population B was indeed due to surface backgrounds.

The simulated spectra however do not match this data. The simulated spectra all have some rate in the high energy region discussed in the previous chapter, where the rate not from ^{222}Rn, ^{220}Rn and their daughters was found to be less than $3.6 \cdot 10^{-5}$ Hz. According to the simulation results, in order to explain the low energy rate in V2 and V3, a rate far exceeding this would have been observed above 5 MeV, making the original hypothesis that they are due to surface backgrounds seem unlikely. In addition, the more careful treatment of the surfaces of the V3 detector chamber resulted in only minor improvement to the background rates (see Chapt. 8), and the small excess of events in the high energy spectra around 5 MeV (presumed to be from ^{210}Po on the acrylic surface[48]) in the high energy alpha spectrum also remained.

These inconsistencies prompted much of the detailed analysis of radon spectra and background event distributions, which eventually led to the discoveries outlined in chapter 7, and the subsequent improvement of the detector for V5.

Chapter 7

Geometric backgrounds

While the DEAP-1 data from V2 and V3 did not match any of the simulated surface background spectra, it did have striking similarities with Monte Carlo simulations of radon decays in the liquid argon, done by M. Kuzniak. There, too, a population of events appeared which were clustered near the window and centre of the detector and had an extended energy spectrum. These events came from decays in gaps, areas of the detector from where not all light could reach the active volume, so they appeared to have some amount of energy from zero to full energy, depending on the location of the decay. We call these alphas appearing at lower than full energy "gap alphas", and the class of backgrounds "geometric backgrounds".

Since taking more physics data in V3 was not deemed useful due to the high background level, the theory of geometric low energy backgrounds was instead tested by purposefully injecting ^{222}Rn gas into the detector. This will be referred to as "the spike".

Fig. 7.1 shows the rates of ^{222}Rn, ^{218}Po and ^{214}Po versus the time since the spike. The rate initially increased by a factor of about 900. As before, the ^{214}Po peak is

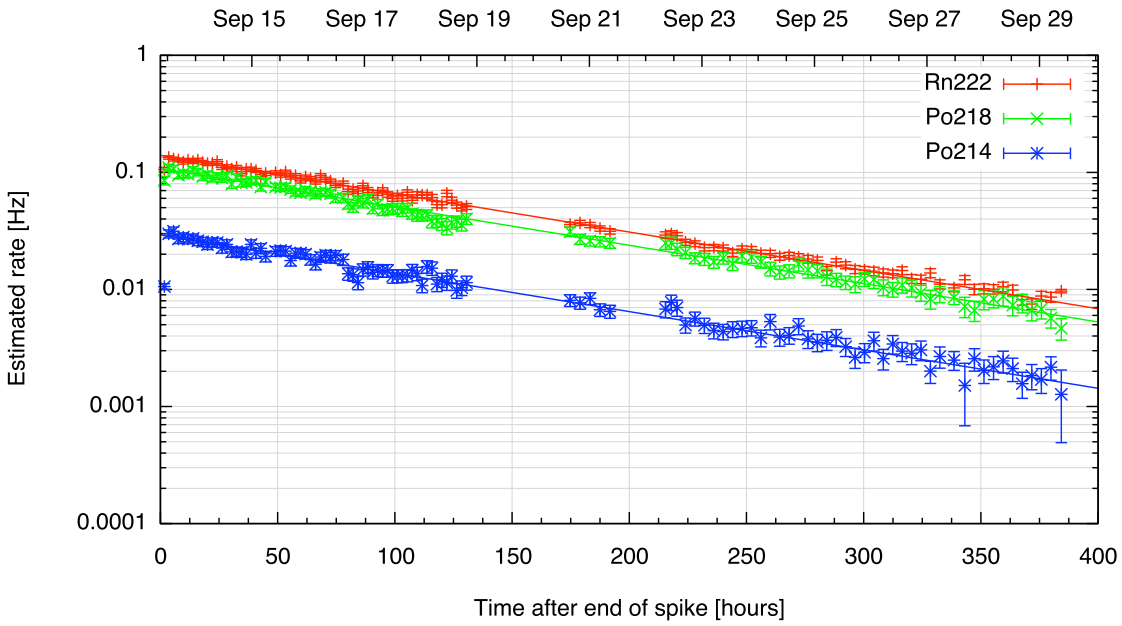

Figure 7.1: Fitted number of events in each radon daughter peak after the spike.

suppressed in comparison to the ^{222}Rn peak, and with the higher statistics here one can see that the ^{218}Po is also slightly suppressed.

7.1 Full energy radon spectra after the spike

The radon spectra measured two and nine days after the spike are shown in Fig. 7.2. Each peak has an excess of events towards lower energies. This is the excess that was previously believed to be evidence of ^{210}Po decaying on the acrylic vessel behind the TPB[48].

If this hypothesis had been correct, there would be no such excess in the spectrum recorded after the spike. The spike data provides a template spectrum of ^{222}Rn that can be fit to the normal run data and subtracted, as shown in Fig. 7.3. The difference spectrum shows the two peaks corresponding to the ^{220}Rn alphas, and no excess of

events at 5 to 5.5 MeV. This excess is thus a feature of the ^{222}Rn spectrum as observed in DEAP-1 and not related to ^{210}Po from below the TPB. The slight offset between the spectra is due to energy calibration drift over time.

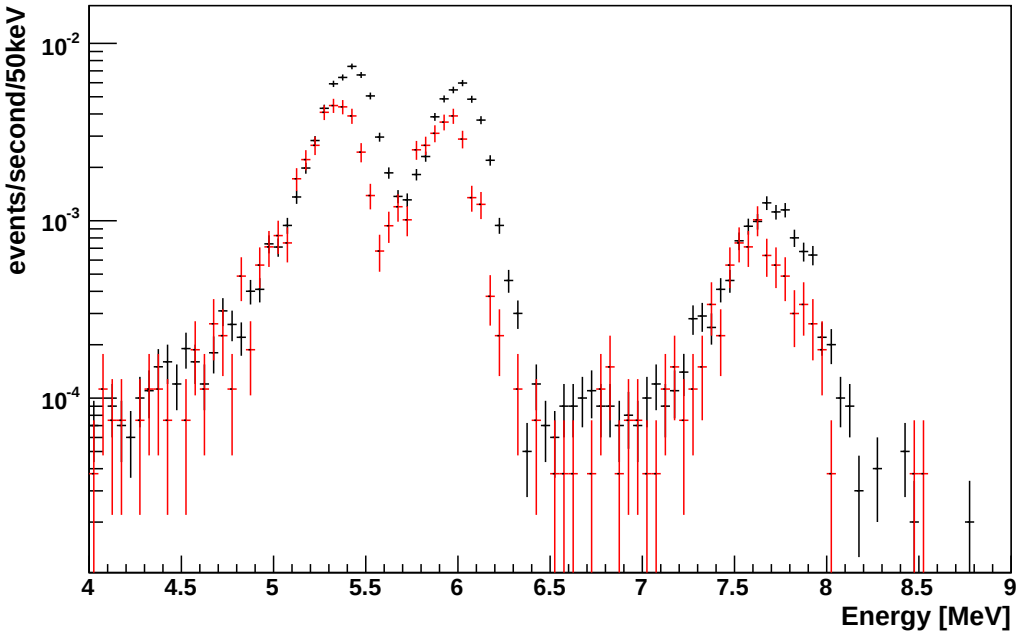

Figure 7.2: Alpha spectra 2 days and 9 days after the spike

7.2 Correlation in rate between full energy and low energy events

Shown in Fig. 7.4 is Zfit versus energy at high and low energies after the radon spike. In the first plot, energies are Zfit corrected and Zfit is converted to cm. The second plot shows the raw Zfit variable against approximate energy, corrected for the alpha quenching factor. In the high energy plot, a leakage of events down to lower energies

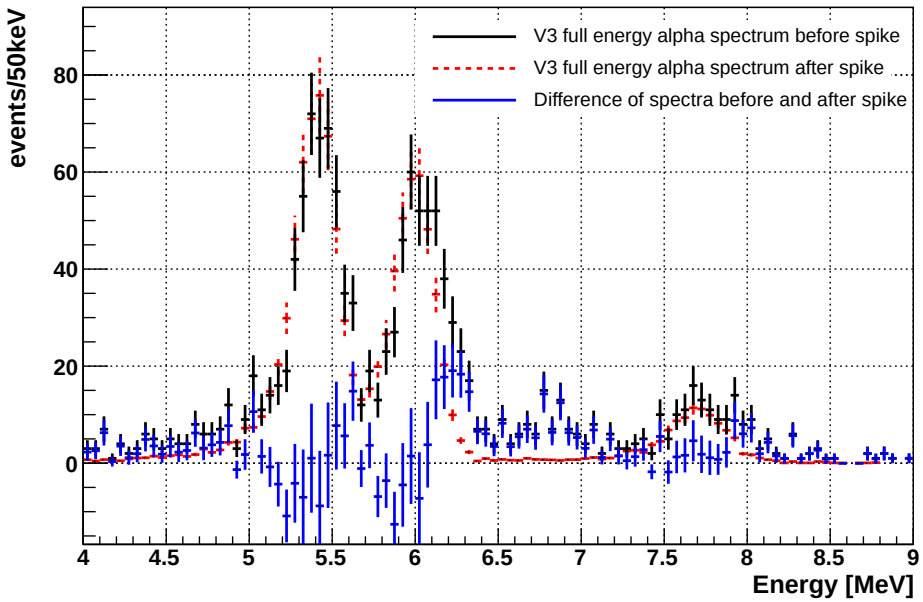

Figure 7.3: The alpha spectrum in V3 before the spike, fit with the spectrum after the spike.

is visible at the center and the windows of the detector. This leakage reaches all the way down to zero energy and is the cause for the low-energy tails of the peaks shown in Fig. 7.2.

The events below 50 keV and far out Zfit are from population D in figure 4.4. Their rate did not increase after the radon spike.

The rate of events leaking down from the full energy alpha bands at the sides and the center of the detector increased after the spike. The factor by which it increased is not the same for all energy windows. Fig. 7.5 shows the tagged number of ^{222}Rn decays versus time, as well as the rate in two low energy windows of interest, 120-240 PE and 240-480 PE. The background in these low energy windows decreases at the same rate as the ^{222}Rn.

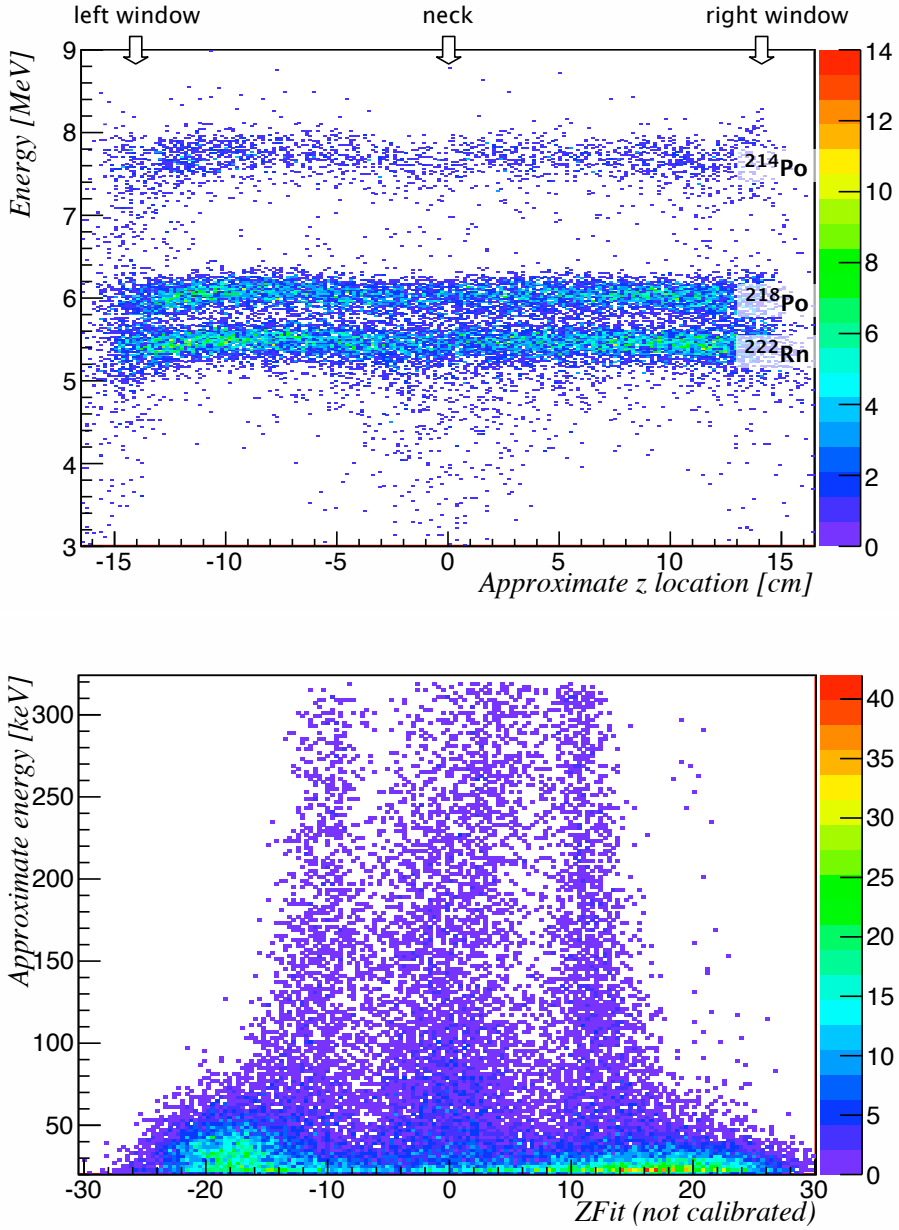

Figure 7.4: Zfit versus energy at high (top) and low (bottom) energies after the radon spike. The coloration indicates the number of events per bin. In the high energy plot, a leakage of events down to lower energies is visible at the center and the windows of the detector. This leakage reaches all the way down to the detector energy threshold. Below 50 keV, another population of events at further out zfit emerges, the hot spot events.

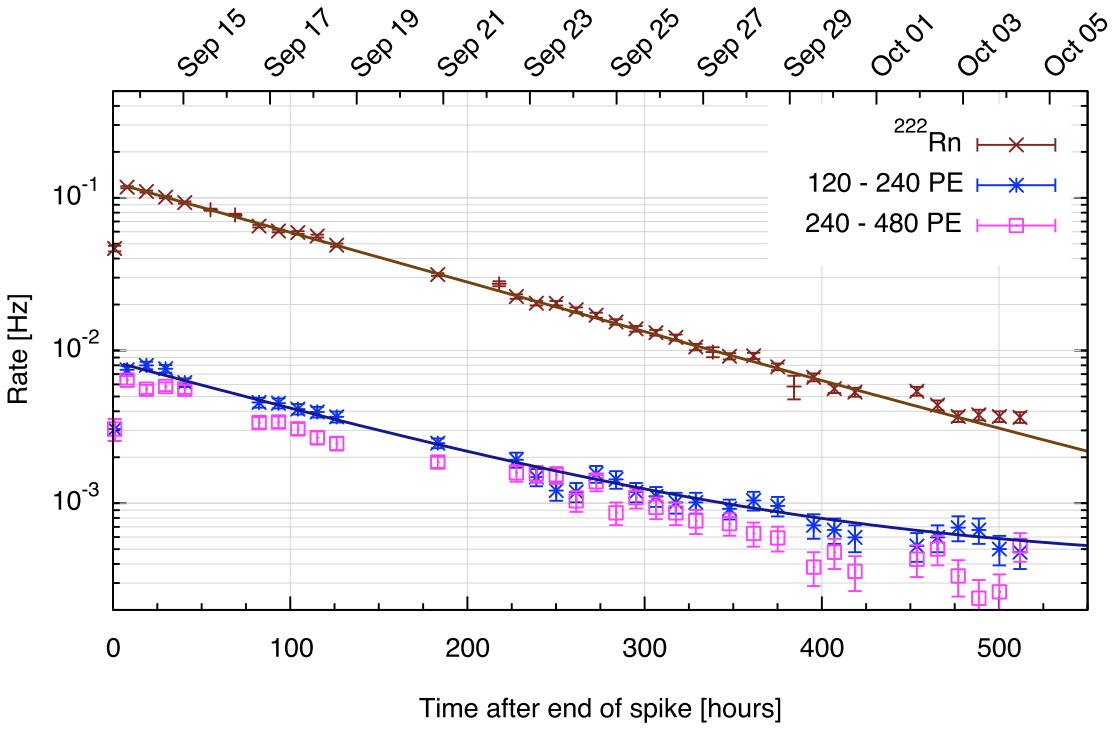

Figure 7.5: Full energy radon rate and event rate in two low energy windows versus time after the radon spike. Theoretical decay curves are also drawn. The low energy rate decreases similarly to the full energy rate, indicating that these low energy events are in fact caused by radon decays.

At the beginning of the spike, the low energy rate starts increasing at the same time, possibly even before the high energy rate does, though the statistics is too low to say for sure. A faster rise is expected if the radon takes some time to reach the active liquid argon volume and until it is there, only low energy events from what are at that point gap alphas in the neck of the detector can be seen.

7.3 Correlation in timing between full energy and low energy events

Alpha emitting isotopes can drift in and out of areas with low light collection efficiency. We thus expect there to be real timing coincidences between high and low energy events and between low and low energy events, in addition to the high-high energy event correlations discussed in Sect. 5.1, though the time constants may be altered. A low energy event from, for example, ^{222}Rn in the neck may be followed by a high energy event, another low energy event, or no event at all, depending on whether the ^{218}Po drifted into the active volume, stayed in the neck, or drifted up the neck so high that the visible energy of the decay is below the experiment's energy threshold.

I define the high energy region as TotalPE $>$ 3500 and the low energy region as 200 $<$ TotalPE $<$ 3500, and consider only events with -8$<$Zfit$<$3. I then tag events less than 1000 s apart in time, requiring the order of events to be a) high energy $\rightarrow$ low energy, b) low energy $\rightarrow$ high energy, c) low energy $\rightarrow$ low energy. The longer tag time window was chosen to accommodate the altered time constants. The results are shown in Tab. 7.1. In each situation, the tagged number of events is two to four times higher than the expected number of random coincidences.

The timing spectrum between events where both partners are in the low energy window is shown in Fig. 7.6. A double exponential fit to this spectrum returns a half-life of 55$\pm$18 s for the faster component, consistent with the half-life of ^{220}Rn. This indicates that ^{224}Ra is present in the neck. After the ^{224}Ra decays, the ^{220}Rn does not have much time to drift out of the neck or to a region with much worse

order of energies	total number of such pairs	tagged	expected if random
high → low	445	192	55
low → high	445	217	55
low → low	783	370	167

Table 7.1: Timing correlations between high and low energy background events in DEAP-1 V3.

light collection efficiency, thus nearly every low energy event from ^{224}Ra is followed by another low energy event from ^{220}Rn, and the timing is not distorted. Should ^{224}Ra be inside of the active volume, its contribution to the energy spectrum would seem like a statistical fluctuation in between the ^{222}Rn and ^{218}Po peaks. The lack of tags between high energy events however indicates that no ^{224}Ra is in the active volume.

Based on the constant and half-life from the fit (Fig. 7.6), 20 ^{224}Ra coincidences are expected to occur with a timing of less than 100 s. Many of the events tagged with less than 100 s timing are not ^{224}Ra coincidences, due to the second component in the timing spectrum. A real ^{224}Ra event is followed by ^{220}Rn, which in turn is followed by ^{216}Po in less than 0.5 s. Out of all double coincidences with a timing of less than 100 s, 8 are followed by another event in less than 0.5 s. This is a little less than half of what was expected, however, there are two possibilities for the ^{216}Po to not be visible: it could drift to an area from where no light can reach the PMTs or it could adhere to a wall and emit the alpha into the wall.

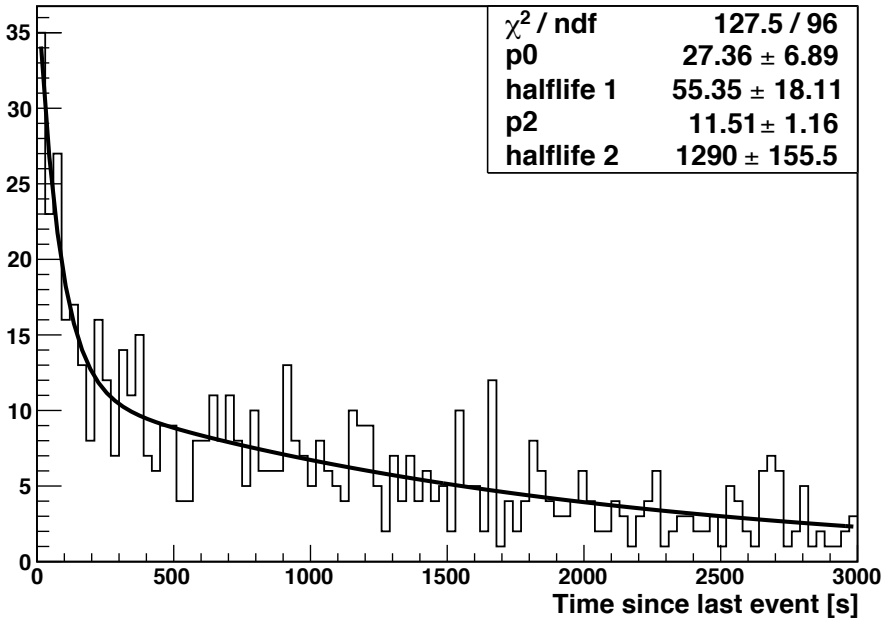

Figure 7.6: Timing spectrum between pairs of low energy events. The thick line is a double exponential fit to the spectrum, fit parameters are shown in the box. Data is from V3.

7.4 Extrapolation of background rate in the absence of gap alphas

Using the radon spike data, I was able to estimate the expected background in the energy region of interest without gap alphas. Fig. 7.7 shows the Zfit distribution of events in the 120-240 PE region of interest. The distribution before the spike is dominated by the hot spots (at zfit of -21 and 16) and has some neck gap alphas events (at zfit of -5). After the spike, the window gap events at zfit of -14 and 12 increase in rate and dominate over the hot spot events. The center peak increases by a factor of 42.

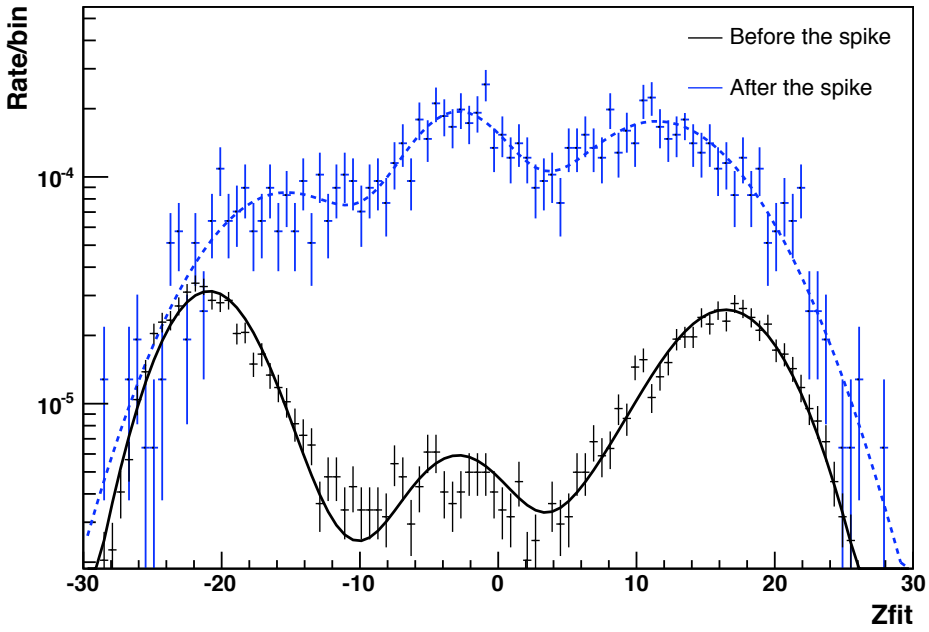

Figure 7.7: V3, Zfit distribution in the ROI before and after the spike. After the spike, the rate in the center increased by a factor of 42.

The shape of the distribution after the spike can be used as a template to the zfit distribution of gap alphas. Fig. 7.8 shows a fit of the ROI distribution before the spike, using the scaled distribution after the spike, plus two gaussians for the hot spot events, and a constant offset. Assuming the hot spot events are unaffected by the spike because they are from outside the detector, and that we can get rid of the window gap and center events by closing the gaps in a new chamber, we should have a background rate at 96% recoil acceptance of less than 40 μHz between -10 $<$ zfit $<$ 4, several times less than in V3.

The prospect of a very low background region motivated the modification of V3 to include tighter fitting windows and a plug at the top of the neck to reduce the gap alpha event rate.

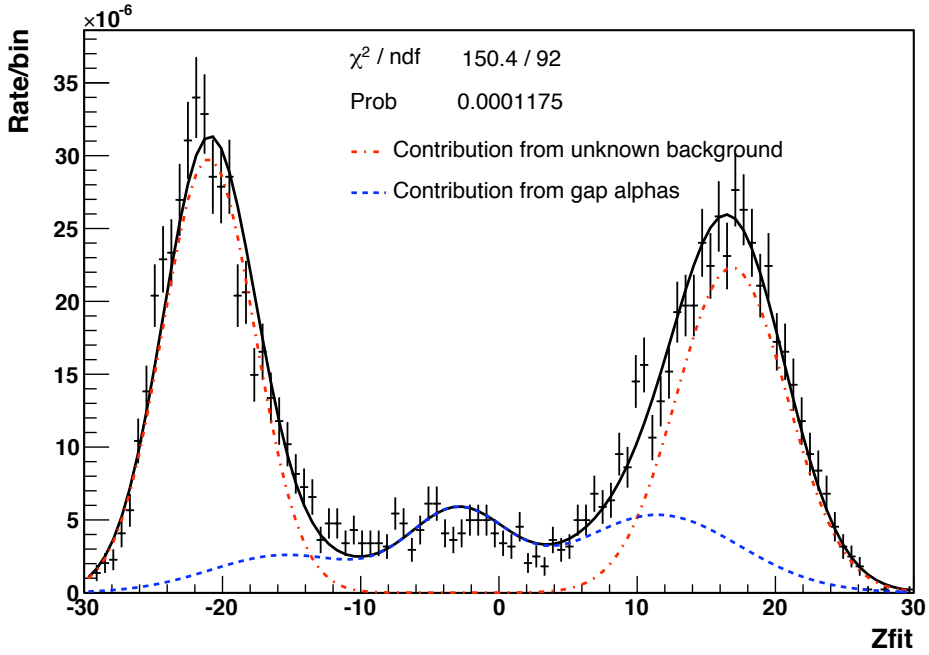

Figure 7.8: V3, Zfit distribution of ROI events, fitted with the distribution after the spike (blue dashed line) and two extra Gaussians (red dash-dot line). The distribution after the spike is dominated by gap alphas and thus serves as a model for their effect. The events described by the red line are an unknown background from outside the detector chamber.

7.5 Results of the gap alpha reduction measures in DEAP V5

In V3, there was a population of events in the centre of the detector at a mean Fprompt of 0.69, attributed to gap alphas from the neck. As Fig. 7.9 shows, these events are replaced in V5 by a population of events evenly distributed along the detector axis, at a mean Fprompt of 0.79.

The zfit distribution for events between 35 to 70 keVee is shown again in Fig. 7.10, and the energy spectrum of events in the central detector region for V2, V3 and V5

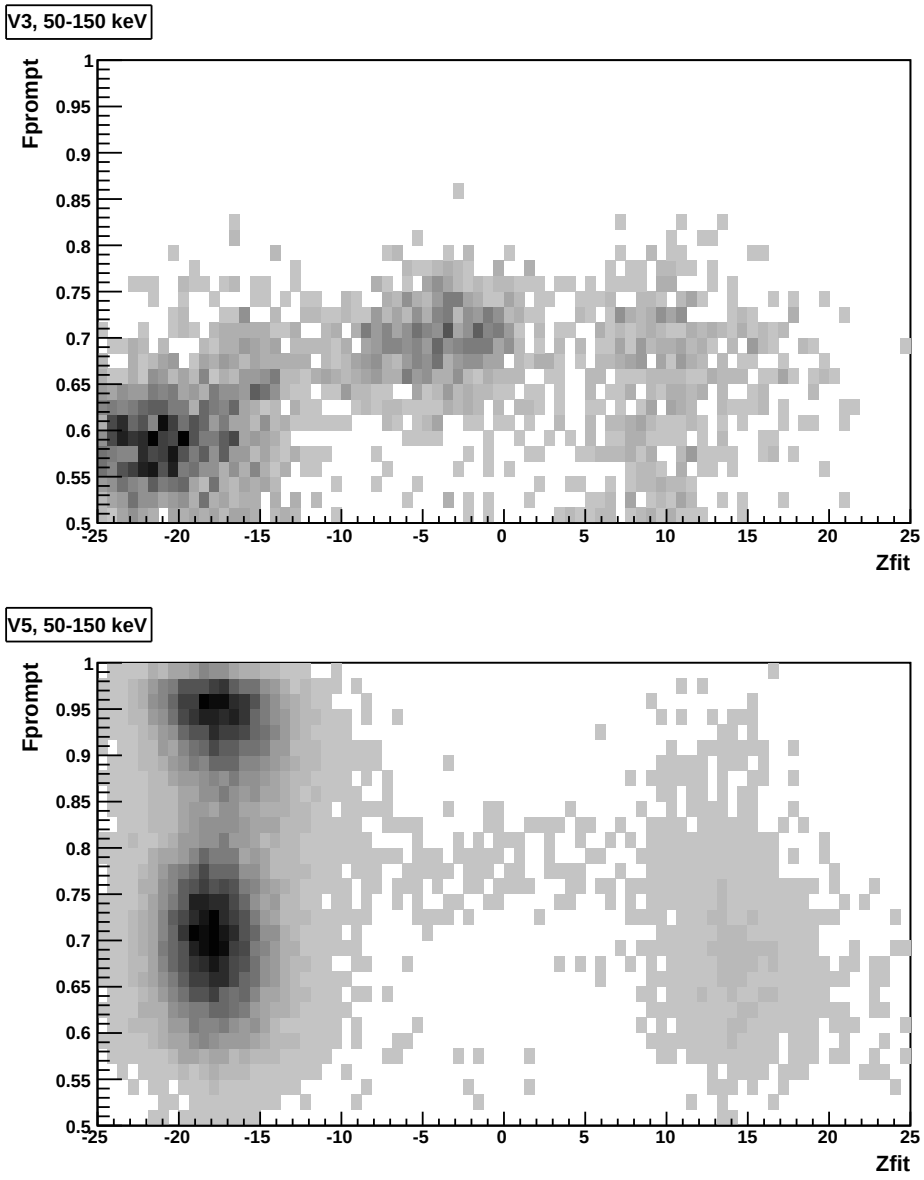

Figure 7.9: Zfit vs. Fprompt for events between 50 and 150 keVee, V3 and V5.

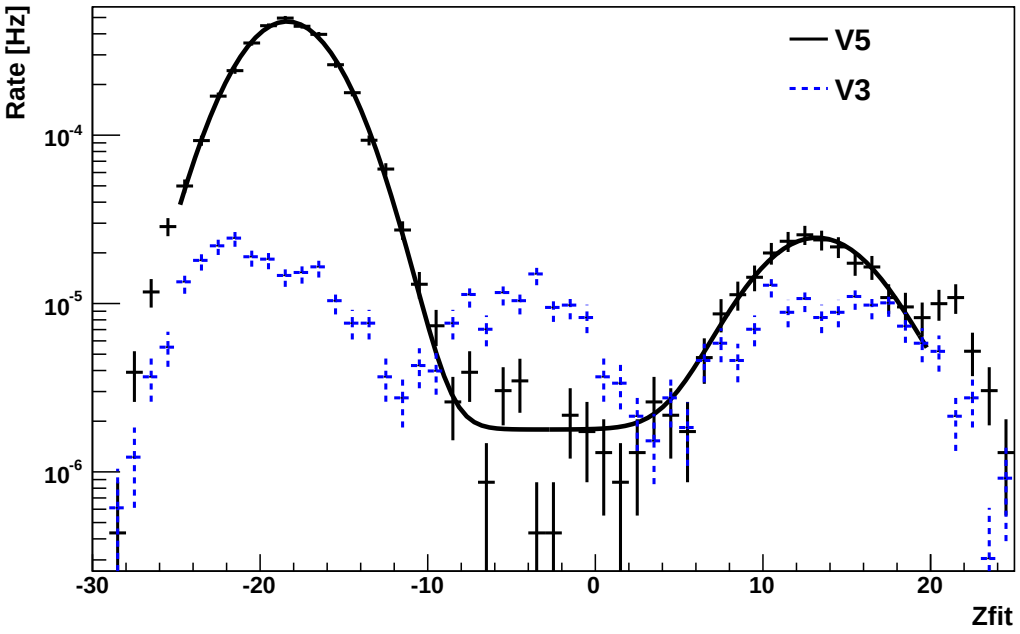

Figure 7.10: Comparison of the Zfit distribution of events in the 35 to 70 keVee energy region at 80% recoil efficiency, V3 and V5.

is shown in Fig. 7.11

The V3 and V5 spectra have a peak at around 70 keVee and around 85 keVee respectively. These peaks have been shown to be from ^{214}Po adhering to the TPB surface (see Sect. 6.3.1). The peaks are at different energies because of the difference in TPB thickness. The V2 and V3 spectra shows a continuum of events going to higher energies, which is suppressed in V5 as a result of the modification to the detector neck.

Fig. 7.9 also shows that the the hot spots on each side of the detector remain in the V5 background data. An additional population of events apparently outside the detector emerges at an Fprompt of 0.95. The rate of these events fluctuates strongly, and the fluctuations are related to the thermodynamics of the detector, as seen in

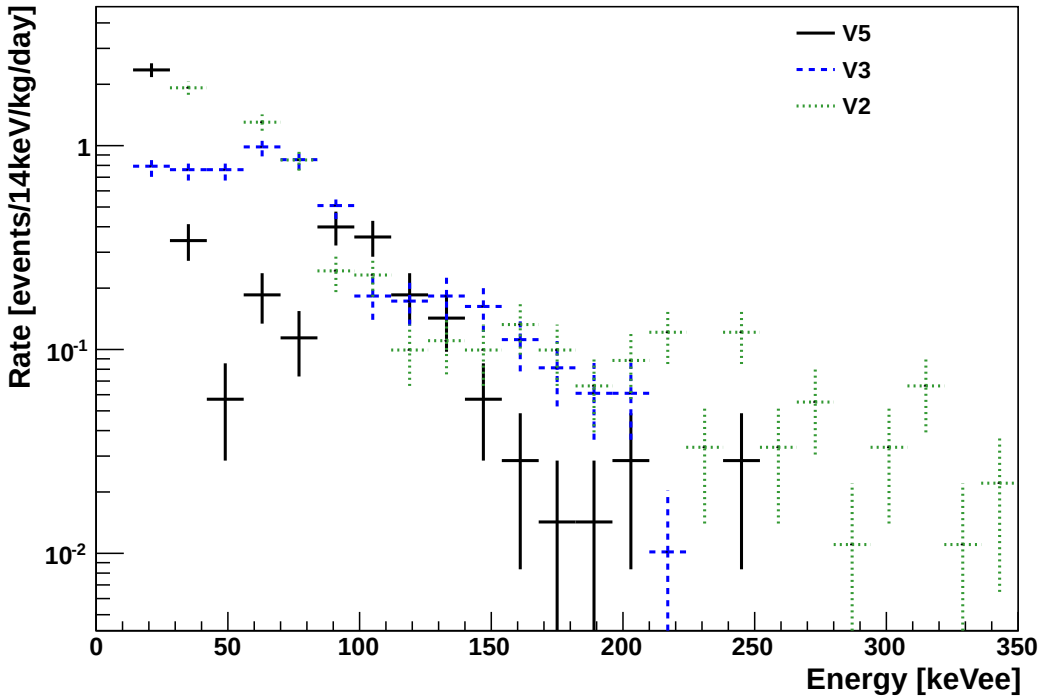

Figure 7.11: Spectra of the high Fprompt events (80% recoil efficiency) in the center region of the detectors V2, V3 and V5.

Fig. 7.12. There is a clear correlation between spikes in the argon pressure and spikes in the rate of hot spot events. The argon pressure rises every time liquid nitrogen is topped up. Those very high Fprompt events might be from cavitation in the liquid argon. The runs with an unusually high rate of these events were excluded from analysis.

7.6 Discussion and summary

A new hypothesis as to the origin of the background rate in V2 and V3, called geometric backgrounds, was developed and tested by spiking the V3 detector with ^{222}Rn. The

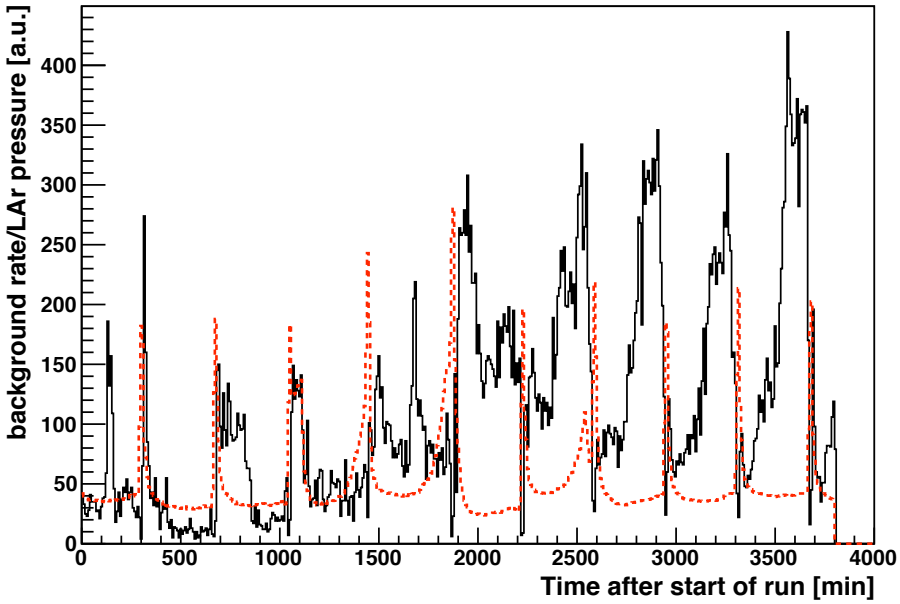

Figure 7.12: Fluctuation of the background rate (solid black) and liquid argon pressure (dashed red).

matching increase and subsequent rate of decrease between low energy background and radon rates, and the location of the background events after the spike, corroborated the idea that the gap towards the neck and the gap between the acrylic windows and sleeve (compare Fig. 3.2) allowed for degraded energy radon alpha events. Timing coincidences in excess of what was expected for random coincidences were also found between high and low energy events. In particular, the timing spectrum among low energy events is consistent with the decay of ^{224}Ra in the neck of the detector.

The gap alphas were found to cause an excess of events at the low energy tail of each peak in the high energy alpha spectrum.

The reduction in background with the modification of the acrylic chamber to include a plug in the neck and tighter fitting windows was final proof of the hypothesis,

but led to erratic background rates linked to frequent changes in the thermodynamic properties of the detector, possibly from movement of the new windows and from impedance of the argon flow through the stainless steel vessel containing the chamber, leading to sonoluminescence. In all detector versions up to and including V3, geometric background dominated the total background rate in the region of interest.

Chapter 8

DEAP-1 low energy background

8.1 Background spectrum

The low energy spectrum of the lowest background detector, V5, is shown in Fig. 8.1 and 8.2. The events in that spectrum are due to three main sources: PSD leakage, window leakage and ^{214}Po on the TPB surface.

The PSD leakage rate was found from tagged ^{22}Na PSD runs under the assumption that the ratio between the number of events in the gamma band and the number of leakage events is the same for ^{22}Na runs and for background runs. For each bin in energy, the number of events above the fprompt fraction used to make the background spectrum, $N_{Na,fp>0.72}$, was divided by the number of events in the electron recoil band ($N_{Na,fp<0.5}$) to get the leakage probability P_{leak}. This was then multiplied by the number of events in the gamma band of the background data, $N_{bg,fp<0.5}$ to get the actual expected number of leakage events for each energy bin.

$$N_{leak} = \frac{N_{Na,fp>0.72}}{N_{Na,fp<0.5}} \cdot N_{bg,fp<0.5} \tag{8.1}$$

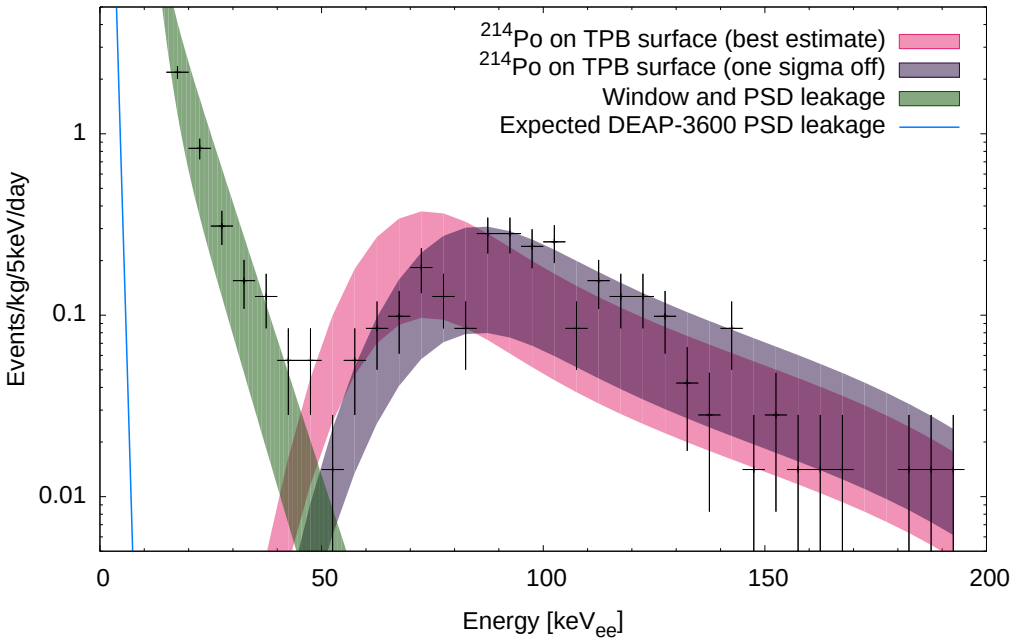

Figure 8.1: Low energy background spectrum, 85±5% recoil efficiency.

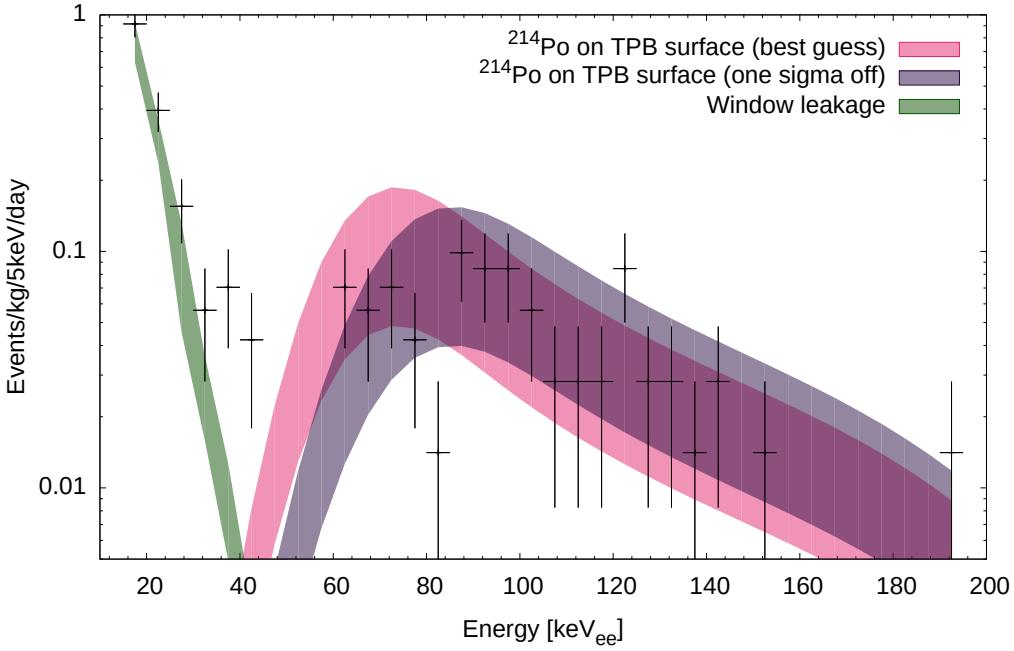

Figure 8.2: Low energy background spectrum, 50±5% recoil efficiency.

The data for this is shown in Fig. 8.3, together with an exponential fit and the uncertainties on the fit. There are not enough events in the PSD runs to track the leakage to higher energies than shown, necessitating the description through a fitted line.

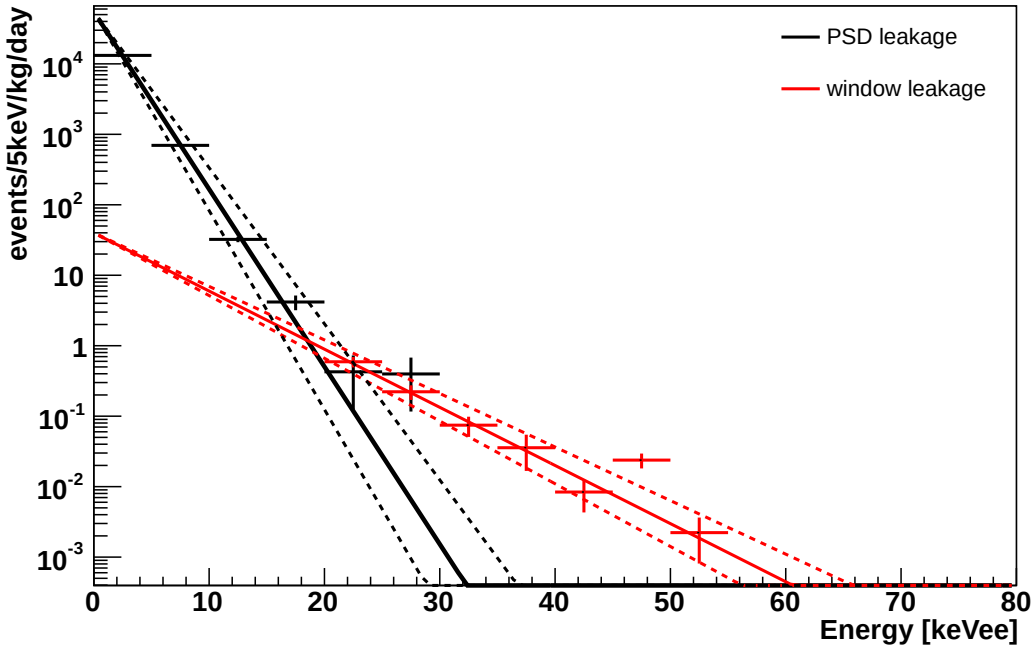

Figure 8.3: PSD and window leakage.

At around 25 keVee, the background is dominated by leakage from the unidentified events near the windows. This component was found by fitting the sum of two gaussians and a constant to the zfit distribution in the given energy bin, and then integrating only the sum of the gaussians over the zfit range of the data cut (compare Fig. 7.10). The uncertainty shown is due to the fitted out uncertainty of the parameters of the gaussians. Again, the leakage in each energy bin was fitted with an exponential function similar to the PSD leakage.

The functions describing the PSD and window leakage were added and the uncertainties were added in quadrature, to produce the green band in Fig. 8.1.

Starting at around 60 keVee, the background is dominated by TPB and LAr scintillation from ^{214}Po decaying on the TPB surface. The spectrum of this was simulated (see Sect. 6). The simulation outputs the energy lost by the alpha in TPB, E_{TPB}, for a given TPB thickness. The visible energy E_{app} is then calculated similar to equation 6.1, where not the alpha particle but the recoil nucleus loses energy in the liquid argon:

$$E_{app} = \frac{E_{tpb}\epsilon_{tpb}}{\epsilon_{lar}} + q \cdot E_{r,lar} \tag{8.2}$$

with q the quenching factor for nuclear recoils. All parameters have uncertainties associated with them. The parameters and errors are quoted in Tab. 8.1. The light

parameter	value	uncertainty
ϵ_{tpb}	200 PE/MeV	50 PE/MeV
ϵ_{lar}	2400 PE/MeV	240 PE/MeV
q	0.25	0.03

Table 8.1: Parameter values used to calculate the TPB scintillation spectrum of ^{214}Po.

yield in TPB and liquid argon is taken for DEAP V2, since the same PMTs were used in DEAP V2 and to do the measurement of the TPB scintillation. This assumes that optical effects on the light yield due to the difference in the DEAP-1 geometry and the geometry of the setup used to measure the TPB scintillation are negligible. The increase in light yield in the subsequent DEAP version was attributed to the larger light guides and more efficient PMTs, thus the same factor applies to liquid argon and TPB scintillation, leaving the apparent energy of the TPB scintillation event the same.

The energy of the recoil nucleus is about $E_{r,lar} = \frac{m_{alpha}}{m_{nucleus}} \cdot E_{alpha} = 149$ keV.

The TPB thickness has only a small effect on the spectrum between the 4 and 5 μm of its range. A value of 4.5 μm was used in the simulation.

The simulated spectrum has a peak that is a bit lower in energy than the peak in the data when using best estimated values for all parameters. The purple band shown is $E_{app} + \Delta E_{app}$, with the uncertainty calculated by standard error propagation. This increase by one sigma yields a good match to the data.

The normalization of the TPB scintillation spectrum was found based on the rate of full energy alpha events (see Sect. 6.3.1), and multiplied by the efficiency of the zfit cut used for the low energy spectrum shown here (37%). The uncertainty on the normalization is dominated by the uncertainty on the number of high energy events but also includes the uncertainty on the zfit cut efficiency and the uncertainty of the ^{214}Po reduction factor.

The simulated event rate due to ^{210}Po from the acrylic bulk, normalized to give the right number of events at intermediate energies (see Sect. 6.3.2) lies two orders of magnitude below the limit of the plot and does not contribute significantly to the observed event rate.

In principle, ^{210}Po decays from the surface of the TPB also contribute to the low energy spectrum. The number of these events can be estimated as:

$$N_{210Po} = r_{222Rn} \cdot (e^{-t/\tau_{210Pb}} \cdot \tau_{210Pb} + t)/_{t_2}^{t_1} \tag{8.3}$$

with r_{222Rn} the constant rate of ^{222}Rn decays in the detector and t_1 and t_2 the start and end times of the background runs counted from the time when the detector was filled with liquid argon. This works out to fewer than 2 events.

8.2 DEAP-1 background rates

Analyzing the data to set a limit on the WIMP-nucleon cross-section requires the knowledge of the background rate in the ROI. I will first define the ROI for the 3 detector versions.

The standard TotalPE ROI is 120-240 PE. To judge the success of background reduction efforts, comparing the same TotalPE region however is not appropriate, because the background spectrum is not flat and each detector version has a different light yield. Changes in rate might be just due to looking at a different range of the spectrum. To compare backgrounds in different chambers, one has to look at the same range of energies. All calculations are thus also done for an energy range of 50-100 keV.

Due to differences in PMT response, the nuclear recoil band is not at the same Fprompt value for each detector version, which means that choosing a common Fprompt window would mean retaining different percentages of nuclear recoil events. To make the numbers comparable, one needs to chose an Fprompt window for each detector version such that a given percentage of nuclear recoil events are retained each time. A 50% recoil efficiency is the easiest and least error prone choice, it means choosing an Fprompt range from the mean of the nuclear recoil distribution to Fprompt = 1.

The nuclear recoil distribution is obtained by irradiating the detector with neutrons from an AmBe source. A sample distribution is shown in Fig. 8.4. The peak of the nuclear recoil band is modelled by a gaussian with adequate precision for this purpose. The recoil band is not perfectly straight in energy, its mean shifts due to the actual physics of the interaction[20] as well as due to energy dependent PMT effects.

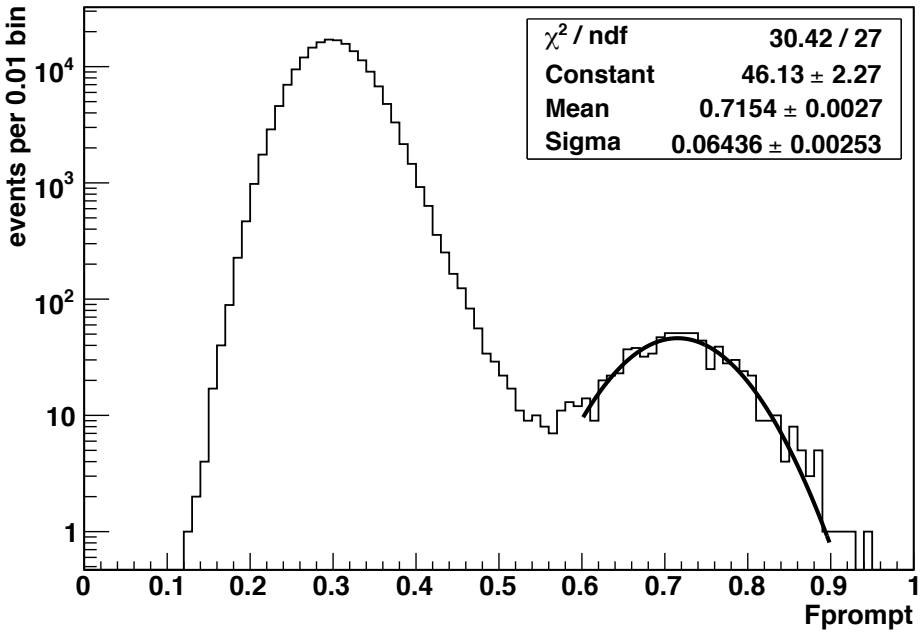

Figure 8.4: Fprompt distribution showing peaks for electron recoil and nuclear recoil events in DEAP-1 V3 at 120-240 PE.

The mean and standard deviation of the nuclear recoil band's Fprompt distribution is thus specific to the TotalPE window chosen.

The mean Fprompt values are determined in two TotalPE ranges for each detector version. Tab. 8.2 shows the gaussian fit values for all versions of the detector in the TotalPE region of interest, and Tab. 8.3 in an energy region of 50-100 keV electron equivalent.

	mean	standard deviation	energy window [keV]
V2	0.798 ±0.002	$4.47{\cdot}10^{-2}$	50-100
V3	0.712 ±0.002	$6.25{\cdot}10^{-2}$	26-52
V5	0.807 ±0.004	$5.7{\cdot}10^{-2}$	30-60

Table 8.2: Fprompt peak values of the nuclear recoil band in the energy ROI. Energies are given as electron equivalent.

	mean	standard deviation	TotalPE window
V2	0.798 ±0.002	$4.47 \cdot 10^{-2}$	120-240
V3	0.733 ±0.001	$4.35 \cdot 10^{-2}$	240-480
V5	0.816 ±0.003	$4.3 \cdot 10^{-2}$	200-400

Table 8.3: Fprompt peak values of the nuclear recoil band in an energy range of 50-100 keV (electron equivalent).

A cut is usually necessary in zfit to exclude events from outside the detector. Again, due to different PMTs, no universal zfit cut can be used for all detector versions. Zfit scans were done that correlate the real position of a source with the zfit parameter (see Appendix A). Based on this, the zfit cut corresponding to any desired range in real detector length can be found.

Tab. 8.4 shows the backgrounds in the same TotalPE range. Tab. 8.5 shows the background in the same energy range.

	Emin	Emax [keV]	Zmin	Zmax	background rate [μHz]
V2	50	100	-6	3	47 ±4
V3	26	52	-7.5	2.0	23 ±3
V5	38	76	-8.0	2.0	10 ±4

Table 8.4: Background rates at 120-240 PE, 50% recoil efficiency, along 10 cm of the detector (-5 cm to 5 cm).

	PEmin	PE max	Zmin	Zmax	background rate [μHz]
V2	120	240	-6	3	47 ±4
V3	240	480	-7.5	2.0	30 ±3
V5	200	400	-8.0	2.0	7 ±4

Table 8.5: Background rates at 50-100 keV (electron equivalent), 50% recoil efficiency, along 10 cm of the detector (-5 cm to 5 cm).

The comparison of background rates is a multi-dimensional problem, since cuts

on Zfit, energy and Fprompt are necessary. To get a more complete picture, the background rates are shown versus the recoil efficiency in figure 8.5.

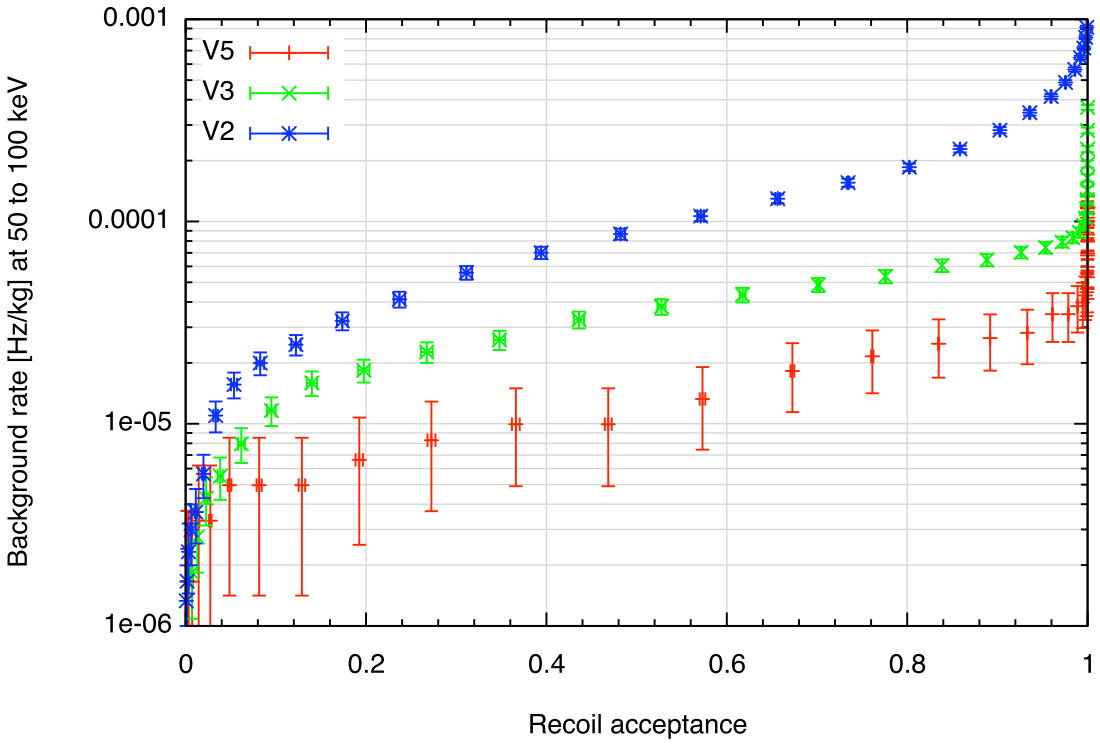

Figure 8.5: Background rates at 50-100 keV versus recoil efficiency.

For the V5 detector, the distribution of background events in Zfit and Fprompt is shown in Fig. 8.6 and 8.7.

8.3 WIMP-nucleon scattering cross section limit

The background in all versions of DEAP-1 is too high to obtain a competitive limit on the WIMP-nucleon scattering cross section. For completeness, it was nevertheless calculated based on the background free region between 45 and 65 keVee in V5 (Fig. 8.2) and is shown in Fig. 8.8, assuming the standard Dark Matter analysis as

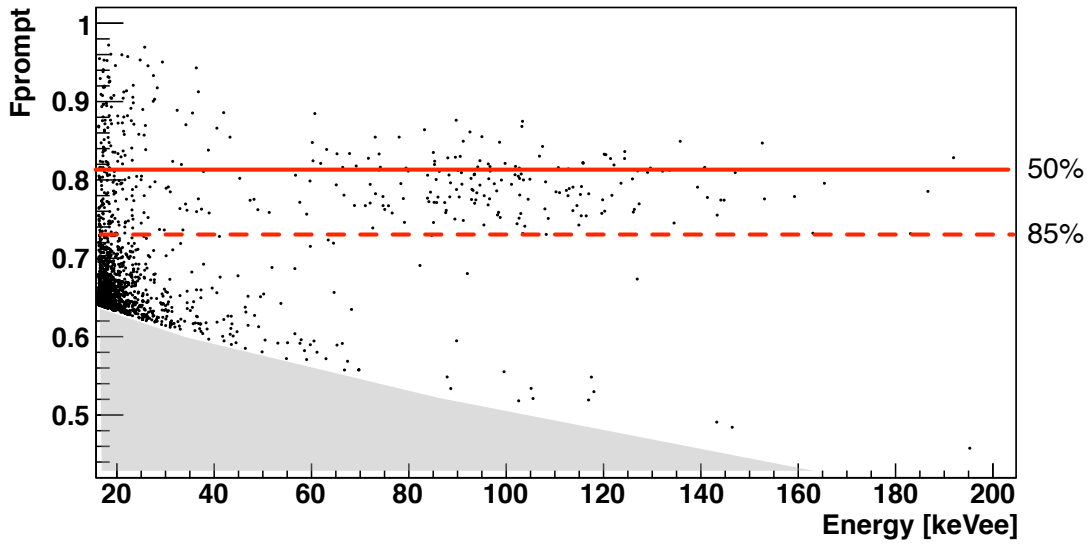

Figure 8.6: Distribution of V5 background events in Fprompt and energy. The 50% and 85% recoil efficiency cuts are indicated by the bars. The gamma band is blocked out.

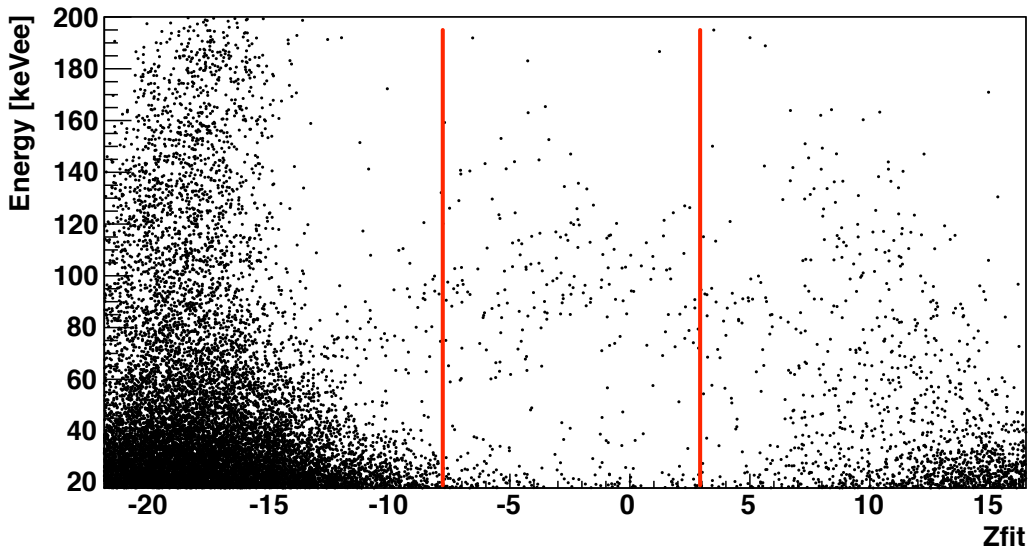

Figure 8.7: Distribution of V5 background events in Zfit and energy. The Zfit cut applied to the data in the low energy spectrum (Fig. 8.1) is indicated by the bars.

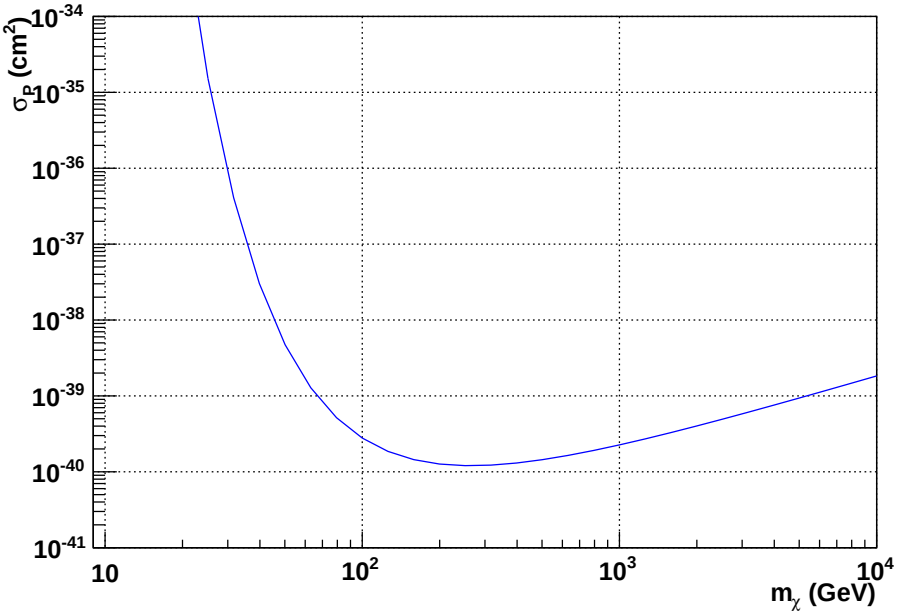

Figure 8.8: WIMP-nucleon cross section exclusion plot, showing for each WIMP mass the highest interaction cross section allowable from DEAP-1 V5 data (at 90% confidence level). The exposure is 71 kg·days.

summarized in Ref. [47].

The limit from V2 data is a factor of about four higher and can be found in H. Lippincott's thesis [48]. A better limit for V5 data could have been obtained in the absence of the window events.

8.4 Implications for DEAP-3600

The discovery of geometric backgrounds informed the design of the DEAP-3600 neck and the prevention of areas with low light collection efficiency is now a critical design criterion in similar experiments, such as MiniCLEAN[33]. Geometric backgrounds will thus be strongly reduced in DEAP-3600.

The dominant surface background contribution in DEAP-1 is ^{214}Po on the TPB. The spectrum has a peak at around 100 keVee, or 400 PE. The position of this peak is sensitive to the thickness of the TPB layer. For a 3 to 4 μm thick layer, the limit on radon contamination is the following:

DEAP-3600 is expected to achieve a light yield of greater than 8 PE/keVee. The ^{214}Po spectrum would thus peak at about 800 PE, which is well above the 240 PE or 30 keV upper limit of the energy region of interest. Some of these events will leak into the energy region of interest due to imperfect energy resolution though. With the current energy resolution, a fraction of $\rho = 6 \cdot 10^{-5}$ ^{214}Po surface events leak into the 15 to 30 keV region. The energy resolution gets better with higher light yield, so assuming the current energy resolution of 15% gives a conservative limit. A fraction of $\epsilon = 1.35 \cdot 10^{-3}$ events on the detector surface leak into the fiducial volume[10], and assuming all ^{214}Po can reach the detector surface, which is again a conservative assumption, about 3/4 of radon decays lead to a ^{214}Po surface event. Thus

$$R_{ROI} = \epsilon \cdot \rho \cdot \frac{3}{4} R_{Rn} < \frac{0.1}{3a} \tag{8.4}$$

so that a radon decay rate of

$$R_{Rn} < 2 \cdot 10^{-2}\text{Hz} \tag{8.5}$$

is required to meet the background goal for DEAP-3600. The subsequent decay of ^{210}Po on the TPB surface will lead to events at higher energy, since the energy loss is higher for this lower energy alpha, thus the peak will be at higher energy and fewer events will leak into the region of interest than for ^{214}Po.

The target thickness for TPB on DEAP-3600 is about 0.9 μm (see Chapt. 10). At this thickness, the ^{214}Po alpha loses a minimum of about 100 keV in the TPB, which would appear as about 10 keV in addition to the visible 48 keV contribution from the

recoil nucleus. The peak would thus be at around 60 keV leading to a limit on the radon rate of

$$R_{Rn} < 1 \cdot 10^{-4}\text{Hz}\,. \tag{8.6}$$

Simulations never include all possible effects, and tails in distributions are often underestimated. The design goal for DEAP-3600 is $R_{Rn} < 1 \cdot 10^{-5}$Hz[14], for a safety factor of ten.

A thicker TPB layer shifts the ^{214}Po spectrum to higher energies and thus loosens the purity requirement, but makes the transmission of light to the light guides less efficient.

The next strongest contributor to the background spectrum is PSD leakage. The higher light yield in DEAP-3600 will strongly reduce the PSD leakage. The expected leakage is indicated by the blue line in Fig. 8.1.

Finally, the simpler optical interface between the light-guides and the PMTs in DEAP-3600 is expected to eliminate the window event population, so that all the dominant contributions to the background spectrum in DEAP-1 can reasonably expected to be absent in DEAP-3600.

Another background observed in DEAP-1 is from ^{210}Po in the acrylic vessel. Based on the rate observed at intermediate energies (see Sect. 6.3.2), the rate at low energies is so small that it comes in two orders of magnitude below the other backgrounds. The acrylic for DEAP-3600 is produced under much stricter quality control in place and will thus have an even lower contamination with ^{210}Po. A complete summary of purity requirements for the acrylic can be found in Ref. [14].

Chapter 9

TPB scintillation under alpha particle excitation

The wavelength shifter TPB is used in DEAP-1 and DEAP-3600 to shift the argon scintillation light (at 128 nm[16]) to the visible spectrum, so that it can penetrate the acrylic light guides and reach the PMTs. It was previously unknown if TPB scintillates under alpha particle excitation and if so, what the scintillation efficiency is and what the pulse shape looks like.

Alpha particles from the primordial thorium and uranium chain can enter the TPB from deposits on the acrylic surface and from contaminations in the acrylic up to about 80 μm away from the TPB. These alpha particles will deposit varying amounts of energy in the TPB, depending on their original energy when emitted, the angle with which they enter the TPB and the depth from where they come in the acrylic. Should the TPB scintillate, some fraction of these events might appear in the energy region of interest for DEAP, so knowing the scintillation light yield is important to determine the expected background rate. If they are also in the Fprompt window

of interest, they cannot be discriminated using pulse shape discrimination methods, and could be a dangerous source of background.

Initial experiments done by R. Mathew in our lab showed that TPB does indeed scintillate under alpha particle excitation[51]. The plan for studying the TPB scintillation more systematically was to produce TPB films of various known thicknesses of the order of a few micrometers, to irradiate those films with an alpha source and to measure the scintillation response using the same type of PMT that was used on DEAP-1 at the time.

The following sections in this chapter are a reproduction of a published paper (Ref. [62]).

9.1 Production of thin TPB films of known thickness

9.1.1 Apparatus

TPB films of thicknesses in the order of 2-4 μm were produced by evaporating crystalline scintillation quality TPB powder from American Chemicals LTD under vacuum onto glass or polished acrylic plates. The TPB was evaporated from a quartz glass crucible 1 cm high and 1 cm in diameter located at the bottom of the chamber. The crucible was heated to the target temperature of approximately 200° C by means of a heating wire wrapped around it (see figure 9.1). An OMEGA resistance temperature sensor was clipped to the heating wire near the crucible and its readout was coupled to the power supply of the heater to maintain a constant temperature. The glass or acrylic plates were held on a rack 17.8±0.3 cm above and centred on the crucible.

Installed at the same height and on each side of the rack were two quartz crystal deposition monitors to monitor the thickness of the deposited film.

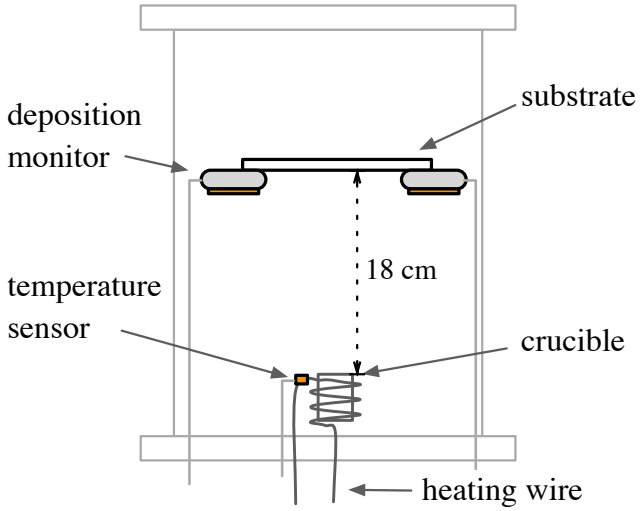

Figure 9.1: Diagram of the TPB evaporation system.

9.1.2 Method of evaporation

The glass plates (radius 6 cm) and acrylic plates (radius 10 cm, thickness 1.9 cm) were prepared for evaporation by the following steps:

1. Washed with tap water and detergent and rinsed with tap water.
2. Wiped with isopropanol.
3. Wiped with a mixture of 20% ethanol and 80% ultra pure water.
4. Wiped with aluminum foil.
5. Rinsed with ultra pure water.
6. Blown dry with nitrogen or argon gas.

Step 4 was introduced after observing that the TPB distribution on the cleaned plates showed signs of the surface treatment, possibly due to surface charges accumulated during wiping. The TPB surface on all substrates used for these measurements was very smooth and powdery white under visual inspection. This indicated that the TPB formed either very small polycrystalline structures or did not crystallize at all. Coatings produced two months later with the same procedure again showed clear signs of surface treatment in the form of visible local thickness variations for yet unknown reasons.

To calibrate the deposition monitors, two test depositions on glass plates were performed evaporating 0.364±0.005 g and 0.255±0.005 g of TPB respectively. During those test depositions, small glass pieces were also installed at the same height of the plates to get TPB films at positions further out than the radius of the plates. The deposition on both glass plates was started when the vacuum in the evaporator was at $5 \cdot 10^{-5}$ mbar. The pressure rose to up to $1 \cdot 10^{-4}$ mbar during the evaporation process.

For the measurement of the light yield, two TPB coatings were done. For coating A, 0.410±0.005 g of TPB was evaporated on an acrylic plate at $5 \cdot 10^{-5}$ mbar pressure in the evaporator. An evaporation temperature of 212°C was necessary to evaporate all the TPB in the very packed crucible. For coating B, 0.284±0.005 g TPB was evaporated at a pressure of $2 \cdot 10^{-4}$ mbar and a temperature of 200°C.

9.1.3 Deposition monitor calibration

The thickness of the TPB film across the substrate is a function of the radial distance from the axis of the crucible. To correlate the deposition monitor readings with the

thickness at the position of the light yield measurement, the TPB film on the glass substrate was scratched with a scalpel and the depth was measured using a Dektak 8M stylus profile meter from Veeco Instruments. A sample scratch profile is shown in Fig. 9.2. There was no indication that the glass beneath the TPB was damaged.

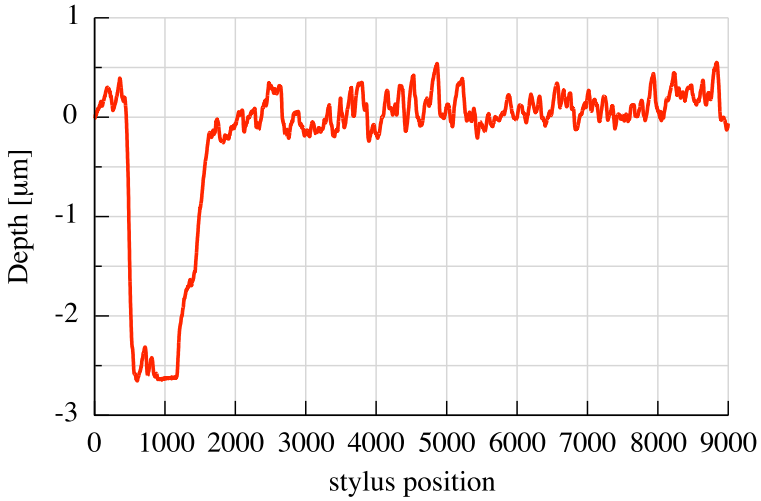

Figure 9.2: Typical profile meter scan of a scratch in the TPB film. The TPB thickness was determined by subtracting the average depth of the valley (stylus position 800 to 1200) from the average height of the TPB (position 1500 to 9000). The length of the scan is 500 μm

The scratch depths across the substrates, shown in Fig. 9.4, show a radial thickness variation consistent with the distribution developed by Chaleix et al.[15]:

$$\nu_d = \frac{\nu_e}{\rho} g(\theta) \frac{d}{(r^2 + d^2)^{3/2}} \tag{9.1}$$

where ν_e and ν_d are the rates of evaporation and deposition, d is the source-substrate distance, r is the radial distance from the axis of the crucible to a point on the substrate and ρ is the density of the TPB film. The geometric factor $g(\theta)$ depends on the evaporation conditions. For conditions with a volume right above the crucible where the probability of interaction between TPB molecules is very high, followed by

a volume where the molecules move in straight lines, the geometric factor is given by[15]

$$g(\theta) = \frac{1}{\pi}\frac{e^{\beta^2}(1+\mathrm{erf}(\beta))(\frac{3\beta\sqrt{\pi}}{2}+\frac{\beta^3}{\pi})+\beta^2+1}{1+\frac{u}{\alpha}\sqrt{\pi}e^{\frac{u^2}{\alpha^2}}(1+\mathrm{erf}(\frac{u}{\alpha}))}\cos(\theta) \tag{9.2}$$

where

$$\beta = \frac{u}{\alpha}\cos(\theta) \tag{9.3}$$

and θ is the angle between the axis of the crucible and a line from the crucible to

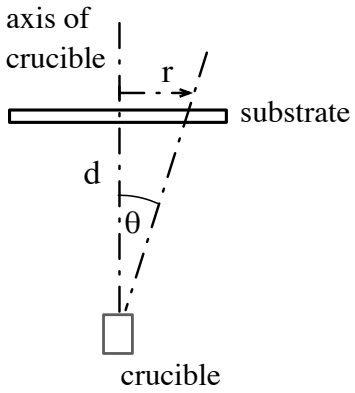

Figure 9.3: Geometry of the TPB evaporation system.

a point on the substrate, as shown in Fig. 9.3. The fit paramater $\frac{u}{\alpha}$, which depends on the vapour temperature at the boundary where the TPB molecules start moving without collisions, was found to be 0.284±0.013 for the substrate with 0.364 g TPB evaporated and 0.224±0.004 for the substrate with 0.255 g TPB evaporated.

The density of the TPB film enters into the mass distribution equation (eq. 9.1). It was fitted from the scratch measurement data to be 1.16±0.04 g/cm^3. The uncertainty takes into account the additional constraint that the deposition monitor readings, which also depend on the density of the TPB layer, had to be within errors of the scratch test measurement. This result is also consistent with the TPB density

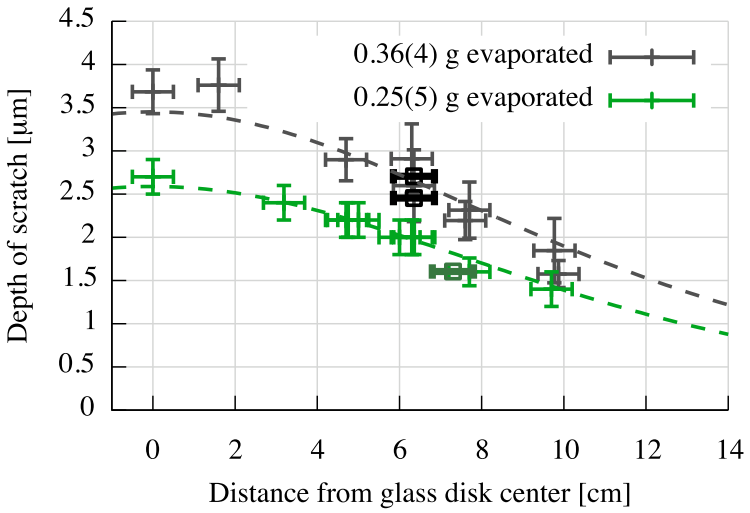

Figure 9.4: The variation in TPB thickness with radial distance from the crucible axis for the two test depositions on glass. The light thin points are results from the profile meter measurement, while the darker bold boxes are the readings from the deposition monitors. Dashed curves are best fits with the distribution from ref. [15].

estimated from the mass of the substrate before and after evaporation.

Since the deposition on sample A was done at a different temperature, the parameter $\frac{u}{\alpha}$ differed significantly from the above. It was fitted from the deposition monitor readings to be 0.36 ± 0.02 and the function was then used to calculate the TPB thickness at all locations where scintillation data were taken. The readings on the deposition monitors for the coating of sample B were not consistent with the above thickness distribution function, but instead indicated a uniform thickness distribution, as would be expected for an evaporation pressure high enough to not allow for a region of collision-less movement of the TPB molecules.

9.2 Method of measuring TPB scintillation pulses

Acrylic plates were used as a substrate for the light yield measurement because acrylic is also the material covered with TPB in the DEAP experiment. The acrylic plates were installed in the scintillation chamber shown in figure 9.5. The chamber consists of a stainless steel cylinder sealed on the bottom with a plain acrylic plate and on the top with the TPB coated acrylic plate. It was viewed by a 5" PMT (ETL 9390B), optically coupled to the top of the acrylic plate with a 1 mm thick silicone pad.

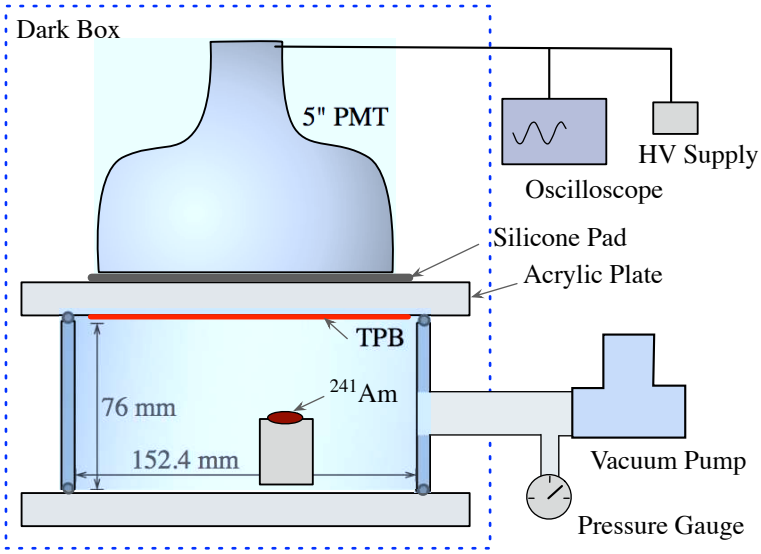

Figure 9.5: Diagram of the setup used to determine the light yield of a TPB film under alpha particle excitation.

A ^{241}Am alpha source (5.49 MeV alpha energy) with a collimator of 44° opening angle could be placed at arbitrary positions and heights inside the chamber. In order to not degrade the energy of the alpha particles, the chamber was evacuated to a pressure of typically $5 \cdot 10^{-2}$ mbar.

The light yield was measured with the ^{241}Am source irradiating different points on the TPB coatings, either pointing straight up or fixed at an angle θ of 47°, leading

to the alphas travelling distances of 1.8 to 6.5 μm through the TPB. The PMT was moved for each measurement such that the source was always aligned with the PMT's centre. The PMT signals were read out with a LeCroy WavePro 7100A oscilloscope and the traces were saved to file for offline analysis. Two pulse height spectra are shown in Fig. 9.6.

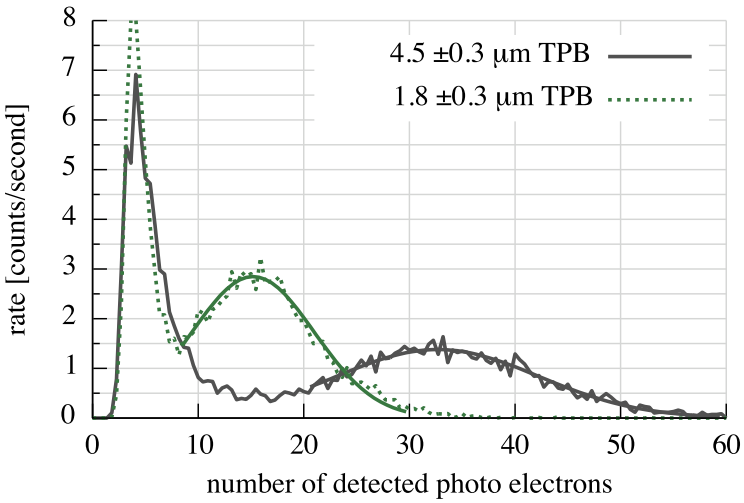

Figure 9.6: Background subtracted spectra and gaussian fits for alpha particles going through 4.5±0.3 μm (solid dark line)and 1.8±0.3 μm (dotted lighter line) of TPB. The peaks at approximately 5 PE are from background.

The energy loss of the alpha particles going through the TPB was simulated using SRIM[70] tables. The largest and smallest simulated energy loss for the pathlengths studied were 0.18 and 0.69 MeV. The TPB density of 1.16±0.04 g/cm^3, found previously, was assumed in the simulation.

9.3 Results: TPB light yield and pulse shape

The light yield measured for different pathlengths through the TPB is presented in Fig. 9.7. The average of these measurements is 71 PE/MeV with a standard deviation of 11 PE/MeV. The geometric acceptance of the PMT is 35%. Assuming a PMT efficiency of 23%[24] at 420 nm, the peak wavelength of TPB, 882±210 photons are emitted per MeV energy deposit. The uncertainty on this number does not include the uncertainty on the PMT efficiency, which is not quoted in the data sheet.

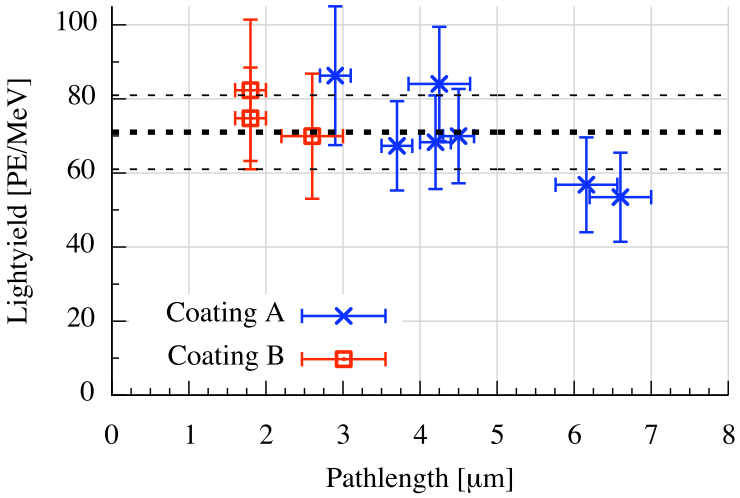

Figure 9.7: The measured light yield for different pathlengths the alpha particles had through TPB. The dashed lines represent the mean and standard deviation of the data. The points with the larger error bars on the pathlength variable were measured with the alpha source inclined at 47°.

The zero-suppressed scintillation pulse shape for two measurements is shown in Fig. 9.8. There is a region of fast decay followed by a region of slow decay, which were fit separately with a simple exponential decay function $A \cdot e^{-t/\tau}$ where A is a constant and τ is the lifetime. The fitted lifetimes are 11 ±5 ns and 275 ±10 ns. There are no significant differences in the pulse shapes for different TPB thicknesses.

The so called "fast to total" or "Fprompt" parameter, which is the ratio of the pulse intensity in a fast time window and the total pulse intensity, is often used to discriminate electromagnetic interactions in noble liquid detectors from nuclear recoils. Using a fast time window of 50 ns before to 100 ns after the peak position, which is the standard window used in DEAP, and a total integration time of 1 μs this parameter is 0.67±0.03 for alpha inducted TPB scintillation.

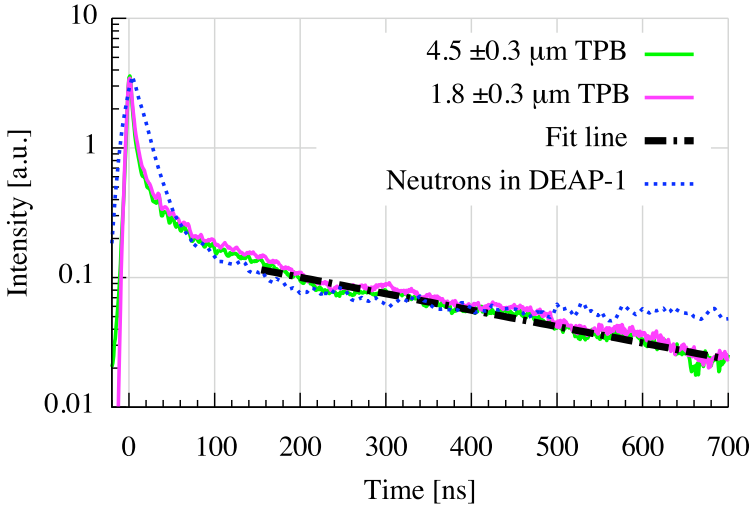

Figure 9.8: The solid curves are averaged pulse shapes of alpha induced TPB scintillation for data taken at TPB thicknesses of 1.8 μm and 4.5 μm. The dashed line shows best fit to the slow component of those traces. The dotted curve is the average neutron induced liquid argon scintillation pulse shape as measured in DEAP-1. It was normalized to have the same peak height as the TPB pulses.

9.4 Discussion

The theoretical thickness distribution curve describes the measured radial TPB thickness distribution well, even though the pressure in the evaporator as well as the distance between the TPB surface and the substrate change during evaporation. We therefore believe this method of deposition monitor calibration to be reliable for determining the TPB thickness at radii other than where it was directly measured.

The measured photon yield of 882±210 photons is a factor of 5 smaller than that measured by Hull et al.[38] for alpha scintillation in a TPB monocrystal. The light yields for coating A and B are consistent within errors, indicating that the pressure in the evaporator during the evaporation process has no significant influence on it. The two data points at 6.1 and 6.6 μm pathlength seem to be lower than the ones taken at shorter pathlengths. These points were measured with the source inclined by 47°, so that this effect is not caused by increased absorption in a thicker TPB layer. The other points measured with an inclined source do not show a reduced light yield. It is possible that the energy loss simulation becomes inaccurate for longer pathlengths. The TPB coatings were frequently exposed to fluorescent lighting in the lab without a noticable change in light yield over 3 months.

The main source of error on the light yield measurement comes from the uncertainty in the energy loss. This uncertainty is due to the uncertainty in the relative position between the alpha source and the the axis of the crucible during evaporation, and the uncertainty in the parameter $\frac{u}{\alpha}$ in the radial mass distribution equation. In future work, this error can be significantly reduced by developing a more advanced substrate positioning system in the evaporator and in the scintillation chamber.

Excitation of TPB with photons excites short lived singlet states[52, 63], which

have PMT signals with an Fprompt parameter of 1. The measurement of a 275 ns compontent indicates that alpha particles excite a triplet state, next to a short lived singlet state. This leads to the lower Fprompt parameter. The measured 11 ns for the singlet state has a large uncertaintly, since the shape is convolved with the time resolution of the PMT.

The Fprompt parameter of 0.67 measured here is very close to the Fprompt of 0.75 measured in the DEAP-1 detector for neutron events in liquid argon. WIMP and neutron signals are expected to have the same pulse shape and the average neutron pulse shape measured in DEAP-1 is shown in figure 9.8 for comparison. TPB scintillation from alpha decays could therefore lead to background events with Fprompt values similar to those of WIMP events. However, the liquid argon scintillation lifetimes of 6.7 ns for the singlet and 1600 ns[35] for the triplet component are much different from the TPB scintillation lifetimes measured here, suggesting that an improved pulse shape discrimination can be developed. In future work, we plan to study whether the scintillation pulse shape and light yield are temperature dependent.

9.5 Conclusion

We have shown that TPB scintillates under alpha particle excitation with a light yield of 882±210 photons/MeV and a pulse shape that consists of a fast and a slow component. This measurement will help understand surface alpha backgrounds in experiments using TPB and can be used to evaluate pulse shape discrimination methods for discriminating surface alpha from nuclear recoil events.

9.6 Acknowledgements

We would like to thank Prof. Gregory Jerkiewicz and Dr. Michał Grdeń for providing access to the profiler and assistance in using it, as well as Rob Gagnon for technical assistance. This work was supported by the National Science and Engineering Research Council of Canada (NSERC), by the Canada Foundation for Innovation (CFI) and by the Ontario Ministry of Research and Innovation (MRI).

Chapter 10

The DEAP-3600 TPB evaporation source

10.1 Design of the evaporation source

10.1.1 Objectives for the evaporation source

The inside of the DEAP-3600 acrylic vessel will be coated in TPB (see Sect. 3.1.2) by thermal evaporation, as has been successfully done for the DEAP-1 acrylic sleeve. The TPB coat should be done in such a way that the light conversion efficiency will be the highest possible and uniform all over the vessel. The conversion efficiency directly influences the light yield of the experiment and thus critically affects the pulse shape discrimination against electromagnetic background events. Literature values for the optimum coating thickness range from 0.07[18] (for 185nm light) to 0.2 mg/cm^2[52](for 58 nm light). The efficiency falls by roughly 10% when moving 0.03 mg/cm^2 in either direction.

Uneven coating thickness, and thus conversion efficiency, would lead to a worsening of the event position reconstruction power and thus affects the achievable background discrimination power, though calibration of this effect is possible using a uniform light source at the centre of the vessel. It should also not be possible for any TPB to be in the vessel but not adhere to the wall, since this would lead to visible light emission from locations other than the surface of the acrylic vessel, with unpredictable consequences for the position reconstruction power.

The evaporation source for the TPB must thus be designed to meet the following objectives:

1. The TPB layer produced should be on average 0.1 mg/cm^2 (or 0.9 μm) thick, over the roughly 10 m^2 surface area of the acrylic vessel. This means the evaporation source must be able to hold 20 cm^3 of TPB crystals.

2. It must not be possible for the crystalline TPB to fall out of the source.

3. The TPB thickness must not vary by more than 30% across the sphere.

4. On a microscopic scale, the thickness variation must be as small as possible.

5. There must be no pinholes, that is small areas without TPB cover.

6. The coating produced must be structurally stable enough to withstand being cooled down to liquid nitrogen temperature without flaking off.

A common way to make an evenly coated substrate is by rotating the substrate over the evaporation source. This is not possible with the DEAP vessel. Uniform thickness must thus be ensured through the geometrical design of the source.

There are two good places to deploy the source from: The intersection between the neck and the acrylic sphere, or the center of the acrylic sphere. We consider a spherical deposition source, called "the sphere", suspended in the center of the DEAP-3600 vessel (see Fig. 10.3). A cylindrical crucible in the center of the sphere holds the TPB, which can exit through a number of holes in the sphere. The TPB pressure inside the sphere should be high enough to ensure random motion, so that the TPB molecules exit the holes in random directions. Once the TPB molecules exit the sphere, the pressure should be low enough that they move in a straight path until hitting the substrate. The sphere is heated by a heating wire wrapped around it and the crucible in the center is heated radiatively from the sphere.

The design does not include a shutter, which I show will not be necessary to ensure a uniform thickness distribution. Another reason shutters are commonly used is to prevent the deposition of material other than the evaporate from being evaporated from the source and subsequently deposited on the substrate. Polonium isotopes in the TPB in particular are a concern here. This source will need to be heated up and kept just below the TPB evaporation temperature for some time, immediately before being deployed, to evaporate any polonium or other impurities with a lower vapour pressure than TPB. By not evaporating all the TPB from the source, impurities with a much higher vapour pressure will be left behind rather than be deposited on the vessel.

According to Hlawacek et al. [36], there is "a severe lack of understanding of the basic growth mechanisms" for layers of organic materials, and no certain way to address list items 4 to 6 is known. However, based on what is known about coatings with inorganic substances, and my experience in the lab, keeping the evaporation

rate and the pressure low leads to smooth and mechanically stable coatings. An evaporation rate of 1-2 Å/s worked well for DEAP-1 TPB coatings. A rule of thumb for the vacuum is that the mean free path of the evaporant should be at least twice the distance from the source to the substrate.

TPB coatings produced this way were found to be stable when immersed in liquid nitrogen[41].

10.1.2 Vacuum requirements

TPB is a large molecule, shown in Fig. 10.1. Analytic calculations of its mean free path can only be approximations. With a diameter $d = 1220$ pm for the TPB

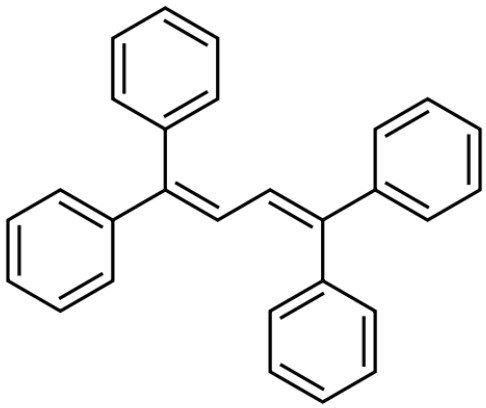

Figure 10.1: TPB molecule (from Wikipedia).

molecule, the approximate mean free path λ versus pressure p at a temperature $T = 200°\mathrm{C}$ is shown in Fig. 10.2. The equation used is

$$\lambda = \frac{RT}{\sqrt{2}\pi d^2 N_A P} \tag{10.1}$$

Typical pressures I have used in the evaporator used for DEAP-1 are between 10^{-3} and 10^{-5} mbar, and the calculated mean free paths are consistent with observations

of the TPB's behaviour. To get a mean free path of about 2 m, a bit over twice the distance between the source and the acrylic vessel if the source is in the center, a pressure of a few times 10^{-6} mbar is necessary.

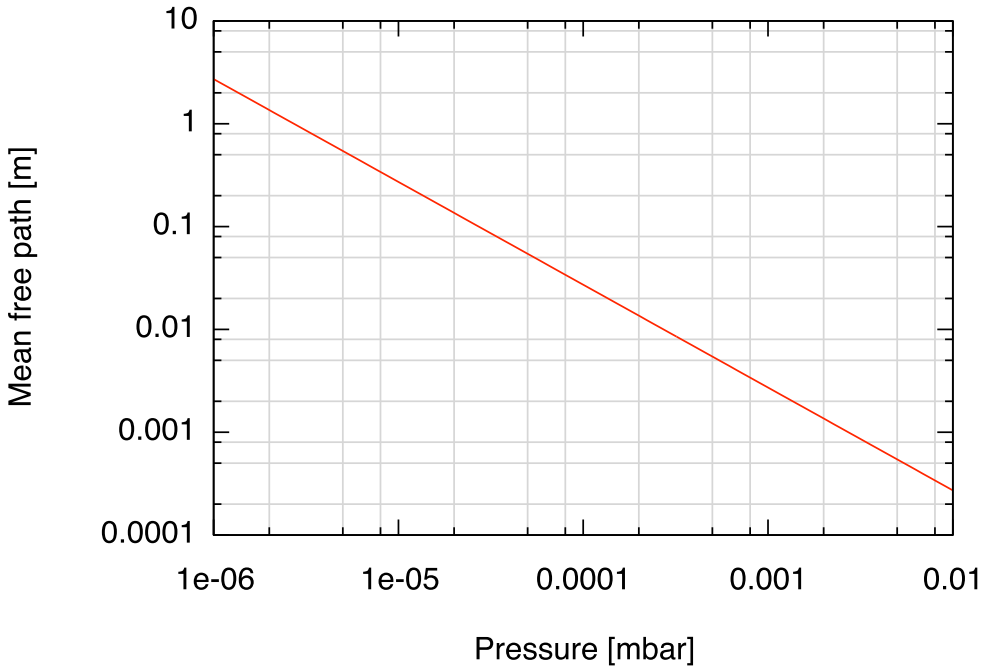

Figure 10.2: Approximate mean free path versus pressure for TPB.

10.1.3 Can a reasonable evaporation time be reached with this design?

The crucible in the center of the proposed source is similar in geometry to the one we use to coat the DEAP-1 detector parts with TPB. With the DEAP-1 crucible, we can reach a peak deposition rate R of 25 $\mathring{A}$/s about r=15 to 20 cm above the crucible. Due to the geometry of the crucible, this rate is only spread over an opening angle of

roughly 100°. The total area receiving the above mentioned rate is then

$$A_{dep} = r^2 \cdot 2\pi \cdot (1 - cos(\theta)) \tag{10.2}$$
$$= 9 \cdot 10^{-2}\, m^2$$

Once a critical pressure within the sphere of the evaporation source is reached, the mass coming out of the sphere must be about equal to the mass emitted from the crucible per second. The acrylic sphere has a radius of 85 cm, thus an area of about 9 m^2, about 100 times more than the above. The deposition rate on the acrylic sphere is then 100 times less, or 0.25 $\mathring{A}$/s. At that rate, it would take 11 hours to deposit 1 μm of TPB. This is a reasonable time frame for the deposition, especially considering that this is an upper limit, since the larger DEAP-3600 crucible can be expected to support a higher evaporation rate.

10.1.4 How big should the holes be?

The mean free path of a TPB molecule in the sphere should be only a fraction of the sphere's radius a to guarantee random motion. The critical pressure p needed to achieve a given mean free path λ is (equation 10.1 rearranged)

$$p = \frac{R_a T}{\lambda \sqrt{2} \pi d^2 N_a} \tag{10.3}$$

For a mean free path of 0.01 m at 200°C, the pressure required is 0.04 Pa.

Assuming the ideal gas law, the number of atoms needed to maintain the critical pressure is

$$N = \frac{p\,V}{k_B T} \tag{10.4}$$
$$= \frac{R_a V}{k_b\, \lambda\, \sqrt{2}\, \pi\, d^2\, N_a} \tag{10.5}$$

with

$$V = \frac{4}{3}\pi a^3 \tag{10.6}$$

the volume of the sphere.

The time it takes for that many atoms to be emitted initially can be estimated based on the experience we have with the DEAP-1 evaporator. The total mass deposited per second at 0.25 $\mathring{A}$/s is $R_{dep} \cdot A_{dep} \cdot \rho = 5 \cdot 10^{-7}\, kg/s$, with $\rho = 1.16\, g/cm^3$. One TPB molecule weights about $6 \cdot 10^{-25}$ kg, leading to the number of atoms emitted per second of $8 \cdot 10^{17}$.

Assuming that we get to the above deposition rate in 60 minutes and that the increase in rate is roughly linear, this leads to a rate function of

$$R(t) = 3 \cdot 10^{14} \frac{atoms}{s^2} \cdot t \ . \tag{10.7}$$

Linearity is a good approximation at the beginning, and becomes more inaccurate as the deposition rate approaches the final rate. Heating up the crucible takes about an hour, heating up faster leads to uneven evaporation. The number of atoms emitted up to a time t is

$$N_{emitted}(t) = \frac{1}{2}\, 3 \cdot 10^{14} \frac{atoms}{s^2} \cdot t^2 \tag{10.8}$$

This does not take into account that some of those atoms will leave through the holes.

We want the number of atoms leaving the sphere per unit time to be equal to or smaller than the number of atoms emitted from the crucible, to maintain the pressure required for random motion. The number of atoms hitting an area A of the wall of the sphere is

$$\frac{N_{hit}}{\Delta t} = \frac{1}{6}\frac{N}{V} < v > \cdot A \tag{10.9}$$

The mean velocity $< v >$ is given by

$$< v >= \frac{2}{\sqrt{\pi}} \sqrt{\frac{2\, k_b\, T}{m}} \tag{10.10}$$

This allows the calculation of the maximum area of holes to maintain the pressure. Should the evaporation rate go higher, N/V rises and thus more atoms will hit holes. Should the rate go lower, the TPB in the sphere will quickly drain and random motion can no longer be guaranteed.

The excess thickness behind each hole in the upper hemisphere if no shutter is used can be estimated based on the number of atoms leaving the crucible during the heat up before random motion is reached, and the area on the acrylic vessel visible from each hole. Atoms that hit a wall during heat up are assumed to scatter in a random direction, so those molecules, should they exit through a hole eventually, will have a random distribution and do not contribute to non-uniformity.

Table 10.1 lists relevant parameters calculated for a 11 cm diameter sphere, including the maximum radius each hole should have for 20 holes. It shows that the excess thickness accumulated without a shutter is negligible.

Parameter	value
Evaporation rate from crucible	$8{\cdot}10^{17}\,\frac{atoms}{s}$
Radius of sphere	0.055 m
Mean free path required	0.0055 m
Max total area of holes in sphere	$2.8\cdot10^{-3}$ m^2
Radius of each hole for 20 holes	6.7 mm
Percentage of surface in holes	7.4%
Time needed to reach random motion	<10 s
Excess thickness behind holes without shutter	$5{\cdot}10^{3}$ Å
Deposition rate on acrylic vessel	0.3 Å/s

Table 10.1: Hole size calculation for a spherical evaporation source of 11 cm diameter

10.1.5 Heat load on the acrylic vessel

The evaporation source will be kept at 200°C for an extended period of time, raising the question how much the acrylic sphere will be heated up radiatively from this. The heat transfer from a heated specular sphere at the centre of a diffuse reflecting sphere can be calculated as (equation 6-23 in [65]):

$$Q = \frac{A_1 \sigma (T_1^4 - T_2^4)}{\frac{1}{\epsilon_1} + \frac{A_1}{A_2}(\frac{1}{\epsilon_2})} \tag{10.11}$$

This works out to 46 W.

There are about 1000 kg of acrylic in the acrylic vessel, with a heat capacity of 1.25 kJ/(kg K), so $1.25 \cdot 10^6$ J are needed to heat the vessel by 1 K. At 46 W heat transfer, it will take $2.7 \cdot 10^4$ s or 450 minutes to heat the vessel by 1 Kelvin.

Heating up of the acrylic vessel is thus not a concern.

10.2 The prototype evaporation source

I built a prototype evaporation source shown in figures 10.3 and 10.4. The sphere is 11 cm in diameter and consists of two hemispheres made of aluminum, held together by a screw when the source is closed. A screw with a hole near its end, coming up through the top of the upper hemisphere, allows for the source to be suspended by a stainless steel wire. The copper crucible in the centre has a 2 cm inside radius and is 2.4 cm high. There are three small holes near the top of the crucible, 120° apart, where copper wires are attached. The three wires are tied to the top of the upper hemisphere, such that the crucible is suspended inside the sphere.

The size of the copper crucible is determined by the volume of TPB required to coat the detector with the desired thickness. The sphere in turn must be large

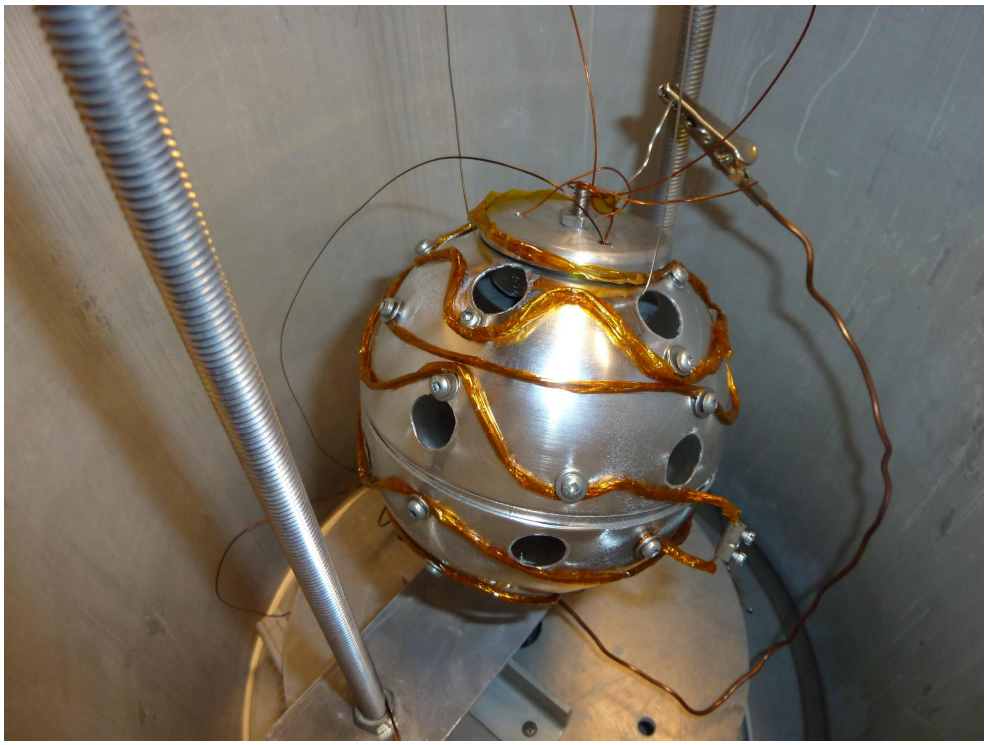

Figure 10.3: Prototype TPB evaporation source.

enough to contain the crucible, and small enough to fit through the neck of the DEAP detector, which is 20 cm in diameter. Less crucial considerations are the power required for heat up and the ease of handling and testing the source. The 11 cm diameter was chosen because it fulfilled the size requirements and because a suitable sphere of that size was commercially available.

The sphere has 20 holes 13 mm diameter, located at the points where the vertices of a dodecahedron inside the sphere would touch it. This way, the holes are spaced evenly on the sphere. Initial calculations done by C. Gilmour[30] indicated that 18 holes was the minimum number necessary to reach the required coating uniformity, though more holes lead to better uniformity. Twenty holes is the maximum number that can be distributed evenly on a sphere using a basic geometric object as guide

and there was no reason to complicated the drilling by using more holes.

Due to the geometry of the hole alignment, there are hexagonal areas free of holes. The holes are aligned in such a way that one such hole-free area is at the bottom of the sphere, so that any TPB that might fall out during the deployment phase will be contained within the source and be evaporated during heat up. Another such area is at the very top, which prevents excess TPB thickness from accumulating on the top hemisphere of the acrylic vessel during heat up before random motion is reached inside the sphere. The calculations show that such an excess is expected to be negligible, but this design gives additional confidence that no shutter is needed.

A nichrome heating wire wrapped in kapton tape is wound around the sphere and held in place by the washers of screws screwed into the sphere. The kapton tape serves to electrically insulate the heating wire from the sphere. The nichrome wires on the top and the bottom hemisphere are joined by a terminal plug so that the hemispheres can be separated and joined again easily if necessary. The total resistance of the nichrome wire is 4.6 Ω.

The source is instrumented with two PT-100 resistive temperature sensors, one on the outside of the copper crucible near its top, and one on the inside of the aluminum sphere near the equator.

10.3 The evaporation source test system

A test system was built from CF10 vacuum components, as sketched in Fig. 10.5, for the purpose of verifying the isotropy of TPB emission from the prototype source, and to gain experience with the heat up characteristics and general handling (installation, filling with TPB, electrical connections) of the source.

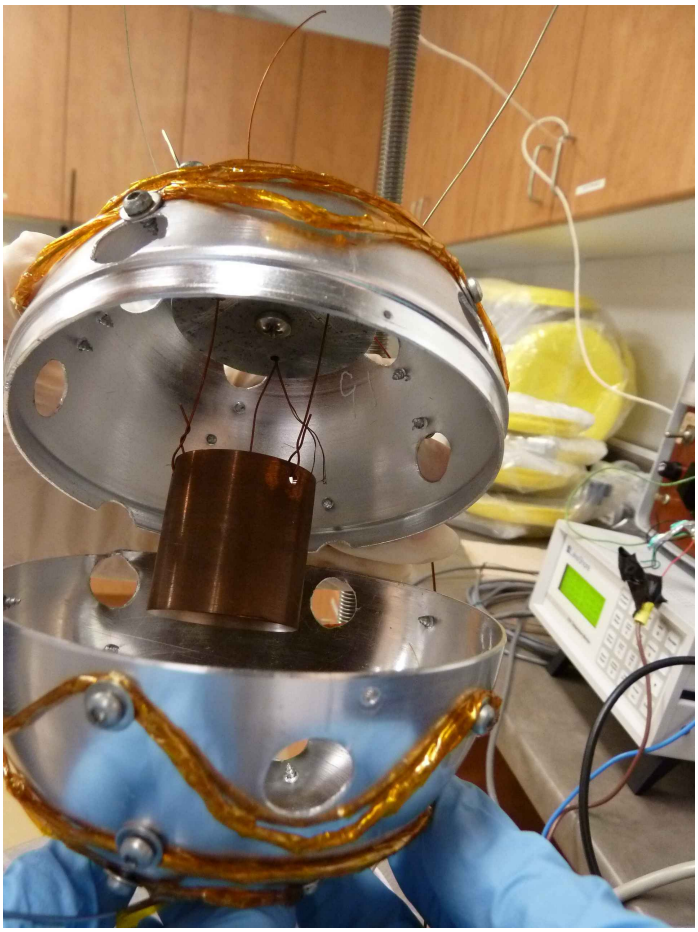

Figure 10.4: Inside of the TPB evaporation source, showing the copper crucible.

The test system is built in the shape of a cross with a 6-way cross in the centre, where the source is suspended. Quick access windows at the front and back arm of the 6-way cross allow easy access to the source. The left, right, top and bottom arm of the 6-way cross are connected to a nipple followed by a 4-way cross each. Each 4-way cross has a deposition monitor inside, and connected to its arms are a quick access window and an instrumentation feedthrough to access and to read out the deposition monitors. A pressure gauge is installed in the right arm and additional vacuum feedthroughs for the power supply (3-pin, of which 2 are used)

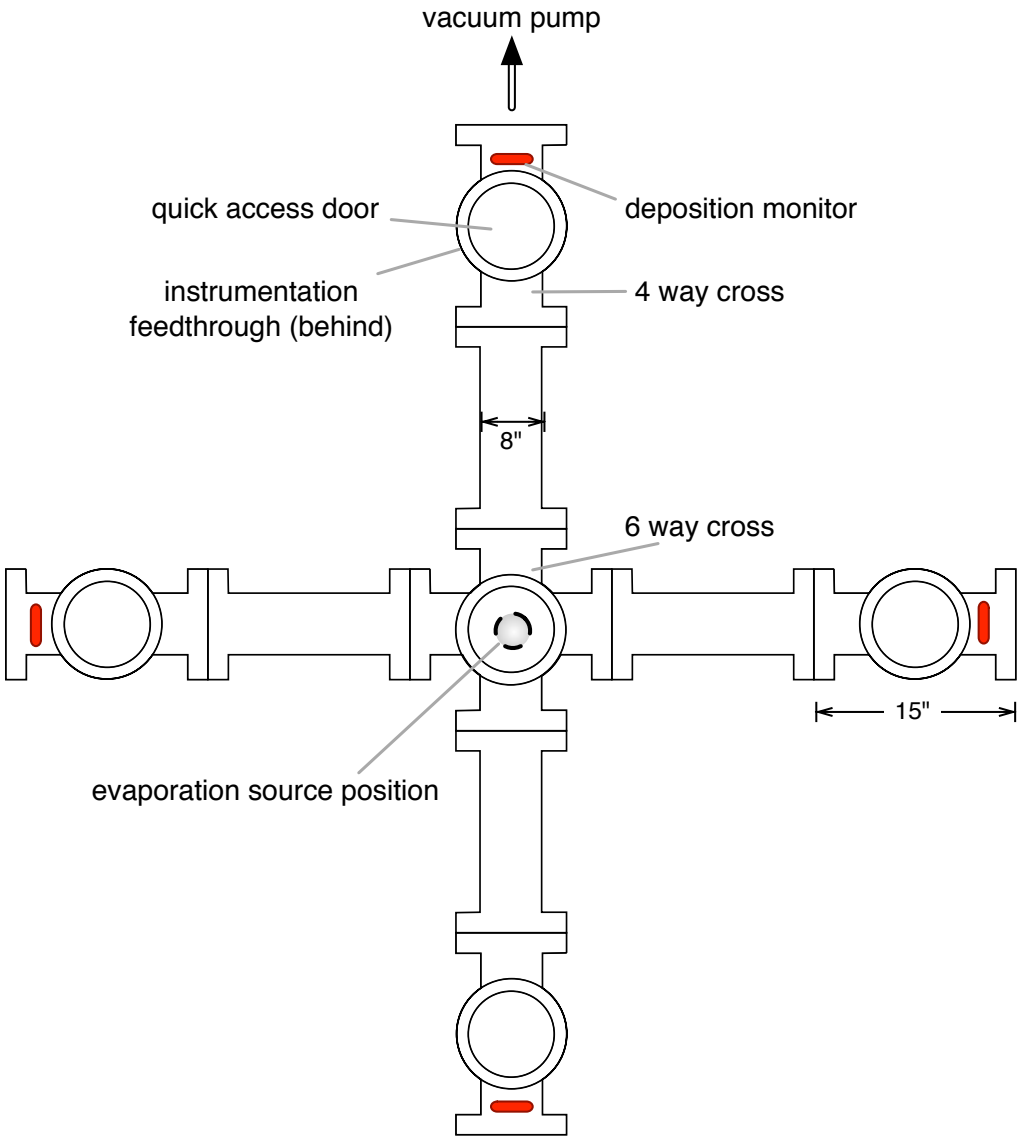

Figure 10.5: Sketch of the evaporation source test stand.

and temperature sensor read out (24-pin, of which 12 are used) are installed at the top.

Each piece of vacuum tubing is 15" long, so that the total diameter in the horizontal and vertical directions is 75", 5" more than the DEAP-3600 vessel. This system allows a direct measurement of the TPB deposition only at 4 points, however, more measurements can be taken by installing glass strips along the sides of the vacuum tubing, which can be removed after each evaporation to measure the thickness of the TPB layer. That way, the TPB thickness at the desired radius can be inferred.

The inside of the vacuum tubing is covered in aluminum foil that was cleaned with isopropanol. The foil prevents build up of TPB on the vacuum system, which would be hard to clean once the layer became thick enough to compromise the attainable vacuum through its outgassing.

The three temperature sensors (two on the evaporation source and one on the vacuum system near the source) are each connected to a 4-strand kapton-insulated in-vacuum wire on the vacuum side using 96.5-3-0.5 Sn,Ag,Cu solder with a melting point of 217 °C, followed by stranded copper wire on the air side. They are read out by the DEAP-3600 slow control system which was being tested in our lab at the time the evaporation source was tested.

The nichrome heating wire on the source is connected with "crocodile clips" to gauge 8 insulated copper wire going up to the vacuum side of the power feed through. On the air side, the electrical connection is continued with stranded copper wire plugged into a variable power source. The DEAP-3600 slow control system controls the power source based on the readings from the temperature sensors. When the temperature on the copper crucible reaches a user defined set point, the computer

program reduces the power by a user defined percentage.

10.4 Test results

10.4.1 Heat up characteristics of the source

Before the first evaporation, the source was heated up empty to verify that the radiative heating of the crucible worked and that the final crucible temperature was maintained. A stable temperature is necessary to guarantee high enough evaporation rates for random motion inside the sphere throughout the evaporation process.

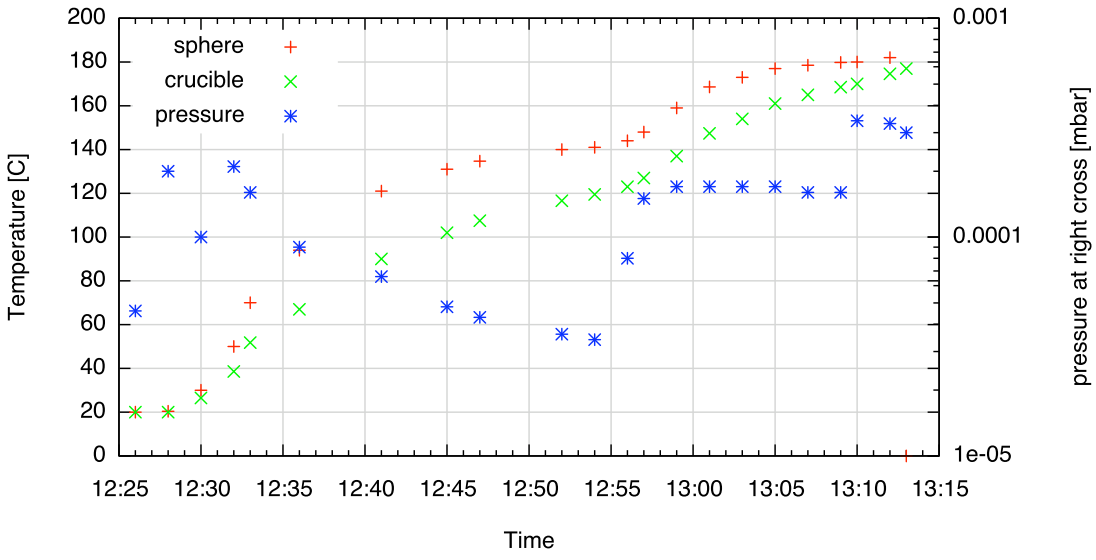

Figure 10.6: Heat up curve for the empty crucible. Pressure spikes coincide with the times when the power was increased.

The temperature of the deposition source during empty heat-up is shown in Fig. 10.6. Notice how closely the copper crucible follows the temperature of the sphere. The pressure in the vacuum system is shown as well. Each time the power is

increased, the pressure in the vacuum system rises abruptly, and then decreases again slowly.

The power was initially reduced to 0 W when the temperature set point was reached and turned back to full power when the temperature dropped below the set point again. This led to temperature fluctuations of about 10 °C on the aluminum sphere and of about 4 °C on the copper crucible. Lowering the power by 50% instead lead to temperature fluctuations of less than 2 °C on the sphere and less than 1 °C on the crucible.

10.4.2 Summary of test depositions

I did three test evaporations to quantify the properties of the prototype source. The temperature, coating thickness and pressure during the evaporations are shown in figures 10.7, 10.8 and 10.9.

First evaporation

For the first evaporation, glass sample slides washed with isopropanol were attached to the aluminum beam holding the deposition monitors at the top and bottom, and held by teflon pieces at the monitor position in the left and right arm as well as half way between the source and the monitor in the left arm.

The evaporation was started at a pressure of $1{\cdot}10^{-7}$ mbar and with 9.4 $\pm$0.1 g of 2 year old non-scintillation quality TPB in the crucible. It rose to $5{\cdot}10^{-5}$ mbar immediately after turning on the power to the heating wire.

In the beginning, the power was set at around 55 W up to a temperature of $110^{c}irc$C, then increased to 75 W up to $140^{c}irc$C and finally to 95 W. After about

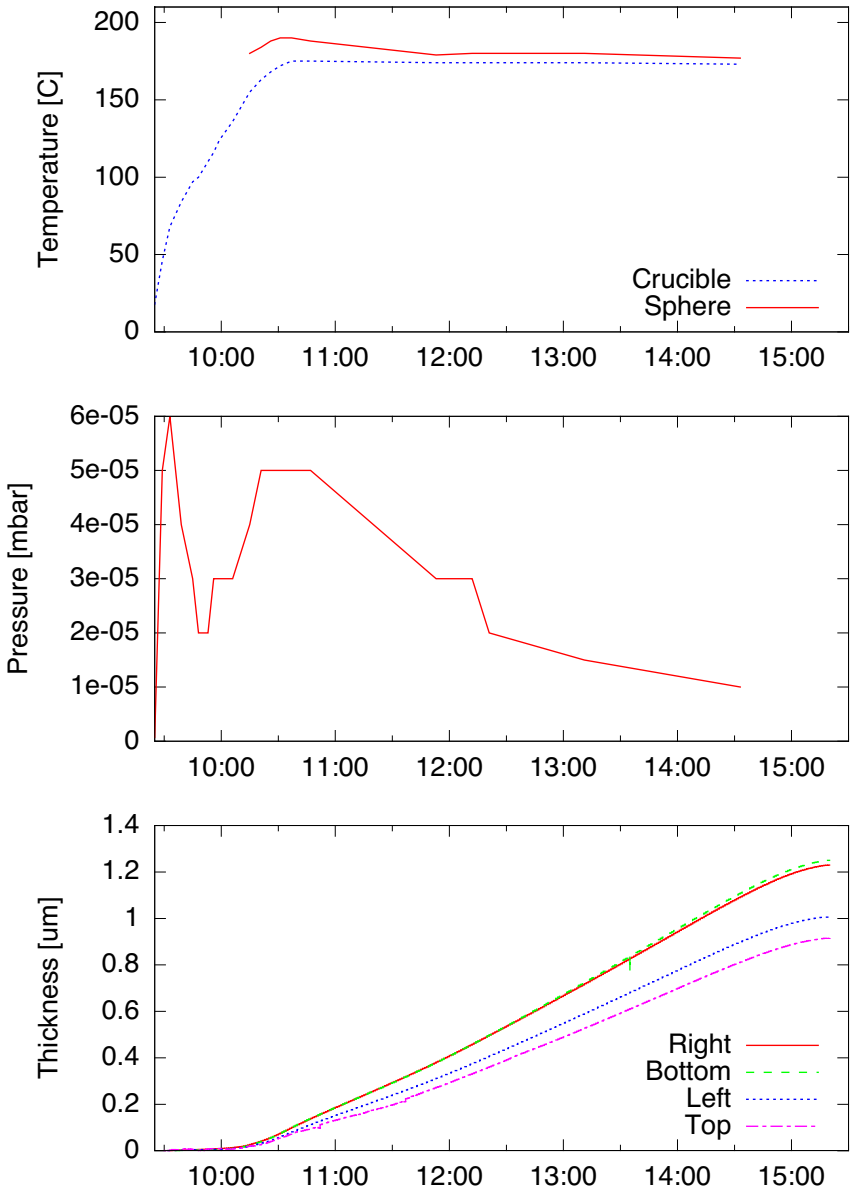

Figure 10.7: Temperature, pressure and thickness versus time of day during first evaporation. The top thickness monitor was slightly shaded by a piece of aluminum that came off the side of the vacuum tubing, causing a lower reading.

50 minutes, the deposition rate was at 1 $\mathring{A}$/s at a crucible temperature of 173 °C. The temperature set point was thus set to 175 °C. The deposition rate fluctuated between 0.7 $\mathring{A}$/s when the power was reduced to 50% and 1.1 $\mathring{A}$/s when the power was at 100%.

Second evaporation

For the second evaporation, glass sample slides washed in the ultrasonic cleaner first with acetone and then with ultra pure water were again attached to the aluminum beam at the top and the bottom, as well as placed at several locations along the left and right arm held by aluminum clamps. At the location of the right and bottom monitor, I placed acrylic disks 15 cm in diameter. One disk was sanded and the other optically polished. The polished disk had several small thin pieces of acrylic attached to it with vacuum grease, which were removed after the evaporation to facilitate profile meter scanning of the coating thickness.

The second evaporation was started at a pressure of $4{\cdot}10^{-6}$ mbar and with 4.2 g of fresh A&C chemicals scintillation quality TPB in the crucible. The pressure was higher than before because of the extra outgassing from the old TPB on the sides of the test system, and the outgassing from the extra acrylic pieces.

The power was ramped up in steps in the same way as before. The temperature set point was again 175°C on the crucible.

After the second evaporation, the aluminum with the TPB from the first two evaporations was replaced with fresh aluminum foil.

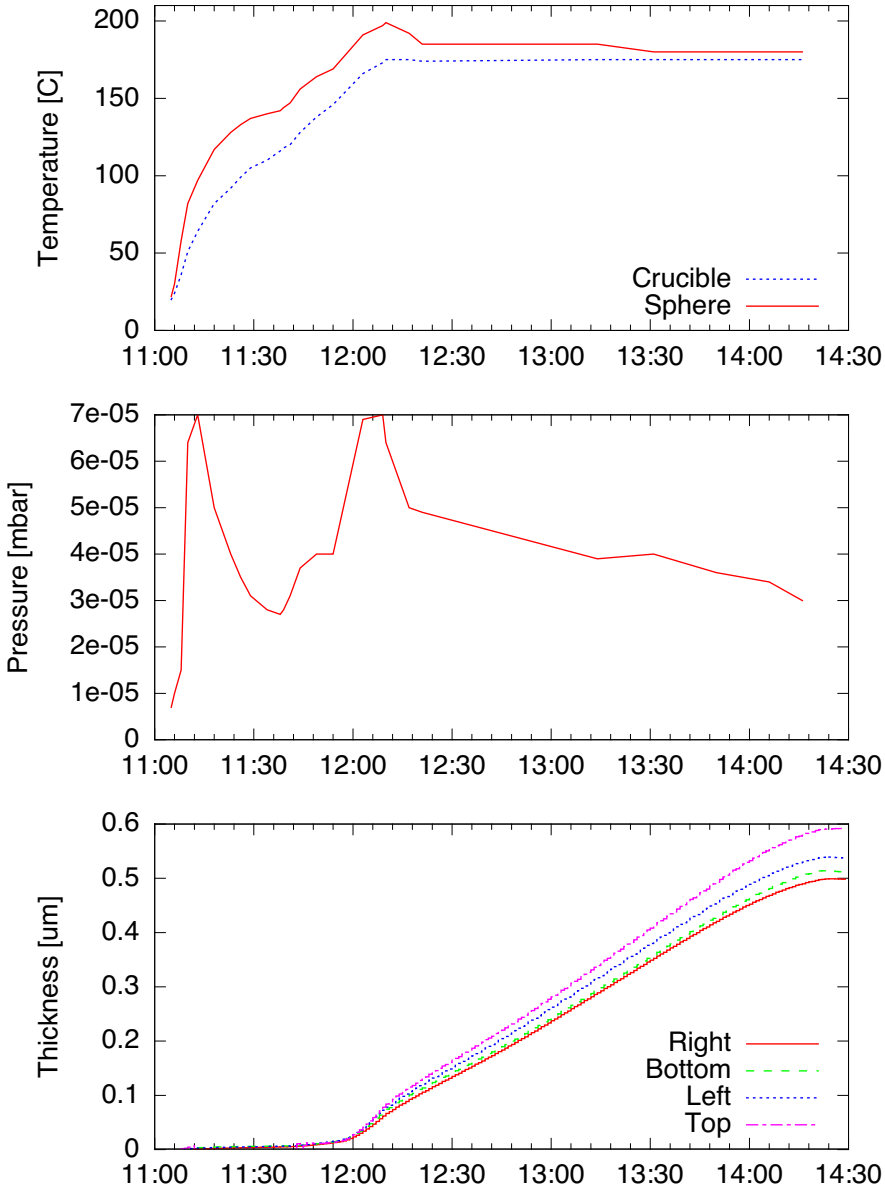

Figure 10.8: Temperature, pressure and thickness versus time of day during second evaporation.

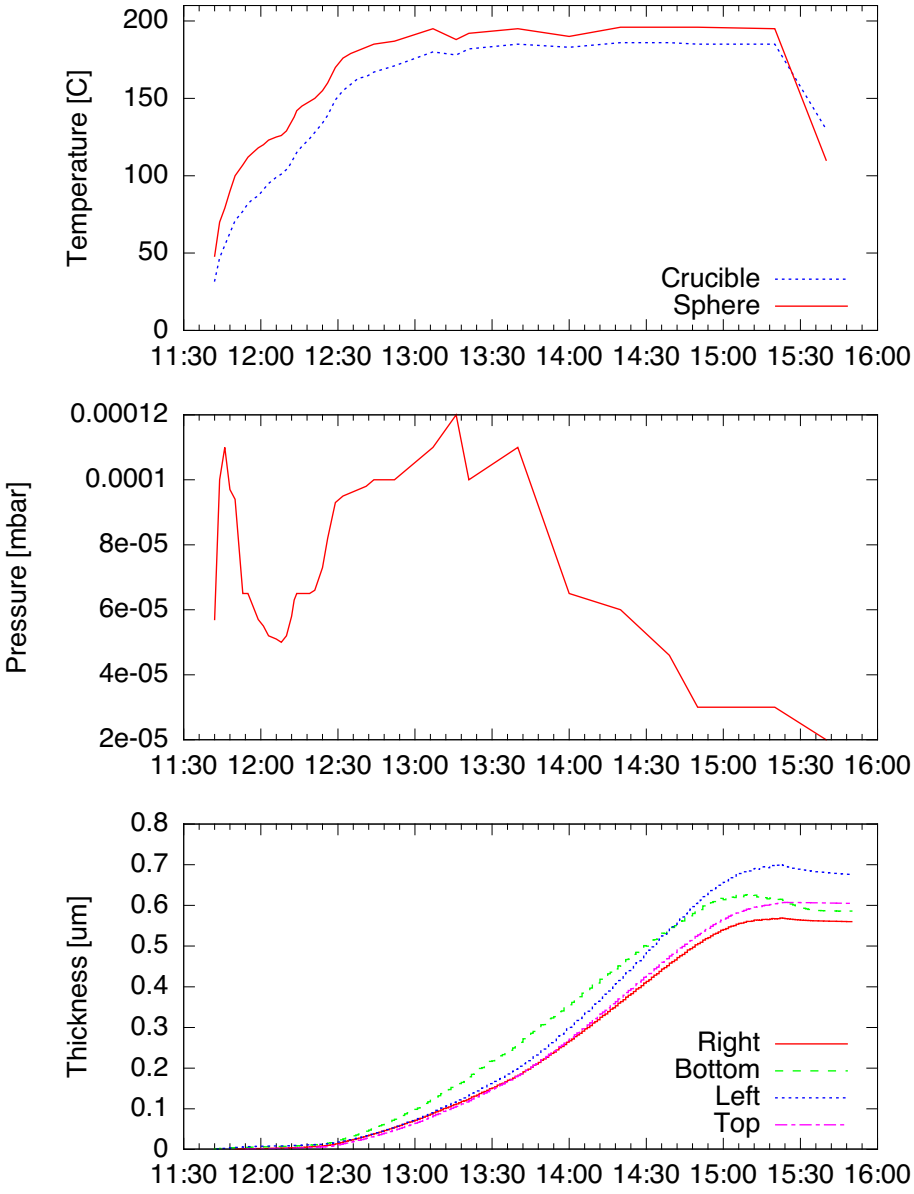

Figure 10.9: Temperature, pressure and thickness versus time of day during third evaporation.

Third evaporation

The previous evaporations were done in a rest gas atmosphere determined by the outgassing of stainless steel and aluminum. In order to more closely mimic the situation in the DEAP-3600 vessel, 150 g of 3 mm diameter acrylic beads from Fire Mountain Gems were put into the test system; 25 g in the left and the right arm and 100 g in the bottom arm. The area of acrylic was chosen to give a ratio of vacuum system volume over acrylic surface area similar to the DEAP-3600 acrylic vessel (V/A = 28.6). For the test system, $V = 1.1 \cdot 10^5$ cm^3 so an area of $A = 3.8 \cdot 10^3$ cm^2 was needed. For beads of 0.3 mm diameter, that makes 3300 beads. The beads have holes through them increasing the surface area, but only about 1700 were put in the system, so that the volume to area ratio is approximately correct.

Glass slides were again placed at various distances from the source along the arms. The slides were backed with aluminum foil.

The third evaporation started at a pressure of $2{\cdot}10^{-5}$ mbar and with 6.3 g of fresh A&C chemicals scintillation quality TPB in the crucible.

The TPB was taken from a new container and had a different structure than the TPB from the same company used during the second evaporation. Rather than a powder with fine crystals, it consisted of many long thin crystals and had a lower density, so that only 6.3 g would fit into the crucible.

The heat up characteristic was slightly changed, a temperature of 185°C was necessary to get the desired deposition rate of 1 $\AA$/s. The power was also increased to 120 W, which led to stronger than before temperature fluctuations each time the temperature set point was tripped (8°C on the sphere and 3°C on the crucible).

10.4.3 Uniformity and quality of the coatings

The glass slides coated in TPB during the first and second evaporation are shown in figure 10.10 while being illuminated by UV (254 nm) light. The top slide in the second evaporation shows clear signs of surface treatment where the ultra pure water ran off during cleaning. The other coatings are very uniform on visual inspection. The uncoated area on the bottom slide from the first evaporation was due to shading.

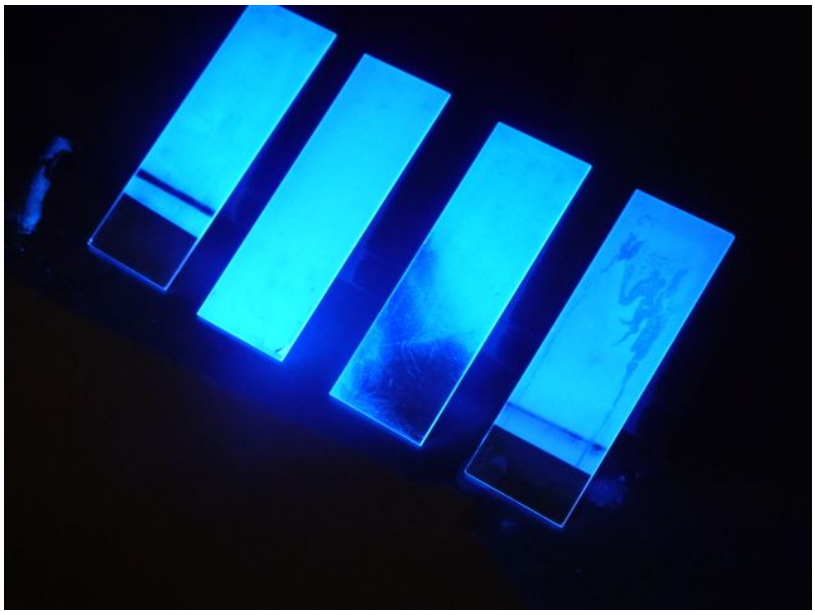

Figure 10.10: The TPB coated glass slides from the top and bottom evaporator arm for the first and second evaporation, photographed while being illuminated by UV (254 nm) light.

The glass slides held by teflon during the first evaporation had no TPB on them, while the teflon and the surrounding surfaces did. The glass slides held in aluminum clamps during the second evaporation also had no TPB on them, except on small areas closes to the aluminum. Both acrylic pieces had a visible coating, as did the glass slides that were attached to the aluminum beams holding the deposition monitors.

In subsequent evaporations, the glass slides were backed by aluminum foil, but again no TPB stuck to them.

The glass slides from the ends of the arms, which did have TPB coats, were scratched with a scalpel and the scratches scanned with a profile meter. The acrylic pieces attached to the larger acrylic plate were removed and the intersections also scanned. Figures 10.11, 10.12 and 10.13 show images of the surfaces together with the profile scans of those surface.

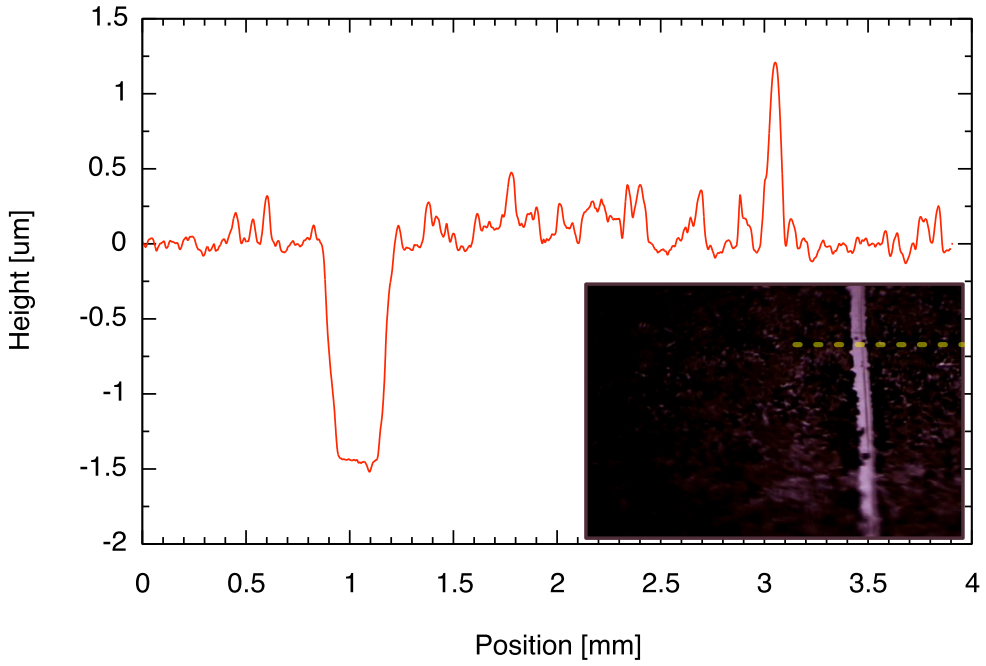

Figure 10.11: Scan across the scratch on top slide from first evaporation.

Tables 10.2, 10.3 and 10.4 summarize the deposition monitor readings and scratch scan data, and extrapolate the coating thicknesses found to 85 cm radius. The data is shown again in Fig. 10.14 with a linear fit.

The aluminum foil covering the inside of the vacuum system was inspected after the second evaporation. Clear shading effects where visible at creases, which had no

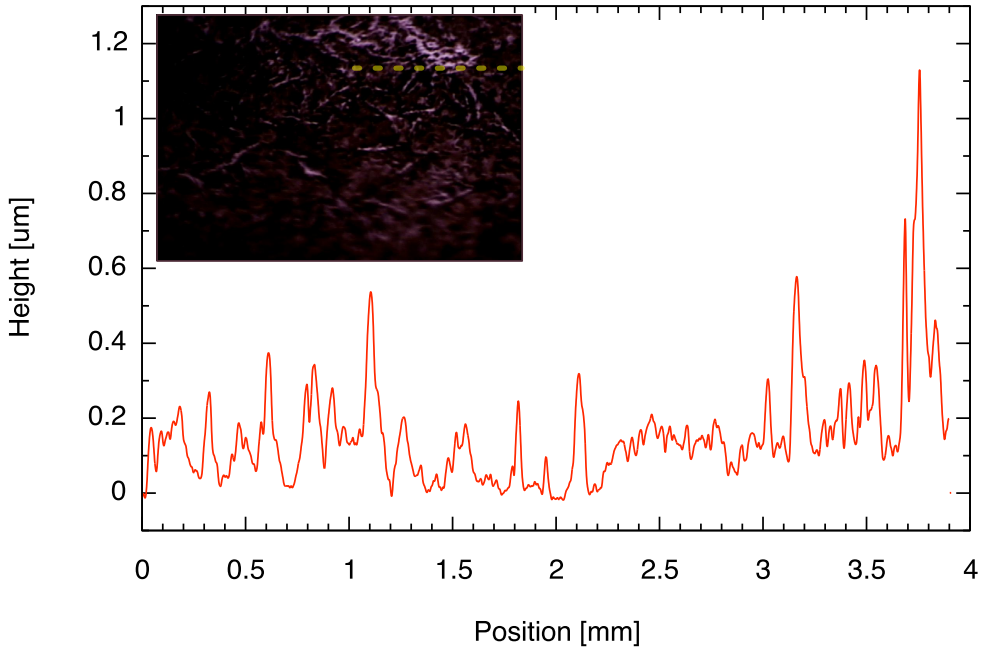

Figure 10.12: Scan across the roughest part of the TPB surface (top slide from first evaporation).

Sample	distance from source [cm]	thickness [μm]	extrapolated to 85cm [μm]
top monitor	62 ±3	1.18	0.63±0.04
left monitor	75 ±2	1.29	1.00 ±0.05
right monitor	75 ±2	1.58	1.23 ±0.07
bottom monitor	75 ±3	1.6	1.24 ±0.07
top glass	68 ±3	1.4 ±0.1	0.90 ±0.10
bottom glass	82 ±3	0.8 ±0.1	0.74 ±0.11

Table 10.2: Coating thicknesses from the first TPB evaporation. The top monitor was shaded slightly by a piece of aluminum. The bottom glass slide was shaded by the deposition monitor. The expected thickness was 0.9 μm

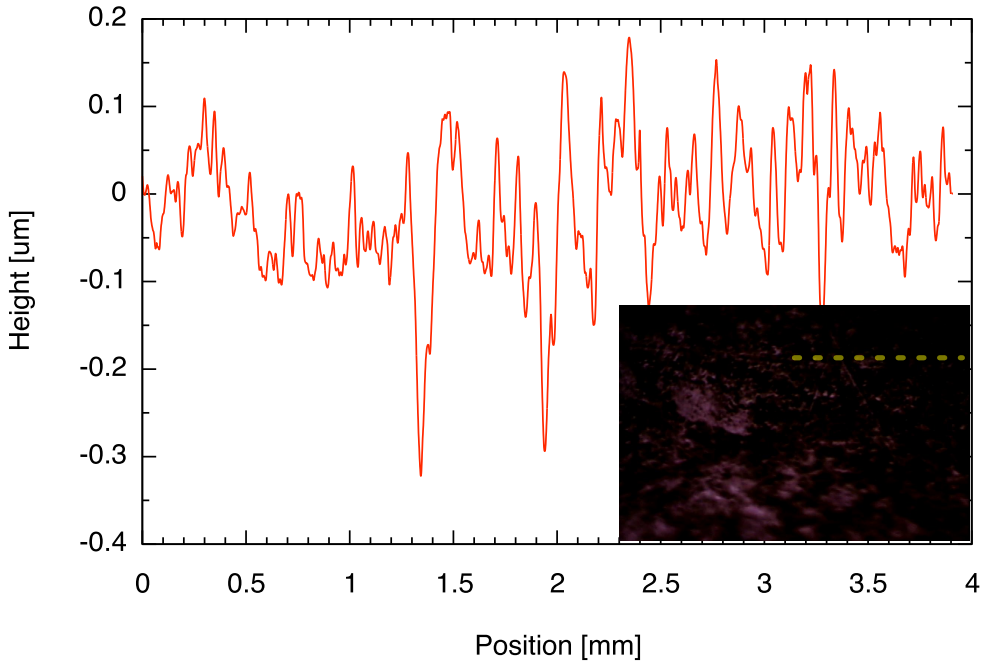

Figure 10.13: Scan across the TPB surface on the acrylic sample (second evaporation).

Sample	distance from source [cm]	thickness [μm]	extrapolated to 85cm [μm]
top monitor	62 ±3	1.02	0.54 ±0.04
left monitor	75 ±2	0.69	0.54 ±0.03
right monitor	75 ±2	0.64	0.50 ±0.03
bottom monitor	75 ±3	0.66	0.51 ±0.03
top glass	68 ±3	0.9 ±0.1	0.58 ±0.08
bottom glass	82 ±3	0.55 ±0.1	0.51 ±0.10
right acrylic	78 ±2	0.5 ±0.1	0.42 ±0.09

Table 10.3: Coating thicknesses from the second TPB evaporation. The expected thickness was 0.43 μm

Sample	distance from source [cm]	thickness [μm]	extrapolated to 85cm [μm]
top monitor	64.7 $\pm$2	1.04	0.60 $\pm$0.04
left monitor	73.5 $\pm$2	0.87	0.65 $\pm$0.04
right monitor	76.5 $\pm$2	0.71	0.58 $\pm$0.03
bottom monitor	73$\pm$2	0.79	0.58 $\pm$0.03

Table 10.4: Coating thicknesses for the third TPB evaporation. The expected thickness was 0.60 μm

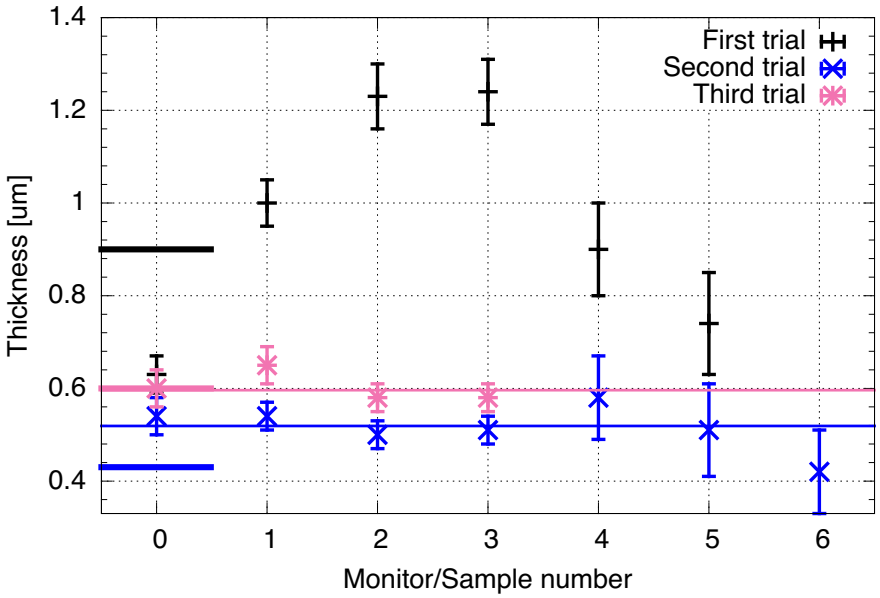

Figure 10.14: Measured TPB thicknesses for the monitors and glass samples from the three evaporations. χ^2/NDF are 5, 0.7 and 0.8 (first to third). The expected thickness is indicated by the thick short bars.

TPB cover on the side facing away from the source. This indicates that the TPB molecules were moving in straight lines. The quick access doors at the ends of the arms did have a very thin layer of TPB, as would be expected if the mean free path is about the length of the vacuum system arms.

After the second evaporation, the areas of aluminum foil closest to the source that also had the "shiny" side facing the source were free from TPB. This is likely due to re-evaporation and could be part of the reason for the excess thickness (see Fig. 10.14) observed. If this TPB was re-evaporated perfectly isotropically towards each sensor, it would merely have caused a common increase in the thickness reading on all sensors. There was however no clear line-of-sight from these areas to the sensors. TPB re-evaporating would most likely have hit the vacuum system at another location or the sphere, from where it would have been emitted towards only one or two sensors. Thus, this effect is most likely to increase any non-uniformity, rather than obscure it.

10.4.4 Discussion

The heat-up test showed that the radiatively heated copper crucible follows the temperature of the aluminum sphere and that the necessary temperature and stability can be achieved without any modification to the original design.

Upon increasing the power supplied to the heating wire, the temperature first increases quickly, but then the increase slows down as the power radiated at the given temperature approaches the power supplied. At about 93 W, this equilibrium point is around 180°C.

The power could be set to 93 W from the beginning, but this would lead to a large spike in pressure and the TPB would reach its evaporation temperature in well

under an hour. Experience with the DEAP-1 evaporator showed that heating up much quicker than an average of 3 °C/minute leads to TPB only evaporating from the outside of the crucible, leaving a column of unevaporated TPB in the centre. The evaporation rate then drops significantly until the column crumbles, which can take several minutes. By heating up slowly, the TPB later evaporates evenly and changes in the evaporation rate are avoided.

The power should be adjusted so that the equilibrium is reached near the desired evaporation temperature. Using more power leads to undesirable temperature fluctuations, as seen during the third evaporation.

During the first evaporation, the readings of the top monitor and the bottom glass slide TPB thickness were a bit low, which after opening the evaporator was found to have been caused by shading. In the case of the top monitor, a piece of aluminum foil had come lose. The glass pieces was shaded by the deposition monitor in the bottom arm. Excluding those two points, a standard deviation of 15% was reached, twice as good as the design goal.

All shading problems were then resolved, and the other two evaporations had standard deviations of 10% and 5%. The uncertainties of the average thicknesses in the last two evaporations are at the level of the fluctuations between individual monitor readings.

The improvement in the third evaporation can be attributed to letting the deposition monitors cool down before taking the final reading. The readings on the deposition monitors decreased as the system cooled down. This was not observed in the DEAP-1 evaporator and may be due to the larger radiative heat load of the aluminum sphere heating up the monitors. This is also at least part of the reason

why the average thickness for the first two evaporations was higher than expected.

The additional radiative heat load may also be to blame for the continued failure to coat glass samples not in good thermal contact with any metals.

On a microscopic scale, the coated glass slides showed excellent uniformity with no pinholes but occasional spikes. The acrylic coats were rougher with occasional deep holes that could be from scratches in the acrylic.

The pressure of several times 10^{-5} mbar at which the evaporations were performed is about a factor of 10 higher than the calculation of the mean free path indicated would be needed. The observations of TPB distribution in the test system indicate that the mean free path of TPB at this pressure is about the length of the arms of the test system. The mean free path calculation was of course only an approximation to begin with, and the quality of the coatings indicates that the pressure used here is adequate.

10.5 Conclusions

A thermal evaporation source was designed, built and tested that produces uniform coatings of the organic wavelength shifter TPB over the surface of a 85 cm radius sphere, without the need to rotate the sphere or the source. To the author's best knowledge, such a system is not commercially available or previously described in literature. The prototype evaporation source performs better than the design specification, producing coatings that are uniform within a few percent on a macroscopic scale, as well as smooth on a microscopic scale.

Some uncertainties remain. The environment of the source, in terms of radiative properties and rest gas compositions, will be different in the DEAP-3600 vessel.

Instead of being surrounded by shiny metal not far from the source, it will be surrounded by acrylic nearly a meter away, which may change the relationship between the input power and the rise in temperature. The outgassing atmosphere the TPB molecules travel through was matched as closely as possible to the final system by putting acrylic beads into the test system, but is likely not perfectly matched. The addition of the beads did not change the behaviour of the TPB significantly though, so this is not a big concern.

Testing the source in the 20" test vessel (a small scale mock-up of the DEAP-3600 acrylic vessel) would provide even more realistic environmental conditions and should be done if possible.

The distribution of thicknesses could effectively only be tested at 4 angles from the source, due to the continued failure to coat samples in the arms closer to the source. This could possibly be remedied by devising a better thermal coupling between those samples and the vacuum tubing. The source was not kept at the exact same rotation angle for each evaporation, remedying this uncertainty to some extend.

A lot remains unknown about the properties of TPB in thermal evaporations. The sudden failure to produce even coatings in the DEAP-1 evaporator (see chapter 9) is still unexplained. Recent literature indicates that even coatings can only be achieved with fresh TPB[2], but the first evaporation here was done with 2 year old TPB and the coatings produced were smooth. The TPB additionally seems to have differences from batch to batch.

The tests done here indicate that the source design will produce TPB coatings adequate for DEAP-3600. The smoothness of the coating can be tested by comparing the light transmission from e.g. an LED light on the evaporation source before and

after the evaporation using the PMTs. In case a problem is detected, the re-surfacer (used to remove the innermost layer of acrylic from the acrylic vessel) can be used to remove the TPB coat and another coating can be produced. I do not foresee this to be necessary.

Chapter 11

Conclusion

Dark Matter detectors meant to probe the parameter space down to ever lower WIMP-nucleon cross-sections require an ever more careful understanding of expected backgrounds, so that they may be modelled and if possible mitigated. In this work, the background in three iterations of the DEAP-1 prototype detector was investigated and found to be largely due to alpha decays from radon and its daughters interacting in previously unconsidered ways.

The most obvious contribution to events in the nuclear recoil band, though not strictly a WIMP background because of their high energy, were decays of ^{222}Rn, ^{220}Rn and daughters in the active liquid argon volume of the detector. The presence of these could be verified by analyzing the high energy spectrum and through timing coincidence analysis. Their decay rate was monitored throughout the three iterations of DEAP-1 and found to be stable around $2 \cdot 10^{-4}$ Hz and $2 \cdot 10^{-5}$ Hz respectively. Contributions to the high energy spectrum not from ^{222}Rn or ^{220}Rn could be excluded at a level above $4.3 \cdot 10^{-5}$ Hz (1 σ C.L.), indicating that purification efforts can be focused on these contaminants, and providing an upper limit for the high energy

contributions of other background sources.

A less likely albeit more dangerous contribution to the background, because also at the right energy for WIMPs, are surface alpha events. These happen when an alpha emitter decays on or near the inner detector surface. The hypothesis put forward in previous works that the main contribution to the background rate in DEAP-1 version 2 and 3 were surface backgrounds was shown to be incorrect. The new hypothesis put forward here, that radon alpha decays in low light collection areas of the detector (gap alphas) contributed most of the background in the nuclear recoil band, in particular at the WIMP energy region of interest, could be verified by studying the detector response after a radon spike.

Detector version 4/5 had an improved geometry informed by the new hypothesis as to the origin of background events, and showed a significant reduction in the background rate. Simulated surface background spectra match the remaining observed background, and the complete event rate in the nuclear recoil band and energy region of interest could be explained within statistics, though one contribution, the window events, are still poorly understood. The low level of surface backgrounds found, and the complete description of the observed spectrum, gives confidence in DEAP-3600 reaching the required low background level and informs the purity requirements of the argon and acrylic used in this detector.

The prevention of gap alpha events in DEAP-3600 is an ongoing effort in the collaboration, and a concern for similar experiments.

DEAP-1 was built for the triple and often conflicting purposes of understanding backgrounds in a liquid argon detector, determining the pulse shape discrimination power possible in liquid argon, and prototyping components for DEAP-3600. This

necessitated more careful and elaborate calibration and run selection than one would want in a production detector, and often the amount of good quality data left in the end was not as much as one could hope for. Yet, it was possible to understand most of the observed backgrounds and to mitigate some of them.

Understanding surface alpha events necessitated understanding the response of the TPB wavelength shifter to alpha particle excitation, and after gaining so much experience with it, designing the TPB deposition source for DEAP-3600 was a natural extension. The prototype source that was built and tested in a custom built test stand exceeded expectations for the level of coating uniformity produced. Further testing of the source should focus on determining why some surfaces do not get coated. Testing on a small scale detector mock up is planned to study and if necessary adjust the heat-up protocol in the pure acrylic radiative and outgassing environment. Work also needs to be done in assessing the radio purity requirements of the source, and in developing a mechanism to lower it into the acrylic vessel.

Bibliography

[1] Aalseth C.E., et al. *Search for an Annual Modulation in a p-Type Point Contact Germanium Dark Matter Detector.* Physical Review Letters, 107(1):141301, September 2011.

[2] Agramunt J., et al. *SiPMs coated with TPB : coating protocol and characterization for NEXT.* arXiv, 12012018, January 2012.

[3] Angle J., et al. *First Results from the XENON10 Dark Matter Experiment at the Gran Sasso National Laboratory.* Physical Review Letters, 100(2), January 2008.

[4] Angloher G., et al. *Results from 730 kg days of the CRESST-II Dark Matter Search.* arXiv.org, astro-ph.CO, September 2011.

[5] Begeman K., Broeils A., and Sanders R. *Extended rotation curves of spiral galaxies-Dark haloes and modified dynamics.* Monthly Notices of the Royal Astronomical Society, 249:523–537, 1991.

[6] Bernabei R., et al. *New results from DAMA/LIBRA.* arXiv, 1002.1028v1, February 2010.

[7] Bertone G. *Light from darkness: Searching for Dark Matter with gamma-ray and neutrino telescopes.* New Astronomy Reviews, 51(3):321–326, March 2007.

[8] Bertone G., Hooper D., and Silk J. *Particle Dark Matter: Evidence, Candidates and Constraints.* Phys. Rept, 405:279–390, 2005.

[9] Bolte W., et al. *A bubble chamber for dark matter detection (the COUPP project status).* J.Phys.Conf.Ser., 39:126–128, 2006.

[10] Boulay M. *Radon exposure and surface contamination limits for DEAP-3600.* Technical report, March 2010.

[11] Boulay M.G. and Hime A. *Direct WIMP Detection Using Scintillation Time Discrimination in Liquid Argon.* arXiv, 0411358, November 2004.

[12] Boulay M.G., et al. *Measurement of the scintillation time spectra and pulse-shape discrimination of low-energy beta and nuclear recoils in liquid argon with DEAP-1.* arXiv, 0904.2930v1, 2009.

[13] Brunetti R., et al. *WARP: a WIMP double phase Argon detector.* arXiv, 0411491, November 2004.

[14] Cai B., et al. *Surface background control in DEAP-3600.* Technical Report STR-2010-011 v5, DEAP collaboration, November 2010.

[15] Chaleix D., Choquet P., and Bessaudou A. *A spatial distribution study of a beam vapour emitted by electron-beam-heated evaporation sources.* J. Phys. D, 29:218–224, 1996.

[16] Cheshnovsky O. *Emission Spectra of Deep Impurity States in Solid and Liquid Rare Gas Alloys.* The Journal of Chemical Physics, 57(11):4628, 1972.

[17] Clowe D., González A., and Markevitch M.L. *Weak lensing mass reconstruction of the interacting cluster 1E0657-558: Direct evidence for the existence of dark matter.* Astrophys. J., 604(astro-ph/0312273):596–603. 8 p, December 2003.

[18] Davies G.J., et al. *UV quantum efficiencies of organic fluors.* Nuclear Instruments and Methods in Physics Research Section B, 117:421, October 1996.

[19] Doke T. and Masuda K. *Prestent status of liquid rare gas scintillation detectors and their new application to gamma-ray calorimeters.* Nuclear Instruments and Methods in Physics Research Section A, 420:62–80, 1999.

[20] Doke T., et al. *Let dependence of scintillation yields in liquid argon.* Nuclear Instruments and Methods in Physics Research Section A, 269(1), 1988.

[21] Doke T., et al. *Absolute Scintillation Yields in Liquid Argon and Xenon for Various Particles.* Japanese Journal of Applied Physics, 41(Part 1, No. 3A):1538–1545, March 2002.

[22] Duncan F., Noble A.J., and Sinclair D. *The Construction and Anticipated Science of SNOLAB.* Annual Review of Nuclear and Particle Science, 60(1):163–180, November 2010.

[23] El Zant A., Khalil S., and Okada H. *Dark Matter Annihilation and the PAMELA and ATIC Anomaly.* arXiv, 0903.5083, 2009.

[24] Enterprises E. *9390B series data sheet.* Technical report, 2009.

[25] Firestone R.B., et al. *Table of Isotopes*. John Wiley & Sons, 8 edition, 1998.

[26] Formaggio J.A. and Martoff C.J. *Backgrounds to sensitive experiments underground*. Annual Review of Nuclear and Particle Science, 54(1):361–412, December 2004.

[27] Gascon J., Lyon V.S.I., and Lemrani R. *DMMC Tool*. http://pisrv0.pit.physik.uni-tuebingen.de/darkmatter/.

[28] Gastler D., et al. *Measurement of scintillation efficiency for nuclear recoils in liquid argon*. arXiv, 1004.0373, April 2010.

[29] Gedanken A., et al. *Electronic Energy Transfer Phenomena in Rare Gases*. The Journal of Chemical Physics, 57(8), 1972.

[30] Gilmour C. *Design of a Vacuum Deposition System for the DEAP 3600 Detector*. Technical report, May 2010.

[31] Hanagodimath S., et al. *Fluorescence-quenching studies and temperature dependence of fluorescence quantum yield, decay time and intersystem crossing activation energy of TPB*. Journal of Luminescence, 129:335, April 2009.

[32] Heusser G. *Low-Radioactivity Background Techniques*. Annual Reviews in Nuclear and Particle Science, 45:543–590, 1995.

[33] Hime A. *The MiniCLEAN Dark Matter Experiment*. Proceedings of the DPF Conference, October 2011.

[34] Hitachi A., Doke T., and Mozumder A. *Luminescence quenching in liquid argon under charged-particle impact: Relative scintillation yield at different linear energy transfers.* Physical Review B, 46(18), November 1992.

[35] Hitachi A., et al. *Effect of ionization density on the time dependence of luminescence from liquid argon and xenon.* Physical Review B (Condensed Matter), 27:5279, May 1983.

[36] Hlawacek G., et al. *Characterization of step-edge barriers in organic thin-film growth.* Science, 321:108, 2008.

[37] Hu W., Naoshi S., and Silk J. *The physics of microwave background anisotropies.* Nature, 386(6):1–7, March 1997.

[38] Hull G., et al. *New Organic Crystals for Pulse Shape Discrimination.* IEEE Transactions on Nuclear Science, 56(3), 2009.

[39] Ishida N. *Attenuation length measurements of scintillation light in liquid rare gases and their mixtures using an improved reflection suppresser.* Nuclear Instruments and Methods in Physics Research Section A: Accelerators, Spectrometers, Detectors and Associated Equipment, 384(2-3):380–386, January 1997.

[40] Jochum J., et al. *The CRESST dark matter search.* Progress in Particle and Nuclear Physics, 66(2):202–207, April 2011.

[41] Kezwer J. *TPB Stability Testing with Liquid Nitrogen.* Technical Report DeapStr2010x006, Queen's University, September 2010.

[42] Komatsu E., et al. *Seven-year Wilkinson Microwave Anisotropy Probe (WMAP) Observations: Cosmological Interpretation.* The Astrophysical Journal Supplement, 192(2):18, February 2011.

[43] Kubota S., Hishida M., and Raun J. *Evidence for a triplet state of the self-trapped exciton states in liquid argon, krypton and xenon.* Journal of Physics C: Solid State Physics, 11:2645, June 1978.

[44] Kubota S., et al. *Liquid and solid argon, krypton and xenon scintillators.* Nuclear Instruments and Methods in Physics Research, 196(1):101–105, May 1982.

[45] Kuźniak M. *Acrylic purification and coatings.* In *Topical workshop on low radioactivity techniques (LRT).* 2010.

[46] Kuźniak M., Boulay M.G., and Pollmann T. *Surface roughness interpretation of 730 kg days CRESST-II results.* arXiv, 1203.1576, March 2012.

[47] Lewin J. and Smith P. *Review of mathematics, numerical factors, and corrections for dark matter experiments based on elastic nuclear recoil.* Astroparticle Physics, 6:87–112, 1996.

[48] Lippincott W.H. *Direct detection of dark matter with liquid argon and neon.* Ph.D. thesis, Yale University, 2010.

[49] Loosli H. *A dating method with 39Ar.* Earth and Planetary Science Letters, 63:51–62, 1983.

[50] Lubashevskiy A.V. and Yakushev E.A. *EDELWEISS experiment: Direct search for dark matter.* Physics of Atomic Nuclei, 71(7):1298–1301, July 2008.

[51] Mathew R. *Alpha-induced scintillation of Tetraphenyl Butadiene.* Technical report, December 2006.

[52] McKinsey D., et al. *Fluorescence efficiencies of thin scintillating films in the extreme ultraviolet spectral region.* Nuclear Instruments & Methods In Physics Research Section B-Beam Interactions With Materials And Atoms, 132(3):351–358, 1997.

[53] McKinsey D.N., et al. *The LUX dark matter search.* J. Phys. Conf. Ser., 203:012026, 2010.

[54] Miley H., et al. *Achieving low backgrounds in a variety of situations.* In *International workshop on superconductivity and particle detection.* 1994.

[55] Miyajima M., et al. *Average energy expended per ion pair in liquid argon.* Physical Review A, 9(3):1438–1443, 1974.

[56] Montaruli T. *The Antares Underwater Neutrino Telescope.* International Journal of Modern Physics A, 24(0):1656–1663, 2009.

[57] Mulliken R. *Potential Curves of Diatomic RareGas Molecules and Their Ions, with Particular Reference to Xe.* The Journal of Chemical Physics, 52:5170, 1970.

[58] Nakamura K. *The Review of Particle Physics.* J. Phys. G, 37, 2011.

[59] Nikkel J.A., et al. *Scintillation of liquid neon from electronic and nuclear recoils.* Astroparticle Physics, 29(3):161–166, April 2008.

[60] O'Dwyer E. *Radon Background Reduction in DEAP-1 and DEAP-3600.* Master's thesis, Queen's University, December 2010.

[61] Piro M.C. *Status of the PICASSO experiment for spin-dependent Dark Matter searches*. arXiv, 1005.5455, May 2010.

[62] Pollmann T., Boulay M., and Kuzniak M. *Scintillation of thin tetraphenyl butadiene films under alpha particle excitation*. Nuclear Instruments and Methods in Physics Research Section A, 635(1):127–130, 2011.

[63] Porter F. and Topp M. *Nanosecond flash photolysis*. Proceedings of the Royal Society A, 315:163–184, 1970.

[64] Schnee R.W. *Introduction to dark matter experiments*. arXiv, 1101.5205, January 2011.

[65] Siegel R. and Howell J.R. *Thermal radiation heat transfer*. McGraw-Hill Inc., 1st edition, 1972.

[66] Sigma-Aldrich. *Material Saftey Data Sheet - TPB*. Technical report, October 2010.

[67] The CDMS Collaboration. *Dark Matter Search Results from the CDMS II Experiment*. Science, 327(5973):1619–1621, March 2010.

[68] The IceCube Collaboration. *Multi-year search for dark matter annihilations in the Sun with the AMANDA-II and IceCube detectors*. arXiv, 1112.1840, December 2011.

[69] Thonnard N. and Hurst G.S. *Time-Dependent study of VUV emission in Argon*. Physical Review A, 5(3):1110, 1972.

[70] Ziegler J., Biersack J., and Ziegler M. *The Stopping and Range of Ions in Matter*. SRIM Co.

Appendix A

DEAP-1 data quality and calibration

This is a summary of basic detector characteristics relevant for background analysis. A basic property of any particle detector is the energy calibration. In scintillation detectors, the light yield relates the number of photons produced, or in this case the number of detected photo electrons, to the energy deposited in the scintillator. The light yield of the 60 keV peak from an AmBe source in DEAP-1 is shown in figures A.1 and A.2 versus time.

The apparent drop in light yield from V3 to V5 cannot be taken at face value, because the single photo electron charge was not determined with the same method, and there are indications that the SPE charge in V3 was too low.

The drop of the light yield from the beginning of the V5 run to the end however is real. The first suspect when light yields drop is a progressive "poisoning" of the liquid argon through the slow addition of air, i.e. nitrogen, which would quench the scintillation light. This would also lead to a shorter observed triplet lifetime. As

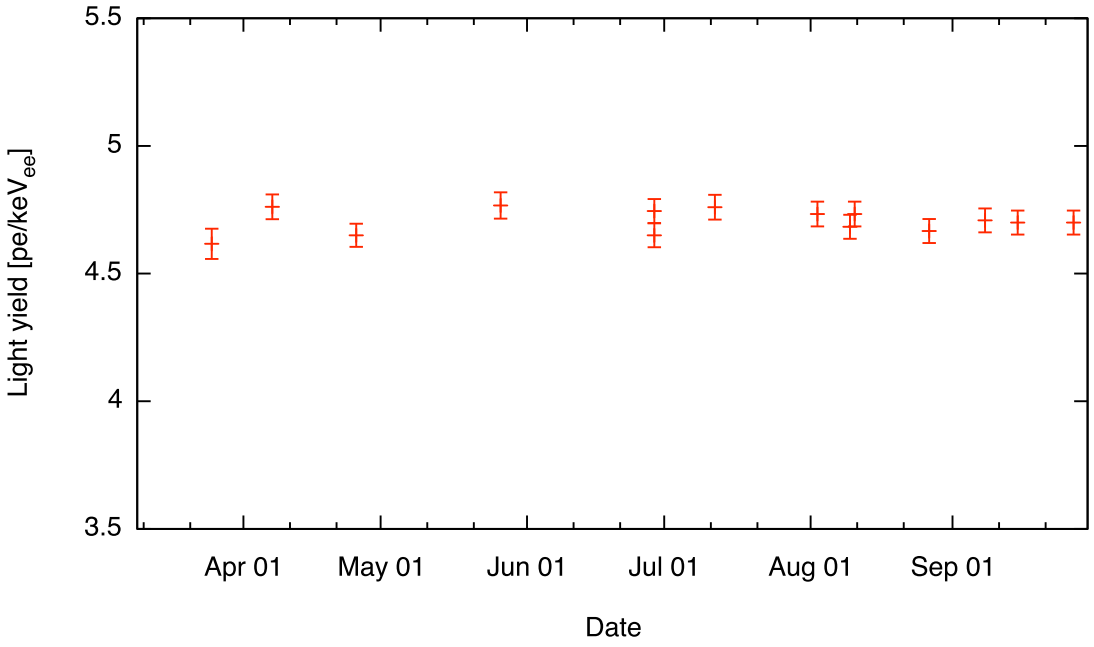

Figure A.1: Light yield as function of time in V3.

Fig. A.3 shows, this is not the case. The triplet lifetime was stable over time.

The other two possible reasons for a drop in light yield are degradation of the TPB and degradation of the optical properties of the acrylic. No such degradation of the TPB was observed in the previous versions of the detector. Acrylic light guides made from the same material is the ones used in this version of DEAP-1 were in fact observed to turn from clear to yellow-tinted over the course of a few months.

The light yield is a function of deposited energy. This is discussed in E. O'Dwyers thesis[60].

The location of an event along the axis of the detector, Zfit, can be determined by the fraction of light that the left and the right PMT observe. The light yield is somewhat dependent on the location of the event. This dependence is calibrated by moving a ^{22}Na source along the side of the detector and determining the number of

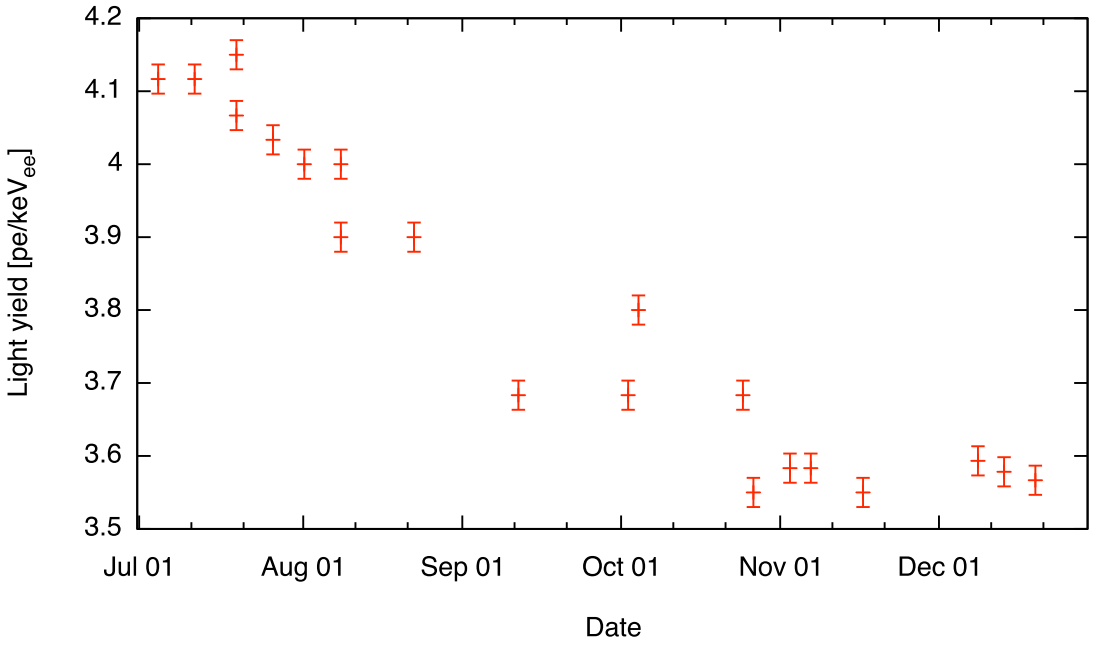

Figure A.2: Light yield as function of time in V5.

photo electrons corresponding to the 511 keV peak at each source location. The Zfit variable is calibrated at the same time. The calibration for V2 is:

$$PE = 1363 + (0.73 \cdot \text{Zfit} - 1.08)^2 \tag{A.1}$$

$$Z[cm] = 1.19 \cdot \text{Zfit} + 0.39 \tag{A.2}$$

The calibration for V3 is:

$$PE = 2263 + (1.01 \cdot \text{Zfit} - 0.33)^2 \tag{A.3}$$

$$Z[cm] = 1.13 \cdot \text{Zfit} + 2.56 \tag{A.4}$$

The calibration for V5 is:

$$PE = 2020 + (1.01 \cdot \text{Zfit} + 0.27)^2 \tag{A.5}$$

$$Z[cm] = 1.03 \cdot \text{Zfit} + 3.2 \tag{A.6}$$

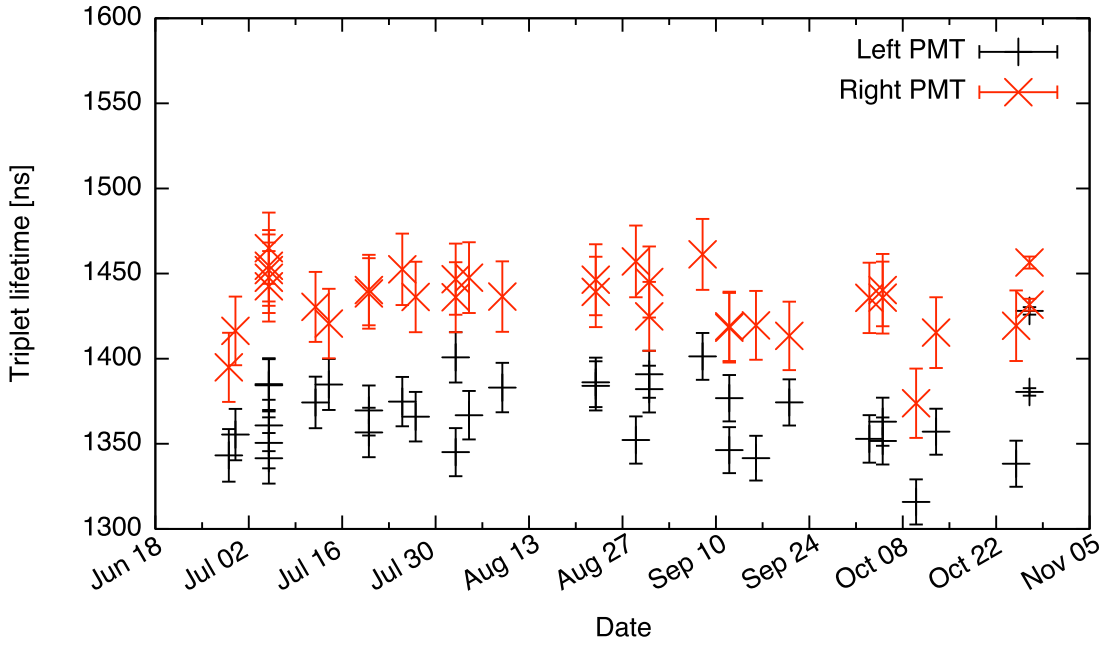

Figure A.3: Triplet lifetime in V5. Only statistical uncertainties are shown. There are systematic uncertainties related to the baseline correction and PMT behaviour, which cause the triplet lifetime measured with the left PMT to be different from that measured with the right PMT.

The range of any Zfit cut is translated into a liquid argon cut volume or surface area using these Zfit calibrations.

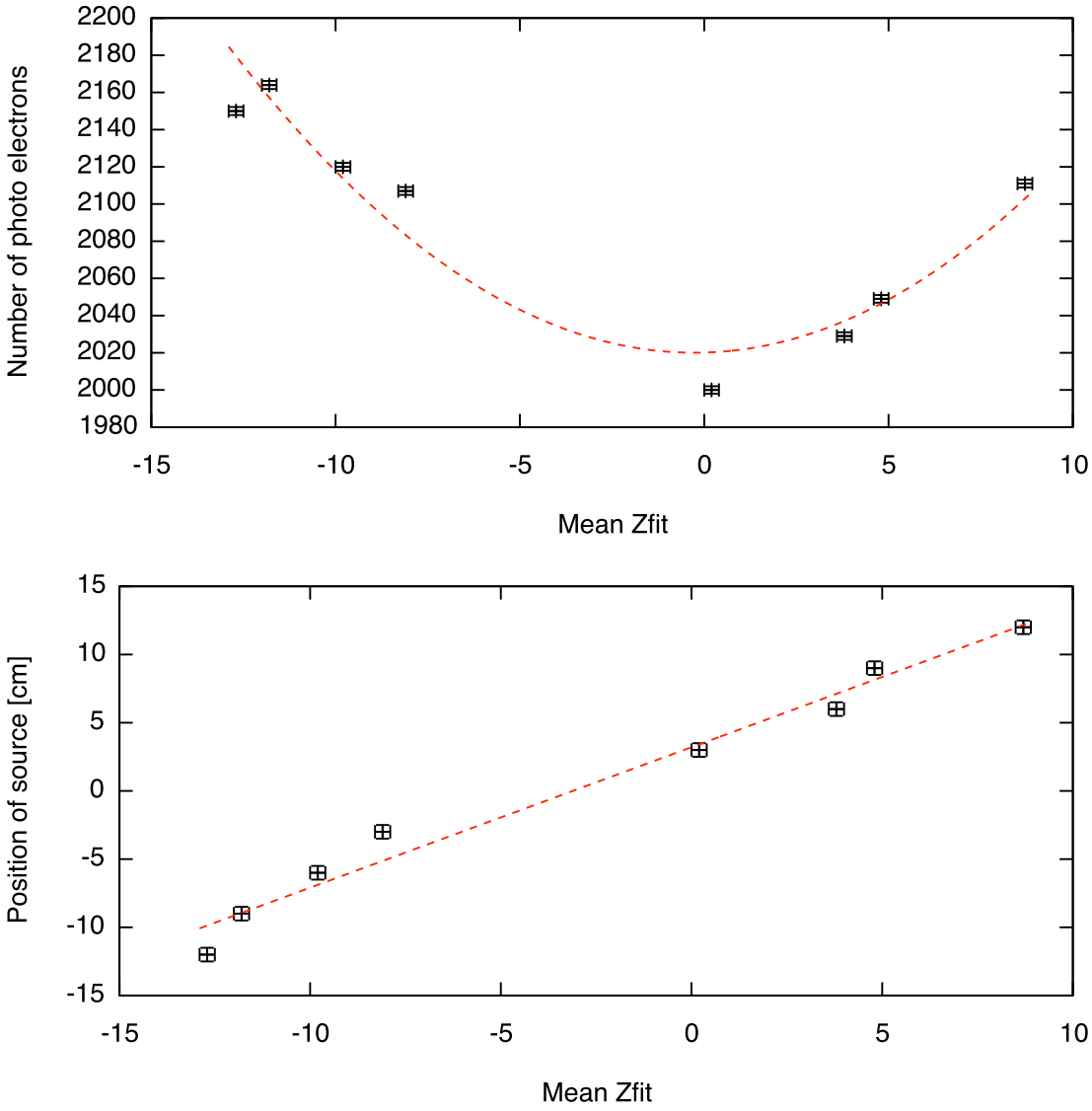

Figure A.4: Zfit calibration V5.

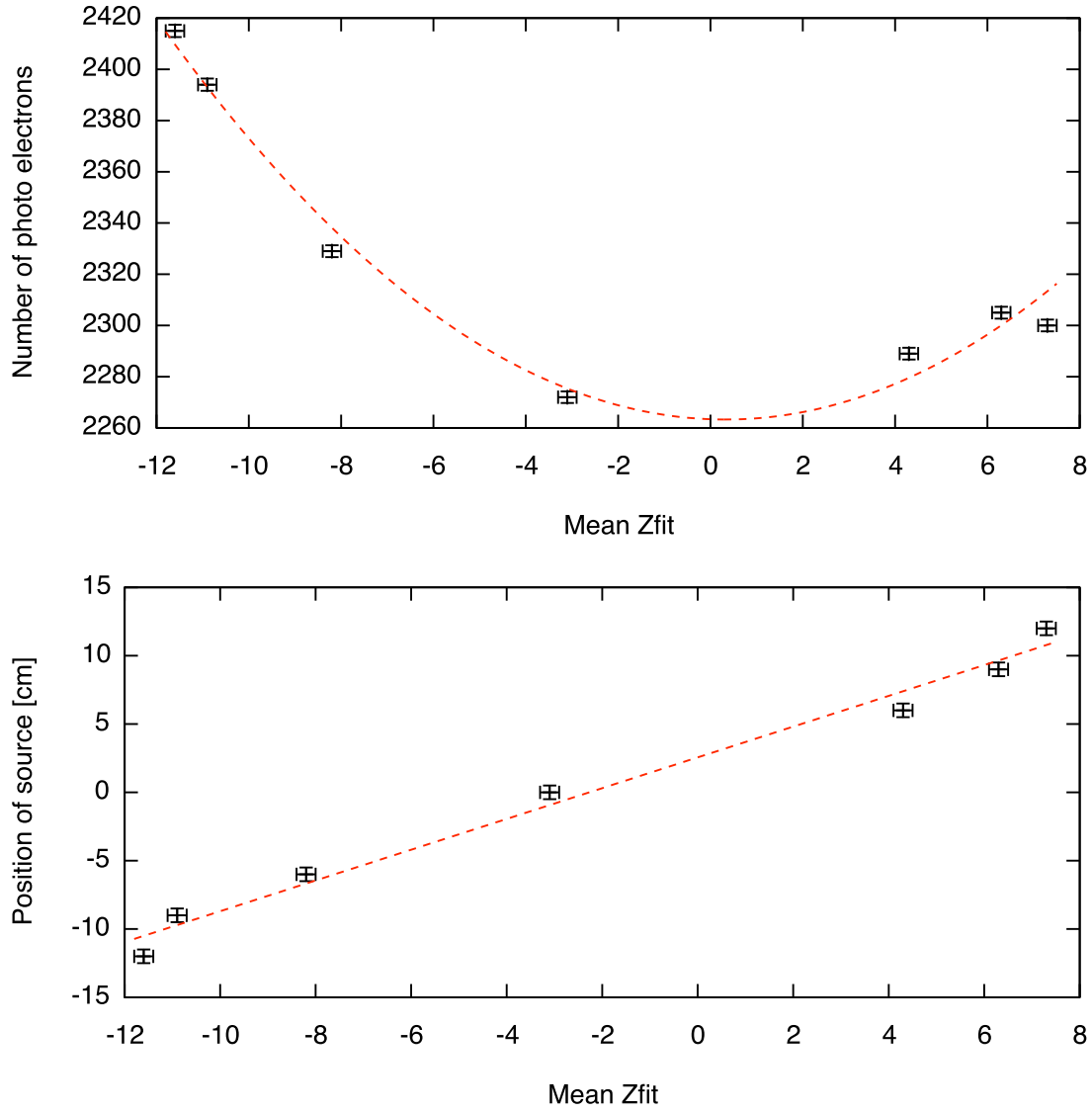

Figure A.5: Zfit calibration V3.

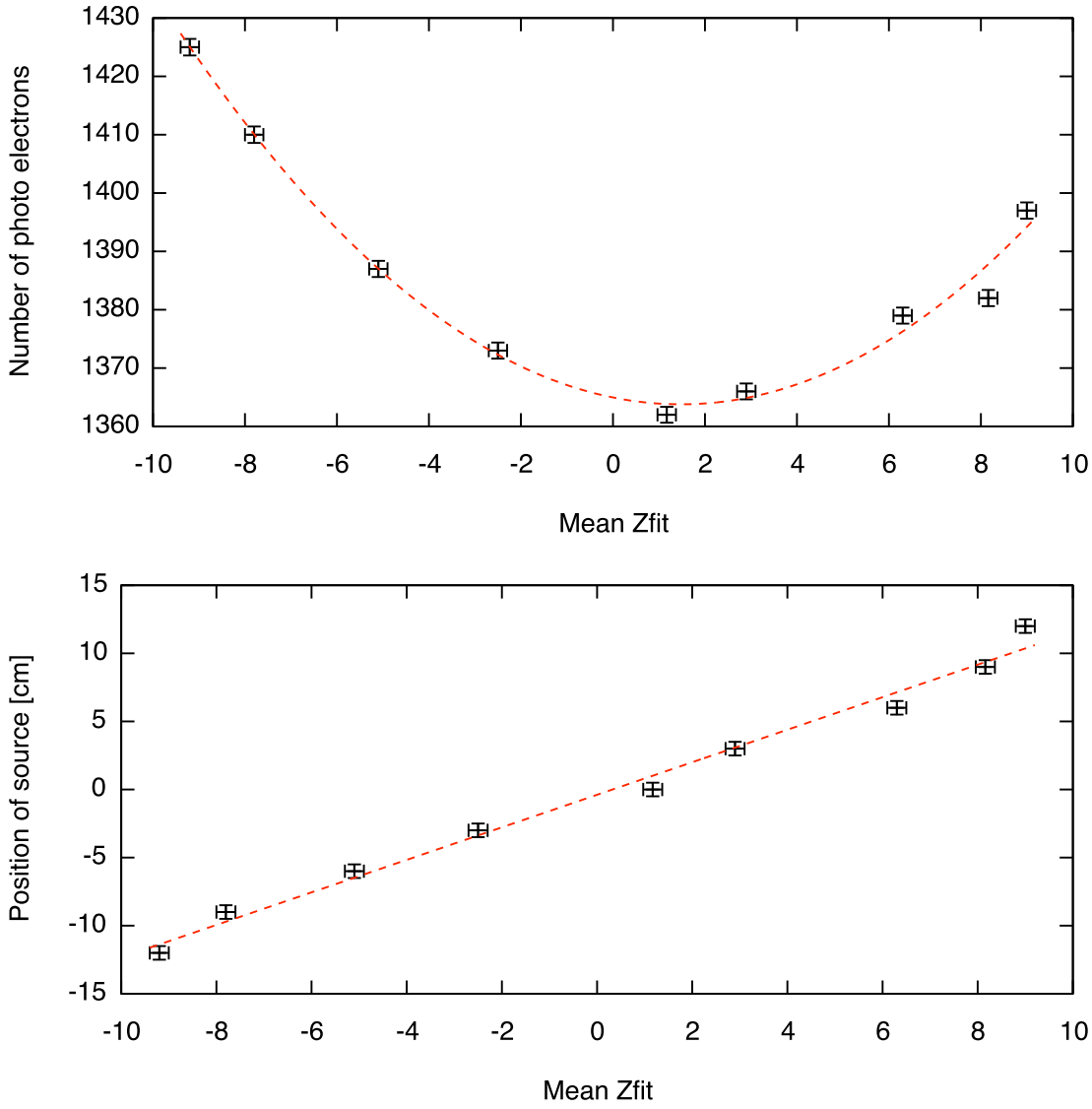

Figure A.6: Zfit calibration V2.

Appendix B

Data cleaning cuts for background runs

The following data cleaning cuts are applied for V2:

- HPromptPEn > 0 and HLatePEn > 0 (for n = 0 and 1). This cuts away noise events with no or negative charge.
- Abs(MinBin0 - MinBin1) < 25. This removes events where the peaks in the two PMTs are far apart in time
- PmtCutIDn == 7 (for n = 0 and 1). This removes events with double peaks and events where the baseline or peak finding algorithm failed.
- Fprompt > 45.0/TotalPE + 0.35 and Fprompt < 1.0 . This removes electron recoil events.

Runs used in the analysis are: 10035, 10055, 10057, 10080, 10081, 10083, 10087, 10089, 10098, 10137, 10175. For a total run time of 3,008,606 s.

The following data cleaning cuts are applied for V3:

- HPromptPEn > 0 and HLatePEn > 0 (for n $= 0$ and 1). This cuts away noise events with no or negative charge.
- Fprompt $< 10.0/\text{sqrt}(\text{TotalPE} + 500.0) + 0.12$ and Fprompt > 0.3 and Fprompt < 1 This removes electron recoil events.
- PmtCutIDn $== 7$ (for n $= 0$ and 1) This removes events with double peaks and events where the baseline or peak finding algorithm failed.
- Abs(Edge1 - Edge0) < 30. This removes events where the peaks in the two PMTs are far apart in time
- Edge1 > 640 and Edge1 < 680 and Edge0 > 640 and Edge0 < 680. This removes events with peaks far away from the trigger time.

Runs used in the analysis are: High voltage runs: 11056, 11057, 11068, 11077, 11078, 11086, 11091, 11099, 11135, 11139, 11141, 11145, 11146, 11162, 11163, 11167. For a total run time of 3,269,814 s. Low voltage runs: 11151, 11153, 11158, 11164, 11168. For a total run time of 1,210,024 s.

The following data cleaning cuts are applied for V5:

- HPromptPEn > 0 and HLatePEn > 0 (for n $= 0$ and 1). This cuts away noise events with no or negative charge.
- EventCutID $== 1$. This removes events with double peaks and events where the baseline or peak finding algorithm failed.

- Fprompt > 11.0/sqrt(TotalPE + 400.0) + 0.13 and (Fprompt > 0.4 if TotalPE > 3000) and Fprompt > 0.2 and Fprompt < 1. This removes electron recoil events.

- Abs(MinBin1 - MinBin0) < 20. This removes events where the peaks in the two PMTs are far apart in time

- MinBin0 > 650 and MinBin0 < 685. This removes events with peaks far away from the trigger time.

Runs used in the analysis are: High voltage runs: 13155, 13147, 13161, 13186, 13187, 13249, 13250, 13267, 13271, 13290, 13314. For a total run time of 2304639 s. Low voltage runs: 13148, 13167, 13188. For a total run time of 1160814 s.

Appendix C

Some notes on TPB evaporation

TPB comes in the form of a white crystalline powder, in either scintillating or non-scintillating quality. We typically use the non-scintillation quality TPB for initial testing of the evaporation setup, then use the scintillating-quality TPB for production evaporations. The nominal TPB evaporation point is at 207-209°C [66], but the deposition monitors typically starts to register material deposited on them at a crucible temperature of about 160°C.

The geometry of the evaporator used to make the TPB coatings for DEAP-1 is shown in Fig. C.1.

It consists of a cylindrical vacuum chamber with electrical feed throughs in the base for resistive heating and read out of the temperature sensor and deposition monitors. A pressure of better than 10^{-3} mbar is necessary for the TPB to travel more than a couple of centimetres.

The quartz crucible is heated by a nichrome wire wrapped around it in a spiral, and the temperature sensor is clamped to the nichrome wire. Because the sensor is not directly attached to the crucible, it might not reflect the actual crucible temperature

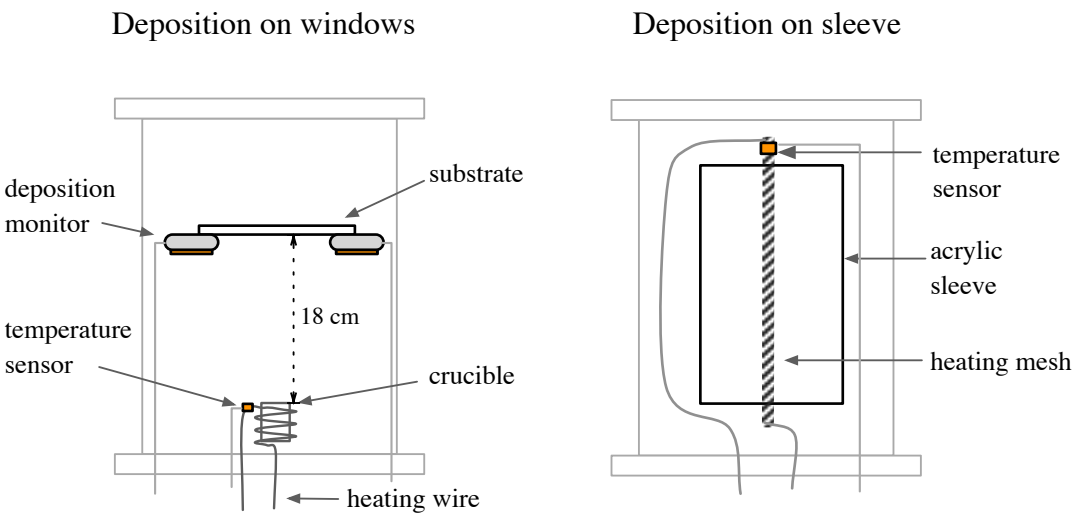

Figure C.1: Sketch of the evaporator setup for evaporating onto planar surfaces such as the DEAP-1 windows, and onto the cylindrical acrylic sleeve.

and could be up to about 5°C off.

Heating up the TPB in the crucible should not be done too quickly, as this will lead to the TPB touching the crucible evaporating away quickly, leaving a cylinder of partially melted TPB in the centre. The evaporation rate then drops to zero, because the heat transfer from the warm crucible wall through vacuum to the TPB block is not good enough for further evaporation. In the worst case, the evaporation has to be stopped so that the TPB cylinder can be physically broken up. Otherwise, the cylinder can fall over and evaporation takes place again, but not in a uniform manner. Small explosions where TPB crystals are ejected from the crucible are also possible when heating up too quickly.

Taking at least 40 minutes to an hour to reach 200°C reliably prevents any of the above mentioned problems.